A Micro-scale Method to Associate the Fatigue Properties of Asphalt Binder, Mastic and Mixture

Dong Wang

Dissertation submitted to the faculty of
Virginia Polytechnic Institute and State University
in partial fulfillment of the requirements for the degree of

Doctor of Philosophy
in
Civil and Environmental Engineering

Linbing Wang, Committee Chair
Romesh Batra
Joseph Dove
Elisa Sotelino

Feb 25th, 2011
Blacksburg, Virginia

Keywords: Asphalt mixture, Fatigue, X-ray Tomography, Finite Element Method

A Micro-scale Method to Associate the Fatigue Properties of Asphalt Binder, Mastic and Mixture

Dong Wang

(Abstract)

The fatigue damage is one of the most common distresses observed on the asphalt concrete pavement. The initiation and propagation of the fatigue damage is a complicated phenomenon and very difficult to detect. In order to thoroughly understand the fatigue of asphalt concrete, the behaviors of the key components of asphalt concrete under cyclic loading are investigated respectively. A new experiment method is developed to test the performances of asphalt binder, mastic and mixture under cyclic loading, which provides a tool to unify the fatigue test method for both binding medium and asphalt mixture. Using the new fatigue test method, the effects of loading magnitude, temperature and loading rate to the performance of the asphalt binder under cyclic loading are estimated. Mastic and mixture specimens are prepared by adding fillers and controlled-size aggregates into the asphalt binder. The effects of filler content to the performance of mastic specimen are discussed. The differences between the test results of mastic and mixture are compared and analyzed. Incorporated with the new fatigue test, x-ray tomography system is used in this study to: 1. Analyze the structure change of the mastic specimen before and after the fatigue test. 2. Compare the void content differences between the mastic and mixture specimens. 3. Reconstruct the 3-D internal structures of mastic and mixture specimens to build up the digital specimens. The digital specimens are used in the fatigue simulation of the asphalt binder, mastic and mixture specimens based on the finite element method. The asphalt binder, filler and aggregate are treated as different materials. Damage parameter is introduced to model the degradation of elastic modulus of the asphalt binder caused by fatigue damage. Direct cyclic analysis available in ABAQUS is used to obtain the response of the material after large number of loading cycles. The basalt fibers are dispersed into the asphalt binder and mastic specimens, the effects of the basalt fiber to the performances of the binder and mastic at low temperature are analyzed using both experimental and FEM modeling methods.

ACKNOWLEDGEMENTS

The author wants to thank his advisor, Dr. Linbing Wang for his patient supervision, encouragement and support. His valuable and constructive advice and comments are greatly appreciated.

The author also wants to thank his advisory committee members, Dr. Romesh Batra, Dr. Joseph Dove, and Dr. Elisa Sotelino, for their valuable advices and support.

The author would like to thank his colleagues and friends for their help both in and out of office and laboratory. The research was made possible with the support from the Department of Civil and Environmental Engineering and VTTI of Virginia Tech.

TABLE OF CONTENTS

LIST OF FIGURES

LIST OF TABLES

Chapter 1. Introduction

1.1 Background

Stone-based material is the most widely used construction material in the world. It is considered as a composite material consisting of mineral aggregates, binding medium and air voids. In the construction of pavement, major materials used are cement concrete and asphalt concrete. Cement concrete is composed of Portland cement, aggregates, water and chemical admixtures. The water reacts with the cement and produces the binding medium among aggregates. Aggregates are made of crushed rocks, gravels and fine aggregate like sand. Cement concrete is used in all kinds of infrastructures. About 7.5 cubic kilometers of cement concrete are made each year in the world. In the United States, Cement concrete requires a US $35-billion industry which employs more than two million workers. Asphalt concrete is another majorly used material for pavement construction. Different from cement concrete, asphalt is used as binder to mix with mineral aggregates in asphalt concrete. The heated asphalt concrete is laid down on the road and compacted in layers. It is reported that 96% of all paved roads and streets in the US, almost two million miles of road, are surfaced with asphalt concrete.

Asphalt concrete pavement is highly susceptible to cracking damages. Usually, micro-cracks initiate deep within the structure where detection is very difficult. Due to the repeated vehicle and environmental loading, these invisible micro-cracks propagate and connect to each other, leading to mechanical degradation of asphalt materials. The micro-cracks accumulate until

visible macro-cracks appear. Then maintenance and rehabilitation work become mandatory and extremely expensive.

Fatigue cracking is one of the main cracking damages observed on the asphalt concrete pavements of the US. It is defined as failure of pavement structure due to repeated stresses which are not large enough to cause immediate fracture. Generally, fatigue cracking is described as a process where micro-cracks accumulate and connect to each other until macro-cracks are formed and then propagate through the pavement. Sometimes, the cracks cut the pavement surface into many sharp-angled small pieces and develop a pattern resembling the skin of an alligator. So, the fatigue cracking is also called alligator cracking.

The fatigue of asphalt concrete is a complicated phenomenon because the initiation and propagation of fatigue cracking is very difficult to detect. In order to understand the mechanism of the fatigue damage, the National Cooperative Highway Research Program (NCHRP) started a project in 2005 to study the initiation of fatigue damage and tried to include this into M-E design method. The Asphalt Research Consortium in 2007 also proposed a fatigue damage study of the asphalt pavement. This study included a model based on principles of the mechanics and considers the impact of the mixture's internal structure on stress distribution. Most current research efforts are focused on the asphalt mixture. However, as a composite material, the performance of asphalt concrete is determined by its major components including aggregates, binding medium and air voids. A thorough understanding of their behaviors in the fatigue process is also essential. Aggregate is a main component forming the skeleton of the structure. Due to high stiffness, the damage of aggregate caused by fatigue is very limited. Compared with an aggregate, the stiffness and strength of the binding medium are much lower. So, the binding

medium among aggregates is more vulnerable and sensitive to cyclic loading. A research to investigate the fatigue of the major components of asphalt mixture is meaningful and necessary.

1.2 Research objectives

This work investigates the fatigue behavior of the major components of the asphalt mixture during the fatigue process. Traditionally, the fatigue behaviors of asphalt mixture and asphalt binder are evaluated separately. The experiment methods to estimate the fatigue of asphalt binder and mixture are not unified. This work is intended to design a new experiment method which is able to test both asphalt mixture and asphalt binder. Also, as a major component of the binding medium, the fatigue performance of the asphalt mastic will also be investigated. Another objective of this research is to find the cause of fatigue damage. The internal structures of mastic and mixture specimens are compared using x-ray tomography. The structure change of the mastic specimen before and after the fatigue test is also evaluated. The internal structures of each specimen are scanned and used to build up digital specimens for simulation. The designed fatigue test is simulated based on Finite Element Method (FEM). The simulation results will be compared and calibrated with lab test results to build up a digital test served as an alternative method for further research. To improve the performance of asphalt materials at low temperature, basalt fibers are mixed with asphalt binder and mastic specimens. The effects of this new modifier will be evaluated using both experimental and FEM modeling methods.

In short, the overall objectives of this research include:

1. Designing a lab test which can be used to estimate the fatigue performances of major components of asphalt mixture.

2. Utilizing the x-ray tomography system to analyze the property change of asphalt mastic and asphalt mixture caused by fatigue loading.

3. Obtaining the internal structure of the mastic and mixture specimens from x-ray scanning and build up digital specimens.

4. Conducting digital tests to simulate the fatigue tests of asphalt binder, mastic and mixture specimens by considering the internal structure of the materials.

5. Evaluate the effects of basalt fibers to the performances of the asphalt binder and mastic at low temperature by using both experimental and FEM modeling methods.

Chapter 2. Literature Review

2.1 Fatigue of the asphalt mixture

2.1.1 Theoretical model

To consider the fatigue of asphalt mixture into the pavement design, different theoretical models used to predict the fatigue life were developed. At the early period, the fatigue life of asphalt mixture was analyzed based on a power-law relationship between stress or strain level and number of load applications to failure. Typical format of the model is shown in the Equation 2-1.

$$N_f = a(\frac{1}{\varepsilon_0})^b \text{ or } N_f = c(\frac{1}{\sigma_0})^d \quad (2\text{-}1)$$

in which, N_f is the number of load applications to failure. ε_0 and σ_0 are the applied strain and stress level. a,b,c,d are the parameters determined by material characteristics and experiment conditions. (Ghuzlan and Carpenter 2002). This method was widely used because of its simplicity at the early research stage, but this method did not consider the internal fracture or damage accumulations caused by the fatigue and it was experimental dependent.

Model based on dissipated energy concept is another method to characterize the fatigue of asphalt mixture. Dissipated energy is the energy loss in a loading and unloading process. When a stress is applied on a material, a strain would be induced and recovered in a loading and unloading process, the energy put into the material is recovered if the loading and unloading curves coincide. If they do not coincide, there is energy lost in this process. The energy loss in

this loading and unloading cycle could be used as an indicator of induced damage. Based on this concept, researchers developed models to predict the relationship between fatigue life of asphalt mixture and dissipated energy in cyclic loading process. (Aglan and Figueroa 1993; Bonnetti *et al*. 2002; Si *et al.* 2002; Daniel and Bisirri, 2005; Carpenter and Shen, 2006; Ghuzlan and Carpenter, 2006).

Facture mechanics including linear elastic fracture mechanics and non-linear fracture mechanics is another widely accepted method to model the fatigue of the asphalt concrete. In the linear elastic fracture mechanics, stress intensity factor K which characterizes the stress distribution in the vicinity of a macro-crack is developed. The crack growth during the fatigue process can be expressed as a function of K based on the Paris' Law. Typical crack growth curved described by Paris' law is shown in Figure 2-1. There are three phases in the entire range of crack growth. The second phase is a linear region and can be expressed as Paris equation shown in Equation 2-2.

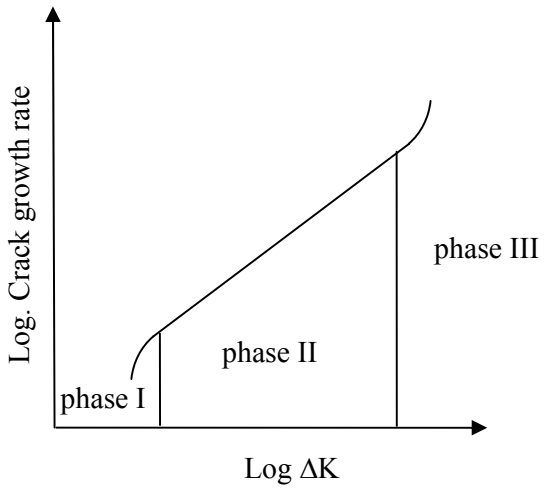

Figure 2-1 Fatigue crack growth described by Paris' law

$$\frac{da}{dN} = A \cdot \Delta K^n \tag{2-2}$$

Where da/dN is the crack length growth rate over number of loading applications, A and n are parameters depending on material properties, loading frequency and mode, temperature and environmental conditions and can be determined by experiment. Some fatigue models were developed based on linear-elastic fracture mechanics. (Majidzadeh *et al*. 1972; Sulaiman and Stock, 1995; Ramsamooj 2002;). In the non-linear fracture mechanics, plastic deformation of the material is considered. Non-linear behavior of the material is characterized by the J-integral which can be used as both an energy parameter and a stress intensity parameter. J-integral is defined in Equation 2-3:

$$J = \int_{\Gamma} (Wdy - \sigma_{ij} n_j \frac{\partial u_i}{\partial x} ds) \tag{2-3}$$

Where W is the strain energy density, Γ is any contour around the crack tip and ds is a length increment along the contour, x and y are the coordinate directions, σ_{ij} is the Cauchy stress tensor and n_j is the normal to the contour Γ. In non-linear fracture mechanics, the crack growth rate is expressed as a function of J-integral instead of K. This method is also used to characterize fatigue properties of asphalt mixtures. (Abdulshafi and Majidzadeh, 1985; Button *et al*., 1987; Sulaiman and Stock, 1995; Mull *et al*.,2002)

Fatigue models based on damage mechanics are also widely used to predict the fatigue life of asphalt mixture. The continuum damage model ignores the micro cracks and focus on the

stiffness of the materials. Damage parameter D based on this concept is developed shown in Equation 2-4:

$$D = \frac{S_D}{S} \tag{2-4}$$

Where S is the initial load bearing cross-section area and S_D is the effective area of intersections of all micro cracks located within S. Generally, the damage evolution over cyclic loadings is expressed as a function of current state shown in Equation 2-5:

$$\frac{\partial D}{\partial N} = \frac{\partial D}{\partial N}(\varepsilon_0, D) \tag{2-5}$$

Where N is the number of loading cycle, ε_0 is the applied strain amplitude and D is the damage parameter. The degradation of stiffness caused by fatigue is modeled based on damage mechanics. (Lee *et al.* 2000; Bodin *et al.* 2004; El-Basyouny 2005; Castro and Sanchez 2007; Suo and Wong 2009; Wen and Bahia 2009).

Other theoretical models developed to describe the fatigue of the asphalt mixture include the damage model based on mixture bonding energy (Rodrigues 1999), artificial neutral network approach (Huang *et al.* 2006) and fuzzy-logical approach (Tigdemir 2001).

2.1.2 Fatigue experiment

There are several different lab test methods to investigate the fatigue properties of asphalt concrete. Shatnowi *et al.* (1997) used repititive direct tension test to evaluate the fatigue performance of the asphalt concrete. Nowadays, the repeated flexural bending test is

recommended by American Association of State Highway and Transportation Officials (AASHTO) as the major lab test method to evaluate the fatigue properties of the asphalt mixture. The fatigue life of a 380 mm long by 50 mm thick by 63 mm wide Hot Mix Asphalt (HMA) beam specimen sawed from laboratory or field compacted HMA is determined by the test. Repeated flexural bending is applied on the specimen until it is failed.

Generally, a repeated flexural bending test system consists of a loading device, an environmental chamber and a data acquisition system. The loading device receives commands from the control system and applies a load so that the specimen experiences a constant strain during each loading cycle. A typical flexural bending beam apparatus is shown in the Figure 2-2. Cyclic sinusoidal load at a frequency of 5 to 10 Hz is applied and the specimen is subjecting to a 4 point bending with free rotation and horizontal translation at all load and reaction points. The specimen is forced back to the original position at the end of each loading cycle.

The test temperature is maintained to be 20.0 °C by the environmental chamber during testing. The beam deflection, number of loading cycles and applied load are recorded during each loading cycle. The data recorded are used to compute maximum tensile stress, maximum tensile strain, phase angle, stiffness, dissipated energy, and cumulative dissipated energy. As the major experimental method to evaluate the fatigue properties of asphalt mixture, flexural bending beam test is widely used in the research of the asphalt concrete fatigue. (Epps 1969; Monismith *et al.* 1971; Sousa *et al.* 1993; Tayebali 1994; Harvey and TSai 1996; Sousa *et al.* 2007)

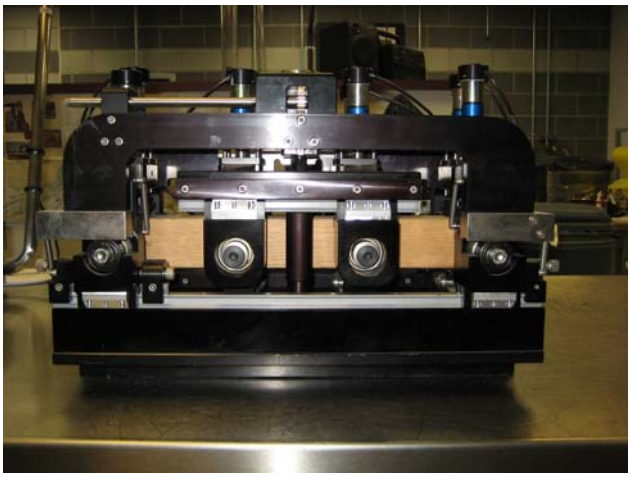

Figure 2-2 Flexural bending beam apparatus

2.2 Fatigue of asphalt binder

Asphalt binder is a major component of the binding medium among aggregates. The fatigue properties of asphalt binder have critical impacts on the performance of the asphalt mixture. It is challenging to apply repeated loading to this sticky viscoelastic material. This difficulty is the main reason that kept researchers from focusing on binder fatigue. (Martono *et al.* 2007). Strategic Highway Research Program accepted to use Dynamic Shear Rheometer (DSR) as the experimental tool to evaluate the fatigue properties of asphalt binder. This method is mainly used by researchers to investigate the fatigue properties of the asphalt binder. (Anderson *et al*. 2001; Shen *et al.* 2010). The DSR is a rotational rheometer that applies oscillatory shear to asphalt binder (Figure 2-3). The rheological properties of asphalt binder are estimated through the response of the material to the applied stress or strain. Asphalt binder is considered as a visco-elastic material at high and intermediate service temperature. The DSR measures complex modulus /G*/ and phase angle δ . The term /G^*/sin δ at a fixed frequency and temperature is used as the specification parameter to give a measure of the fatigue resistance of asphalt binders.

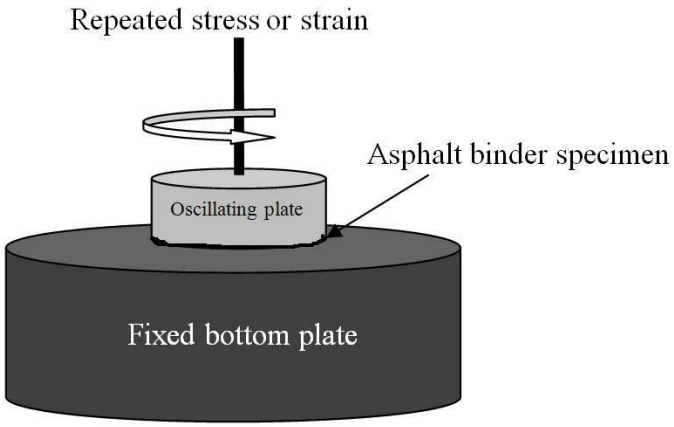

Figure 2-3 Dynamic shear rheometer

However, some recent research has shown that there exist limitations with using the DSR as test method to study the fatigue properties of asphalt binder. Decan *et al.* (1997) analyzed the results data from Strategic Highway Research Program (SHRP) test program to examine the effects of binder loss stiffness on the fatigue performance of asphalt mixture. They concluded that current specification parameter $/G^*/\sin\delta$ is counterproductive for sections of asphalt concrete more than 50 mm in thickness and suggested that an alternative experiment method should be used to estimate the fatigue resistance of the asphalt binder. Anderson *et al*. (2001) examined the DSR method with respect to a phenomenon called edge fracture. Two different modes of failure were observed when asphalt binders were tested with time sweeps: one in which internal micro-cracks appear to occur and another in which the loss of modulus because of flow at the edges of the sample known as edge fracture. It is reported that when instability flow dominates the behavior of the asphalt binder, fatigue life as measured in DSR depends highly on gap spacing and DSR, with its current limitations, is not a suitable method for characterizing the fatigue behavior of asphalt binders. Shenoy (2002) reevaluated the current specification parameter to rank the

fatigue resistance of the asphalt binder $/G^*/\sin\delta$ and found that the parameter was ineffective in estimating the fatigue resistance of asphalt binder, especially when polymer-modified binder were tested. A better binder based fatigue test should be developed.

2.3 Fatigue of asphalt mastics

Asphalt mastic, defined as the mix of binder and fine aggregates, is also a major component of binding medium. To thoroughly understand the fatigue phenomenon of the mixture, a study of the fatigue of asphalt mastic is necessary. However, only a few researches about the fatigue of asphalt mastic can be found. Smith and Hesp (2000) conducted DSR tests on mastic specimen to study the effects of fillers on the fatigue performance of asphalt binders. It is found that the asphalt binder shows brittle characteristic at low temperatures and causes the material to fracture relatively easily under applied mechanical stresses. The addition of the filler causes the energy-absorbing mechanisms to operate in greater volume of material rather than just within the vicinity of the crack tip. Energy required for fracture to occur also increases. Fatigue life of mastic is also influenced by the size of the particle, as the size of the filler decreases, the fatigue life of the asphalt mastic increases. Kim *et al* (2003) conducted DSR test to estimate the fatigue damage characteristics of binders and mastics by measuring fundamental mechanical material properties. It is concluded that fillers provide better resistance to micro-cracks because of a lower rate of damage evolution and higher capability for total damage accumulation.

It can be found that traditional research efforts were mainly focus on the asphalt mixture, the fatigue of the asphalt binder and mastic were not well investigated. The current fatigue test method for asphalt binder and mastic, DSR test, used as the major experimental tool to define the

fatigue property of the asphalt binder is still questionable. The results of DSR test cannot be well correlated with the fatigue properties of asphalt mixture because the experimental methods are not unified.

2.4 X-ray tomography imaging

X-ray Tomography technique has been utilized as a nondestructive tool to evaluate the micro-structure and detect the internal false of the engineering materials for a long time. Generally, an x-ray tomography system contains a light source from which an x beam is produced and a detector system used to receive the transmitted x-ray shown in Figure 2-4. The transmitted ray beams have a varying intensity dependent on the internal structure of the scanned object. The varying intensity is referred to as a profile and then manipulated to produce a reconstructed image of an object.

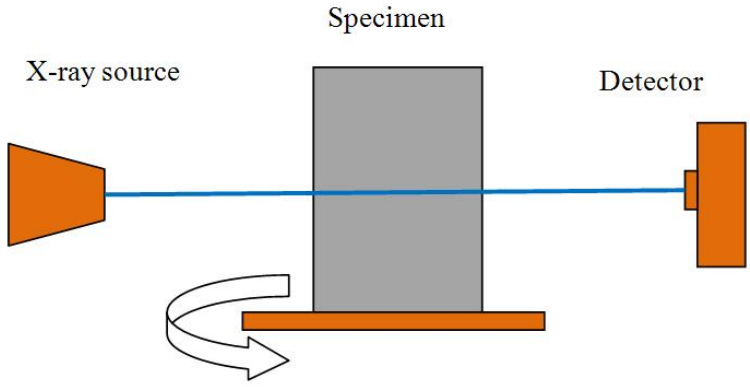

Figure 2-4 X-ray tomography system

The internal images of a material are obtained by analyzing the attenuation of X-rays when passing through the material. The attenuation coefficient along the X-ray path is given by the equation 2-9:

$$I = I_0 e^{-\int_0^l \mu(x,y,z)dl} \tag{2-9}$$

where I_0 is the incident X ray intensity and I is the X ray intensity after traveling through the scanned specimen. The equation above is solved by the software using reconstruction techniques. 2-D images are generated by estimating the distribution of the coefficients of attenuation along the travel path. The obtained 2-D slices can be used to generate 3-D structure based on the theory of Stereology. (Bay *et al*.1999)The basic principle of Stereology is that the information in a 2D image can be extended to give information about the 3D information of the sample; the general relation is given by Equation 2-10:

$$P_p = V_v \tag{2-10}$$

where V_v is the volume fraction occupied by an object and P_p is the area fraction in 2D. Recently, this technique has been utilized in the microstructure characterization of the asphalt concrete. (Wang *et al*. 2001, 2003, 2004; Chehab *et al*.2007;You *et al.* 2008;).

2.5 Simulation of fatigue using finite element method

ABAQUS developed by DS SIMULIA Corp is a software application widely used for engineering modeling based on Finite Element Method (FEM). It is used in this study to simulate

the fatigue behavior of asphalt materials. A constitutive model for material subjected to cyclic loading is applied to describe the mechanical behavior of the asphalt binder at low temperature. The details of the constitutive model are described below.

2.5.1 Elasto-plastic model

The constitutive model used to describe the behavior of the asphalt binder under cyclic loading is an elasto-plastic model proposed by Lemaitre and Chaboche in 1990. In this model, the total strain rate $\dot{\varepsilon}$ is written in terms of the elastic and plastic strain rates as:

$$\dot{\varepsilon} = \dot{\varepsilon}^{el} + \dot{\varepsilon}^{pl} \tag{2-11}$$

The elastic behavior is modeled as linear elastic:

$$\sigma = E \cdot \varepsilon \tag{2-12}$$

where E represents the Elastic modulus and σ and ε are the stress and strain tensors.

The yield surface is defined by the function

$$f(\sigma - \alpha) = \sigma^0 \tag{2-13}$$

where $f(\sigma - \alpha)$ is the equivalent Mises potential with respect to the backstress α, and σ^0 is the size of the yield surface.

The associated plastic flow is assumed:

$$\dot{\varepsilon}^{pl} = \frac{\partial f(\sigma - \alpha)}{\partial \sigma} \dot{\bar{\varepsilon}}^{pl} \tag{2-14}$$

where $\dot{\varepsilon}^{pl}$ represents the rate of plastic flow and $\dot{\bar{\varepsilon}}^{pl}$ is the equivalent plastic strain rate

$$\dot{\bar{\varepsilon}}^{pl} = \sqrt{\frac{2}{3} \dot{\varepsilon}^{pl} : \dot{\varepsilon}^{pl}} \tag{2-15}$$

The size of the yield surface, σ^0, can be easily defined as a exponential law function of equivalent plastic strain:

$$\sigma^0 = \sigma\big|_0 + Q_\infty (1 - e^{-b\bar{\varepsilon}^{pl}}) \tag{2-16}$$

where $\sigma\big|_0$ is the yield surface size at zero plastic strain and Q_∞ is the maximum change in the size of the yield surface and b defines the rate at which the size of the yield surface changes as plastic strain develops:

The evolution of the backstress α of the model is defined as

$$\dot{\alpha}_k = C_k \frac{1}{\sigma^0} (\sigma - \alpha) \dot{\bar{\varepsilon}}^{pl} - \gamma_k \alpha \dot{\bar{\varepsilon}}^{pl} \tag{2-17}$$

the overall backstress is computed from the relation

$$\alpha = \sum_{k=1}^{N} \alpha_k \tag{2-18}$$

Where N is the number of backstress, and C_k is the initial kinematic hardening modulus and γ_k determines the rate at which the kinematic hardening modulus decrease with increasing plastic deformation. The determination of parameters for the model will be described in details in chapter 6.

2.5.2 Progressive damage in fatigue analysis

The initiation and propagation of the fatigue cracks are modeled by different methodology including cohesive zone model (Yang *et al*. 1999, Kim, *et al.* 2006, 2007, 2008), energy-based damage model (Darveaux 2000; Lau *et al*. 2002; Zhang *et al.* 2003) and modified crack layer model (Aglan and Bayomy 1997). Some experimental methods are also developed to monitor the initiation and propagation of the fatigue cracks in asphalt concrete. (Scehffy 1999)

An energy-based damage model proposed by Darveaux to link the fatigue life of the solder joints with crack initiation and propagation is utilized to describe the progressive damage. In Darveaux's model, the number of cycles before crack initiation is calculated as:

$$N_0 = c_1 \Delta w^{c_2} \tag{2-18}$$

where Δw is accumulated inelastic hysteresis energy per cycle, c_1 and c_2 are material constants determined by test data. The crack growth rate per cycle is calculated by a similar form of equation:

$$\frac{da}{dN} = c_3 \Delta w^{c_4} \tag{2-19}$$

where a is the crack lengh, c_3 and c_4 are two constants determined by the test data. In ABAQUS, instead of calculating the crack growth a , the propagation of a scalar damage variable D is calculated.

The rate of the damage in a material point per cycle is given by Equation 2-20

$$\frac{dD}{dN} = \frac{c_3 \Delta w^{c_4}}{L} \tag{2-20}$$

where c_3 and c_4 are material constants, and L is the characteristic length associated with an integration point. At any given loading cycle during the analysis the stress in the material is given by Equation 2-20

$$\sigma = (1 - D)\bar{\sigma} \tag{2-20}$$

where $\bar{\sigma}$ is the effective stress tensor that there is no damage in the material. The load carrying capacity of the material is lost when $D = 1$.

After damage initiation, the elastic stiffness of the material degraded progressively according to the damage evolution. A typical stress-strain relationship of a damaged elasto-plastic material under uniaxial tension test is shown in the Figure 2-6 below. The material response is linear elastic at period, a-b, followed by plastic hardening period, b-c. After the point c, instead of strain hardening to the point d', the material experiences a loading carrying capacity reduction period until rupture, c-d. Point c is the initiation point of the damage.

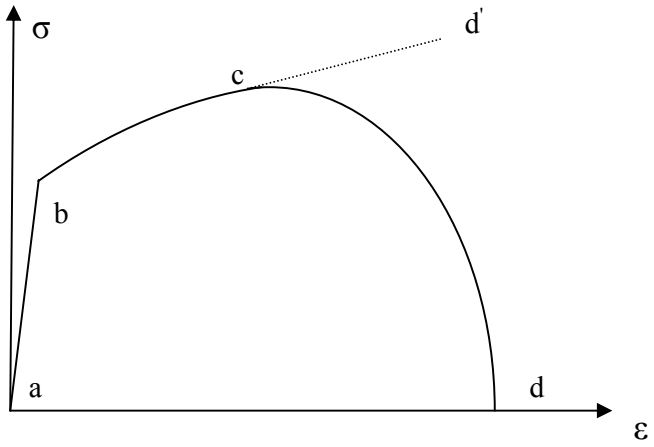

Figure 2-5 Typical stress-strain of an elasto-plastic material

Because the computational cost to simulate the progressive damage in a material over many load cycles is very expensive, only a small fraction of the loading history is simulated in the fatigue analysis. The response of the material during the small fraction of the loading history is then extrapolated over many load cycles to predict the likelihood of crack initiation and propagation.

In ABAQUS, the direct cyclic analysis capability provides a computationally effective modeling technique to obtain the stabilized response of a material subjected to cyclic loading. The response of the material is obtained by evaluating the elastic stiffness of the material at discrete points along the loading history as shown in Figure 2-7. The solution at each of the discrete points is used to predict the degradation of material stiffness that will take place during the next increment, which spans a number of load cycles, ΔN. The degraded material properties are then used to compute the solution at the next increment in the load history. This process is repeated up to the point where the fatigue life assessment is made.

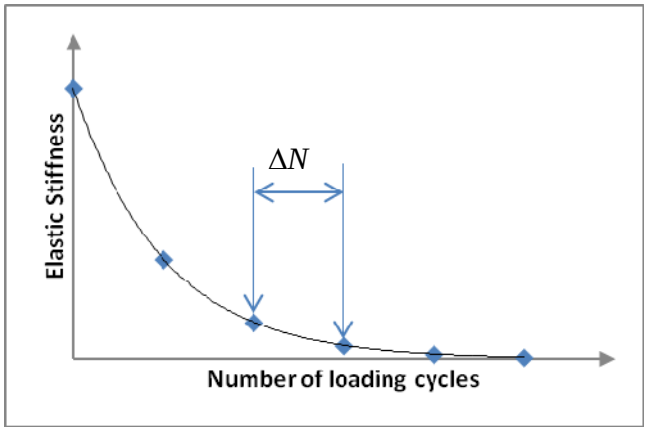

Figure 2-6 Elastic stiffness degradation as a function of the cycle number

Chapter 3. Methodology

In this work, a new fatigue experiment is designed to evaluate the performance of the asphalt binder and mastic under cyclic loading. Asphalt mixture containing controlled size aggregates will also be tested using the new methodology. The fatigue test results of asphalt binder, mastic and mixture will be compared. The internal structure of the mastic and mixture specimens will be obtained using X-ray tomography technique and applied to the mesh generation of the digital simulation. The experiment design procedure, X-ray tomography technique and fatigue test modeling utilized in this study will be described respectively in this chapter.

3.1 Experiment design

3.1.1 Direct tension tester

The Direct Tension Tester (DTT) of Interlaken Company, as shown in the Figure 3-1, is the major tool used in this study to evaluate the fatigue performance of asphalt binder, mastic and mixture. The DTT was originally designed to evaluate the stiffness and failure properties of asphalt binders at low temperatures. It contains a loading frame and measuring head driven by a gear motor. The applied loading and position information of the measuring head is provided by the sensor components of the system. The test temperature is controlled by a chiller system attached with DTT system. The loading frame and chiller system are shown in the Figure 3-2 and Figure 3-3 respectively.

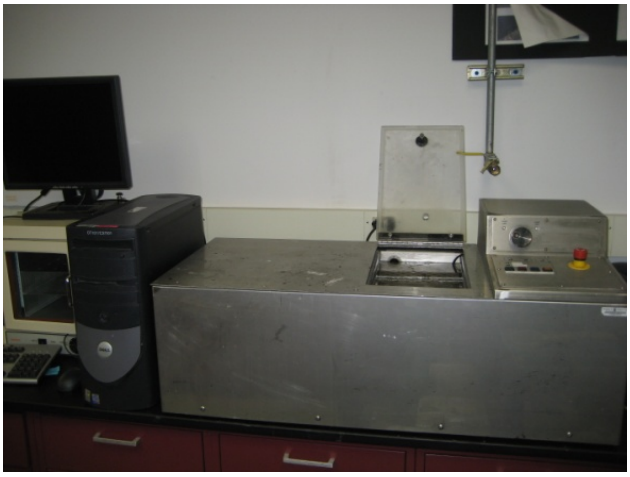

Figure 3-1 Direct tension tester

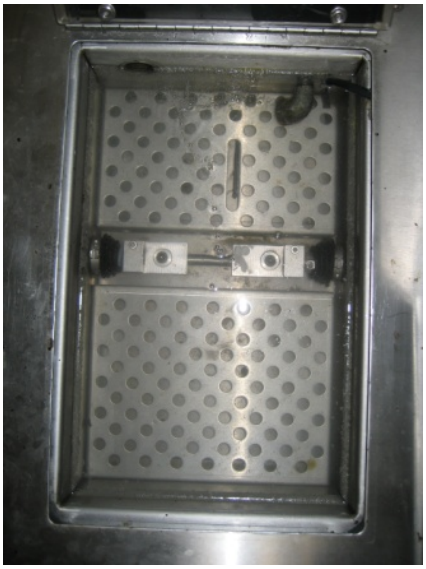

Figure 3-2 Loading frame of the direct tension tester

Figure 3-3 Chiller system of direct tension tester

3.1.2 Tester builder

The Test Builder is a software package developed by the Interlaken Company to build up customized test procedure. It configures the DTT machine to step through the user defined test procedure and make up a test. With this flexibility, a new fatigue test will be designed in which cyclic loading can be applied and the temperature and loading frequency of the test can also be controlled. The fatigue behavior of the asphalt binder, mastic and mixture can be evaluated using the designed fatigue test.

The main screen of the test builder is shown in the Figure 3-4. A complete test procedure is made of series of test steps. When a new step is generated, all of the boxes following the current step number will show as “undefined”. The action of the current step is defined by double clicking each box following the step number. A corresponding window will be opened and show the available options to configure the desired action. The first column of the Test Builder defines the step numbers. The second column defines the action that the control channel will perform. The

third column controls the chiller system. The fourth column controls the data acquisition. The fifth column controls the action for digital inputs and outputs. The last column is the event action that ends the current step and proceeds to the next step.

All the actions available for the control channel to perform are clearly described in the Test Builder Manual. In this study, a fatigue test procedure is designed which is able to apply cyclic loading to the specimen. Several specific actions used in this procedure are described in the APPENDIX A.

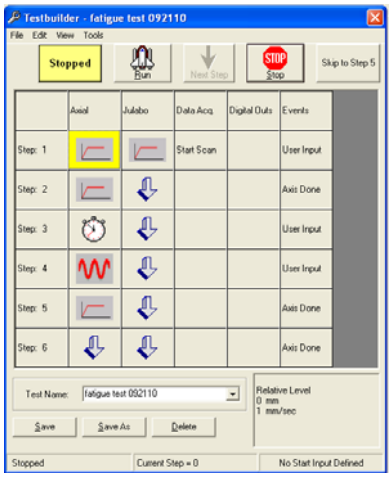

Figure 3-4 Main screen of the test builder

There are five steps in the new designed fatigue test procedure. Each step is described below:

Step 1: A 0.01N loading is applied on the loading end of the specimen at a rate of 0.01N/s. This step initiates the whole test procedure by applying a very small loading on the specimen so that the test can be started smoothly. The event used to control the switch from this step to the next step is "User Input". A window will open when the desired load is applied and let the user to zero the measured load at this time. The user needs to clear the current load state as zero and click the

"PROCEED" button to the next step. The load and displacement at the loading end of the specimen is measured and recorded from this step.

Step 2: A 2 N loading is applied on the loading end of the specimen at a rate of 0.1N/s which is the left end of the specimen shown in the Figure 3-5. This makes a good contact between loading pin and the specimen. The loading rate is small so that the gear motor loading system can be stable and not cause any errors on the machine. When the 2N load is applied, the user is asked to zero the measured displacement from this point the click the "PROCEED" button to the next step.

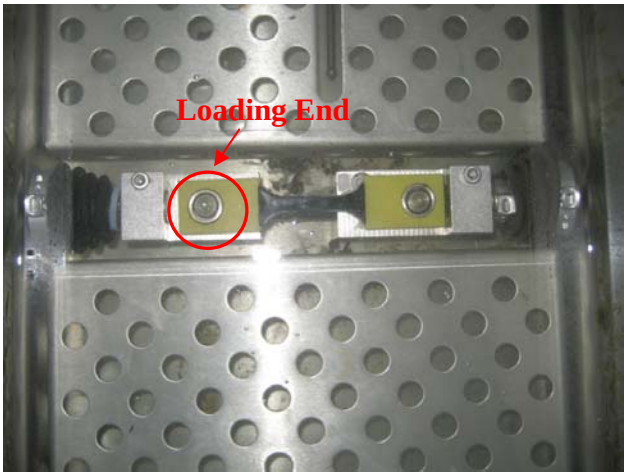

Figure 3-5 Loading end of loading frame

Step 3: A sinusoidal cyclic loading is applied at this step. The LEVEL1, which is the lower loading level of the sinusoidal loading, is still 2N which is same with the previous step. The LEVEL2, which is the higher loading level of the sinusoidal loading, is a specific value determined by the user. The load applied on the specimen is from LEVEL1 to LEVEL2 following a sinusoidal wave. The loading rate is set to be 0.5Hz. When the specimen fails, user is asked to click the "PROCEED" button to the next step.

Step 4: After the specimen fails, a ramp loading of 0.01N is applied on the specimen. Same as the step 1, this is used to finish the test smoothly. The test continues to the next step automatically when the load level is reached.

Step 5: A window prompts out to let the user save the results data. The results are saved in both .dat format and .mdl format. The results data includes the number of loading cycles, time, load value and displacement of the specimen.

3.1.3 Sample preparation

Binder specimen preparation

The asphalt binder used in the fatigue test is PG70-22 binder based on Superpave specification. The binder is obtained from the Asphalt Plant of the Roanoke city. The binder is contained in the small buckets and heated in the oven at 320 ^{o}F for 45 minutes shown in the Figure 3-6. The asphalt binder becomes fluid and can be poured into the specimen modes.

The specimen mode is composed of a bottom plate, two pieces of aluminum fixture with release agent painted on the surface contacting with asphalt and two plastic ends. Two fixtures are lying on the bottom plate with two plastic endings clipped at both ends forming a bone-shaped area shown as the Figure 3-7. Two clamps are used on both endings of the fixture to fix the whole mode. A piece of glassy paper is put between the specimen and bottom plate. The heated asphalt binder is poured into the mode as shown in the Figure 3-8 and the top surface of the specimen is flatted using a heated knife shown in the Figure 3-9.

Figure 3-6 Heated asphalt binder

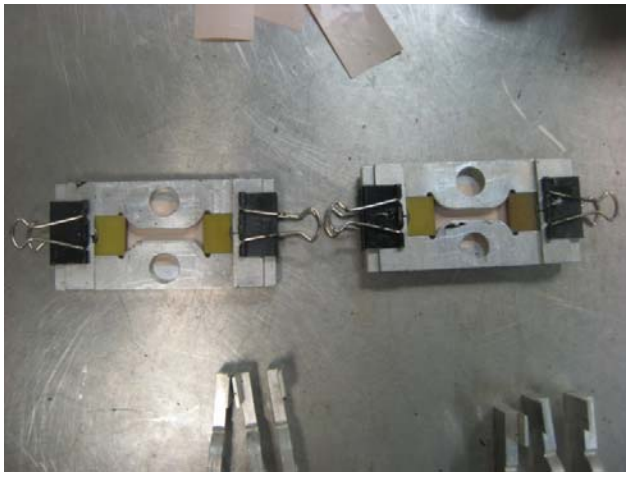

Figure 3-7 Specimen modes

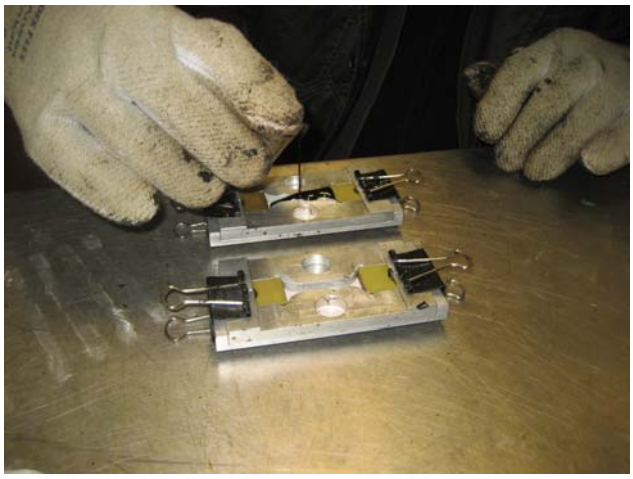

Figure 3-8 Making asphalt binder specimen

Figure 3-9 Surfacing asphalt binder specimen

Mastic specimen preparation

The procedure to make an asphalt mastic specimen is similar with the procedure to make an asphalt binder specimen. The quartz fillers shown in the Figure 3-10 are heated with asphalt binder at the same time. After 45 minutes of heating, the fillers are mixed with asphalt binder to

make mastic specimens. The amount of the fillers added into the binder is controlled by the weight ratio between the filler and asphalt binder.

Figure 3-10 Fillers used for mastic specimen

Mixture specimen preparation

Since the size of the specimens is determined by the specimen mode, the size of the aggregates added into the asphalt binder or asphalt mastic to make the mixture specimen is limited. Aggregates passing through #4 sieves but retained on #35 sieves are used to make asphalt mixture specimen, which have a size range from 0.5 mm to 4.76 mm. The amount of aggregates added into the asphalt binder and mastic specimen is controlled by the weight ratio between the asphalt binder and aggregates. Two kinds of asphalt mixture specimens are made in this study. One is the aggregates added into the asphalt binder and the other is aggregates added into asphalt mastic specimens containing 30% fillers. The weight ratio between aggregates and asphalt binder for both of the mixture specimens is 50%.

3.1.4 Fatigue test procedure

When the samples are prepared, the chiller connected with DTT machine is turned on. The ethanol alcohol will fill the bath area and reach the desired test temperature. The samples will be put into the bath area for 1 hour conditioning before the fatigue test. To start a fatigue test, first take out the whole specimen mode from the bath carefully with the assistance of a long clamp and clip, slice two pieces of the fixture away from the specimen, put both the specimen and the bottom plate back into the bath when the fixtures are removed. Slightly tap the two plastic ends to depart the specimen away from the bottom plate, then take out the bottom plate from the bath and use a clip to remove the glassy paper from the bottom of the specimen. Open the test builder software and move the loading pin to a position so that the specimens can be installed at both ends as shown in Figure 3-11. Close the cap of the bath and click "Run" button on the Test Builder window. Follow the procedure described before to finish the fatigue test and save the test results data.

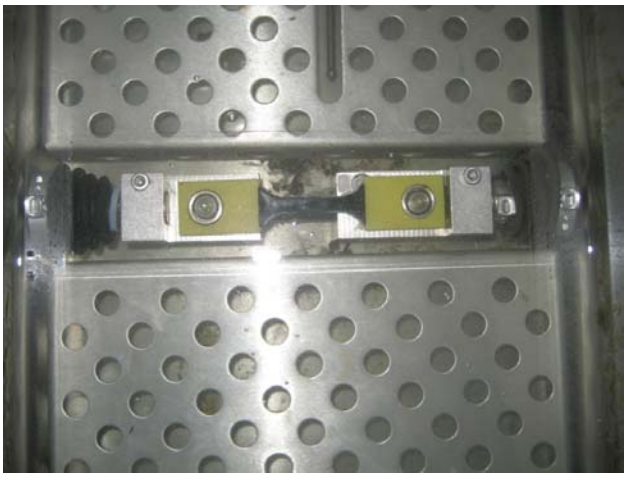

Figure 3-11 Specimen installed in the DTT

3.2 X-ray tomography imaging

The X-ray tomography imaging technique is used as a tool to study the fatigue of asphalt materials. The mastic specimens before and after fatigue test are scanned respectively. The effect of fatigue to the internal structure will be studied. The mixture specimens will also be scanned and compared with mastic specimens to analyze the reason why two materials have different fatigue performances. The internal structures of mastic and mixture specimens will be obtained and reconstructed. The information will be used in the mesh generation of the digital specimen.

The SkyScan 1174 compact micro-CT system shown in the Figure 3-12 is used in this study to scan the asphalt mastic and mixture samples. The procedure to operate the compact micro-CT system is described in the APPENDIX B.

Figure 3-12 Skyscan Micro-CT 1174 system

3.2.1 Scanning of mastic and mixture specimens

Several problems are found when a whole mastic or mixture specimen is scanned shown in the Figure 3-13. First, the specimen deforms very quickly because the temperature of the CT system can not be controlled. The plastic endings attached with specimen also make the specimen easy to deform. The deformed specimen can not be used to conduct the fatigue test any more. Second, if a fixture is used to keep the specimen from deformation as shown in the Figure 3-14, the penetration and detection of the x ray is highly affected and the quality of the scanned image is too low. Considering the limitations described above, the size of the scanning sample has to be controlled so that no large deformation will happen during the scanning process. Before scanning, two samples are prepared using same batch of material, one of which will be used for scanning, while the other one will be used to conduct the fatigue test and scanned after the fatigue test. A 10mm section is carefully marked on the mastic specimen and cut off from the specimen using a heated knife. The section of mastic specimen is put on a small piece of glassy-faced paper and placed on the testing stage for scanning shown as Figure 3-15.

Figure 3-13 Whole mastic specimen to be scanned

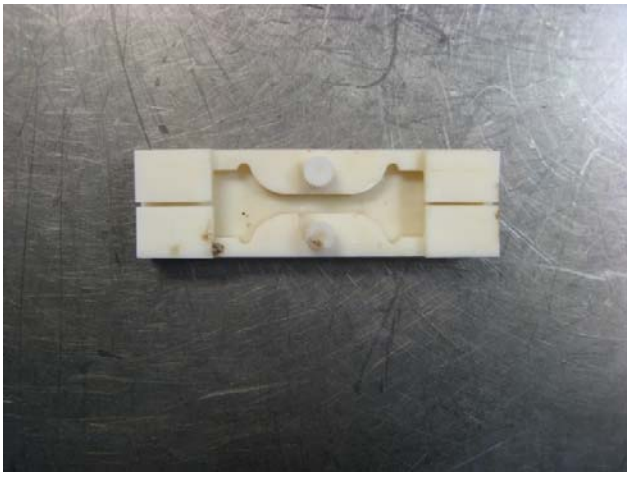

Figure 3-14 Plastic holder

Figure 3-15 Section of the mastic specimen to be scanned

In the scanning option window of the Micro CT 1174 controller, 1 degree is selected for the rotation degree step. 180 degree scanning is used and the number of averaging frames is selected to be 3. These parameters are selected so that the time to finish one scanning of the sample is not too long and the sample will not deform during the scanning. For each kind of mastic and mixture material, six specimens are prepared for every test, three of which are used for scanning before the test and the other three are sued for the fatigue test and scanning after the test.

3.2.2 3-D internal structure reconstruction

Research work has been conducted to incorporating the X-ray tomography into the model generation in FEM. (Dai 2005, 2010; You 2008; Masad 2004; Papagiannakis et al. 2002; Wang et al. 2001, 2004;) The scanned images of the mastic and mixture specimens will be used to generate the mesh of the digital specimens in FEM. The method A Matlab program is developed to process the 2-D scanned images and reconstruct the 3-D structure. Due to the X-ray attenuation difference of each component of the materials, pixels on the images belonging to different components of the mixture have different values. For a binary image, the pixel value range is from 0 to 255, 0 refers to black and 255 refers to white. Generally, dense materials such as aggregates are shown as brighter pixels and the pixel value is close to 255. Air voids with negligible density are shown as darker pixels and the pixel value is close to 0. The binder which has an intermediate density is shown as gray color. Two threshold values need to be determined to discriminate three major components of the asphalt mixture material: air void, binder and aggregates. The higher threshold value determines all the pixels belonging to the aggregates and fillers, while the lower thresh hold value determines all the pixels belong to air voids. The rest pixels with values between the higher and lower threshold values represent the asphalt binder.

An assumption is made that all the pixels with values lower than 70 are belonging to air voids. The lower threshold value is 70. The higher threshold value is determined by a trial and error process. For each mastic or mixture sample, the weights of the asphalt binder, fillers and aggregates are measured. The density of binder is 1.03 g/cm^3 and the density of the quartz fillers and limestone aggregates are assumed to be same, 2.56g/cm^3. A preset higher threshold value is given and all the pixels have value larger than this are counted. All the pixels have pixel value

lower than 70 are also counted. The rest of the pixels are belonging to asphalt binder. Based on the stereology theory introduced before, the volumes of the asphalt binder and aggregates can be obtained respectively. The weight ratio of aggregates and fillers over asphalt binder can be calculated with known densities. Repeat this process as many as necessary until the calculated weight ratio from the image processing is equal to the weight ratio used in the lab test.

The procedure to reconstruct a 3-D internal structure from the scanned 2-D images is described using an example below. In this example, there are 11 scanned images stacked in a 3-D coordinates system shown in the Figure 3-16. The size of each image is 100 by 100, which means there are 10000 pixels on each image.

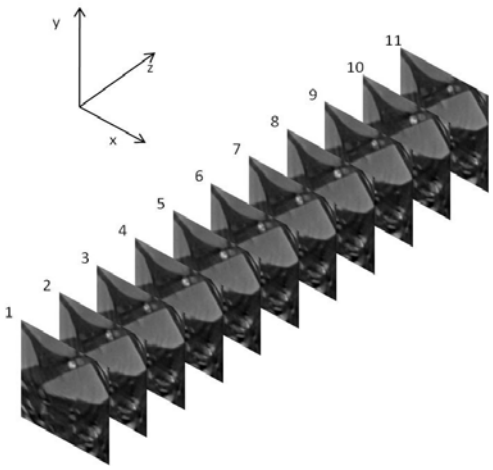

Figure 3-16 Series of scanned images

First, each pixel of an image is numbered. Start from the lower left corner of an image, the first pixel is numbered to be 1. The pixels are numbered from left to right row by row. In this example, there are 100 pixels in each row and column on a single image. The pixels on the first

image are numbered from 1 to 10000. The rest images are also numbered following the same rule.

Second, four corner points of each pixel are considered as nodes and all the nodes on an image are numbered. Start from the lower left corner of the pixel #1, the first node is numbered to be 1. All the nodes are numbered from left to right row by row. In this example, there are 10201 nodes on each image. So, the nodes of the first image are numbered from 1 to 10201. The nodes on the rest images are also numbered following the same rule.

When all the nodes are defined and numbered, the coordinates are assigned for each node. The node #1 is considered as the origin of the coordinate system and its coordinate is (0,0,0). The distance between every two connecting nodes is 1. Following the coordinate directions shown in the Figure 3-16, each node is assigned a coordinate. In the z direction, the distance between every two image is also 1. So, in this example, the z-coordinate is ranging from 0 to 10.

Since the 3-D reconstruction from the 2-D scanned images will be used to generate the mesh for FEM modeling, the element of the FEM model needs to be defined. It is easy to generate an 8 nodes brick element because the nodes are numbered and the coordinates are also assigned. The basic shape of an element is cubic. Two pixels whose nodes have same x and y coordinates on two connecting images are forming the front and back surfaces of a brick element. In this example, there are 10000 elements generated in every two connecting images. For a series of 11 images, there are 100000 elements generated in total.

In the FEM modeling, different components are treated as different materials. The material property of the element generated in the previous step is determined by its front surface, which

means the pixel value of the front surface determines what kind of material this element belongs to. The number of element is same with the number of front pixel.

Finally, the "Patch" method is used to achieve the visualization of the reconstructed internal structure. The 8-nodes brick element generated in the previous step is composed of 6 surfaces, the numbers of four nodes on each surface and their coordinates are already defined. With known nodes information, every surface of an element can be drawn and patch together. In this example, the 3-D reconstructed structure from 11 2-D scanned images is shown in Figure 3-17.

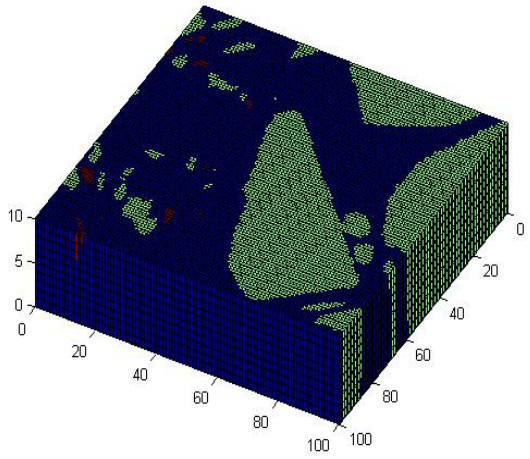

Figure 3-17 Visualization of a reconstructed structure

3.3 Simulation of fatigue based on FEM

The fatigue process of asphalt binder, mastic and mixture under cyclic loading is simulated based on FEM. Asphalt binder is treated as homogenous elasto-plastic material. Asphalt mastic and mixture are treated as composite materials in which the fillers and aggregates are treated as elastic material and the asphalt binder is treated as elasto-plastic material. The air voids elements will be removed in the simulation. The internal structures of both materials are obtained from the

3-D reconstruction described previously. The boundary condition of the simulation is same with the lab test that the specimen is fixed at one end and the loading is applied on the other end of the specimen shown in Figure 3-18. The loading applied on the specimen is a cyclic loading controlled by periodic amplitude with a format shown in Equation 3-1.

$$F = F_0(A_0 + A_1 \sin \omega(t - t_0)) \tag{3-1}$$

in which F is the applied load. F_0 is the initial loading level. A_0 A_1 t_0 are user defined constants and ω is the frequency of the sinusoidal curve.

Direct cyclic analysis method is used to obtain the response of the material after certain number of loading cycles. The damage parameter is incorporated to model the degradation of the elastic modulus of asphalt binder caused by fatigue damage. The axial strain of the center node on the loading surface is measured to compare with the experiment results.

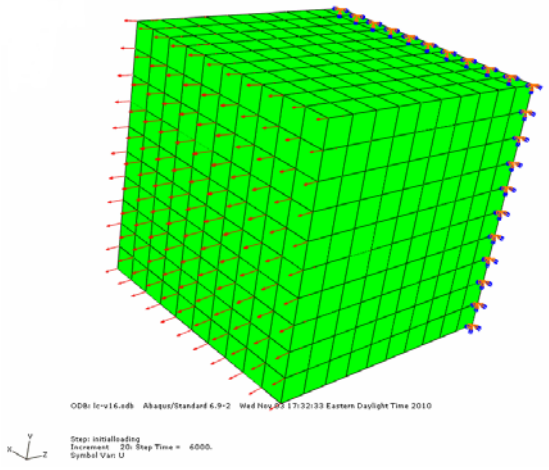

Figure 3-18 Boundary condition of the fatigue modeling

Chapter 4. Fatigue test of asphalt binder, mastic and mixture

4.1 Fatigue of asphalt binder

4.1.1 Introduction

The peak value of cyclic loading applied on the asphalt binder specimen is determined by direct tension test. The tensile strength of three asphalt binder specimens is measured at desired test temperature which is -20^{o}C in this study. The average maximum tensile loading is calculated. The peak value of the cyclic loading is chosen to be about 75% of the average maximum tensile loading. The direct tension test is conducted following the procedure TP3-98 provided by American Association of State Highway and Transportation Officials (AASHTO). The effective cross section area of the specimen is $36\times10^{-6}\,\mathrm{m}^2$. After the peak value of cyclic loading is determined, another three asphalt binder specimens are prepared for fatigue test.

4.1.2 Direct tension test results

The direct tension test results of three asphalt binder specimens at -20 ^{o}C are listed in Table 1 of Appendix C. The maximum tensile loading is calculated by multiplying the maximum stress with the effective cross section area of the specimen. The average maximum loading of three specimens is calculated. Based on the test results below, the average maximum tensile loading can be applied on the asphalt binder specimen is 26.03N at -20 ^{o}C. The peak value of the cyclic loading is chosen to be 75% of the maximum tensile loading, which is 20N. This value is input to the designed fatigue test procedure.

4.1.3 Fatigue test results of asphalt binder under different loading level

The magnitude of the cyclic loading level is a critical factor to the fatigue behavior of asphalt binder. To address this effect, the asphalt binder specimens are tested at three different loading levels, 20N, 15N and 10N respectively. For all three loading levels, the test temperature is -20^{o}C and loading rate is 0.5Hz. The cyclic loading is applied until the specimen fails. Test results of asphalt binder at 20N level are shown in the Figure 4-1 below. The loading history is shown in the left column and the calculated axial strain versus the number of loading cycles is shown in the right column. The final strain when the specimens fail and corresponding number of loading cycles are listed in the Table 4-1 followed. The average final strain of three specimens is 0.0059 and average number of cycles is 105. It can be seen from the results that the axial strain of the asphalt binder specimen keep increasing during the whole loading process, and the asphalt binder is easy to fail at this test condition.

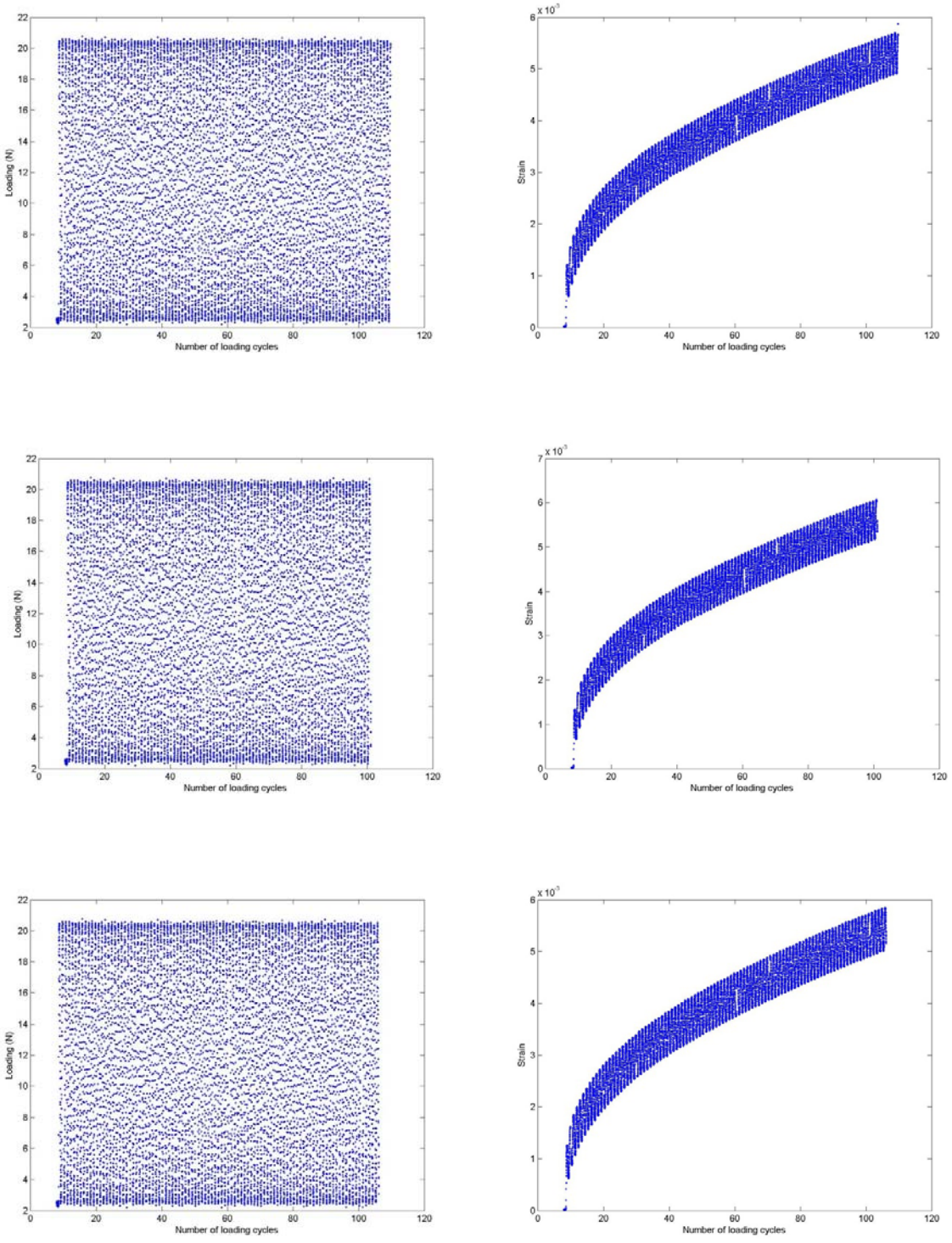

Figure 4-1 Loading history and axial strain of three asphalt binder specimens

Table 4-1 Fatigue test results of asphalt binder under 20N

Specimens	Loading Level (N)	Final strain	Number of loading cycle
Asphalt binder #1	20	0.0056	109
Asphalt binder #2	20	0.0062	100
Asphalt binder #3	20	0.0058	105

Three asphalt binder specimens are tested at 15N and 10N loading levels respectively. The axial strains of the specimens over the fatigue test process are shown in Figure 4-2 and Figure 4-3. The measured final strain and corresponding number of loading cycles are listed in Table 4-2 and Table 4-3.

Table 4-2 Fatigue test results of asphalt binder under 15N

Specimens	Loading Level (N)	Final strain	Number of loading cycle
Asphalt binder #1	15	0.018	3997
Asphalt binder #2	15	0.022	3700
Asphalt binder #3	15	0.017	3970

Table 4-3 Fatigue test results of asphalt binder under 10N

Specimens	Loading Level (N)	Final strain	Number of loading cycle
Asphalt binder #1	10	0.024	10059
Asphalt binder #2	10	0.023	9994
Asphalt binder #3	10	0.023	9164

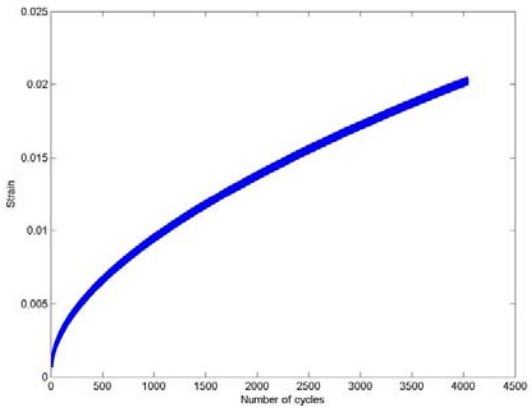

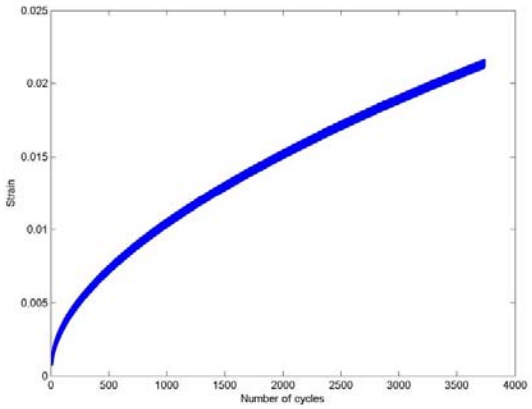

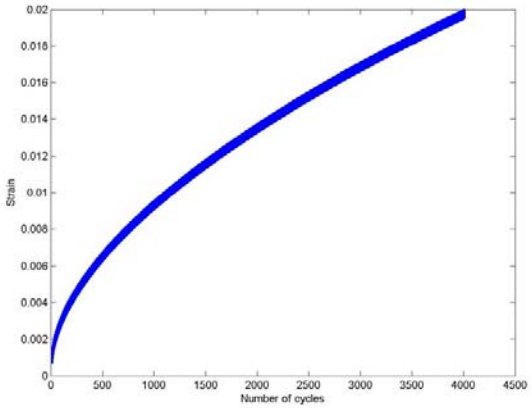

Figure 4-2 Axial strain of three asphalt binder specimens under 15N

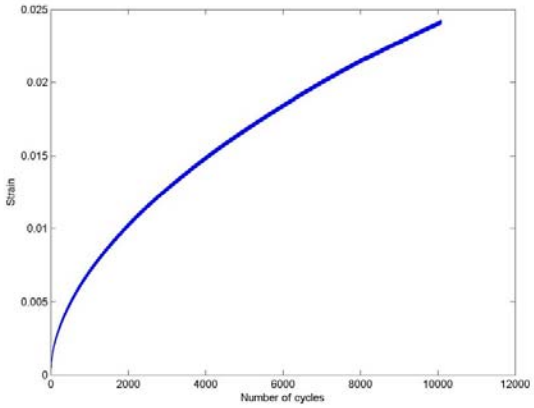

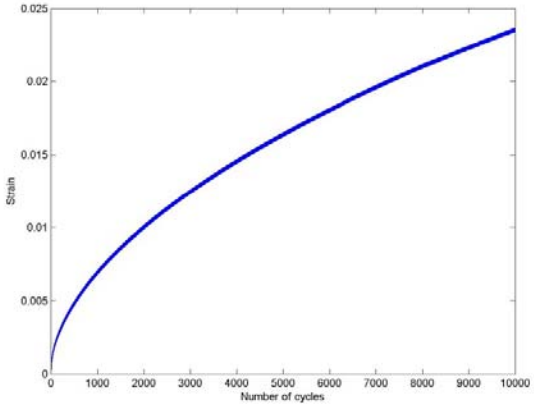

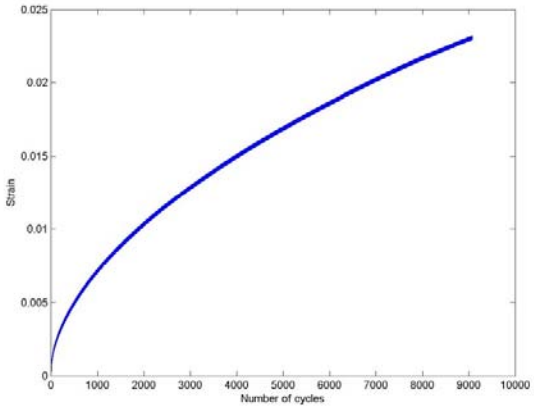

Figure 4-3 Axial strain of three asphalt binder specimens under 10N

The average final strain and number of loading cycles for three loading levels are listed in the Table 4-4.Their relationships with the three loading levels are plotted in Figure 4-4 and Figure 4-5 respectively. It can be seen from the results that the fatigue behavior of the asphalt binder specimen is significantly affected by the magnitude of cyclic loading. Both the final strain and number of loading cycle increase as the peak value of the cyclic loading decreases. From 20 N to 10N, the peak value decreases to the half, the average final strain increases about 4 times from 0.0059 to 0.023, and the average number of loading cycle increases about 100 times from 105 to 9739. The results indicate that the fatigue life of the asphalt binder is closely related with magnitude of the cyclic loading.

Table 4-4 Fatigue test results of asphalt binder in three loading levels

Loading level (N)	Average final strain	Average number of loading cycle
20	0.0059	105
15	0.019	3889
10	0.023	9739

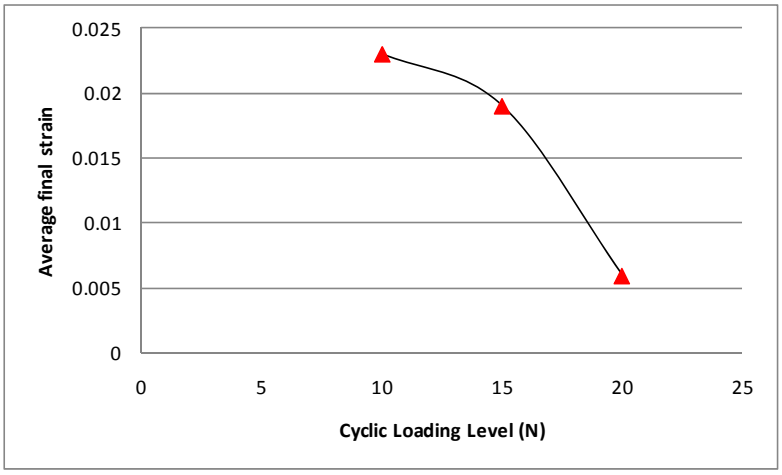

Figure 4-4 Average final strain under three loading levels

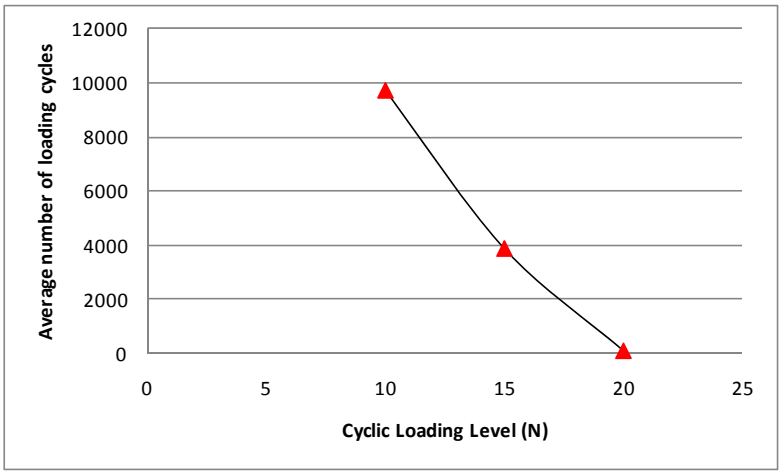

Figure 4-5 Average number of loading cycles under three loading levels

4.1.4 Fatigue test results of asphalt binder under different temperature

Temperature is an important factor to affect the behavior of asphalt binder. To evaluate the effect of the temperature to the fatigue behavior, asphalt binder specimens are tested under three different temperatures: -10^{o}C, -15^{o}C and -20^{o}C respectively. The temperature of the test is controlled by the chiller system. At each temperature, three asphalt binder specimens are tested. The magnitude of the cyclic loading is 20N and the load rate is 0.5 Hz for all three temperatures. The test results of asphalt binder at -20^{o}C are shown previous. The axial strains of the specimens over the fatigue test process at -10^{o}C and -15^{o}C are shown in Figure 4-6 and Figure 4-7 below. The final strain before the specimens fail and number of loading cycle are listed in the Table 4-5 and Table 4-6 followed.

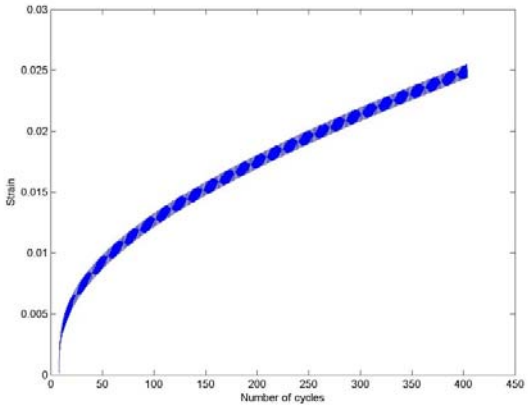

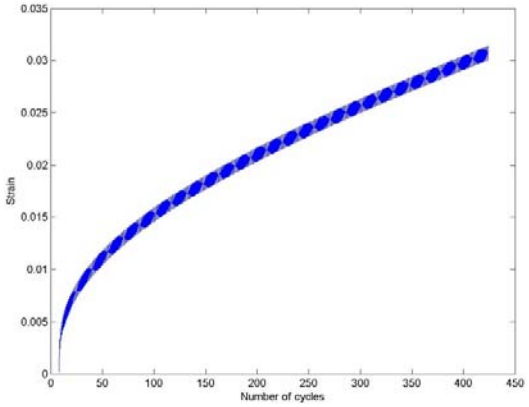

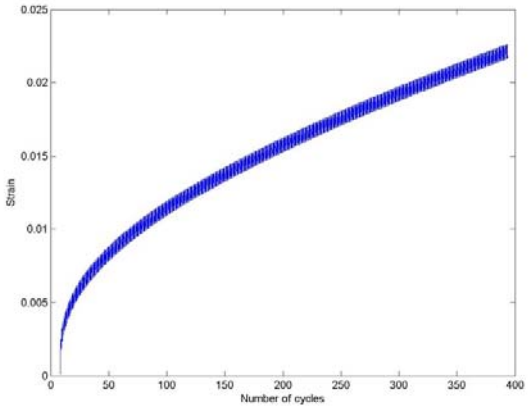

Figure 4-6 Axial strain of three asphalt binder specimens at -15 ^{o}C

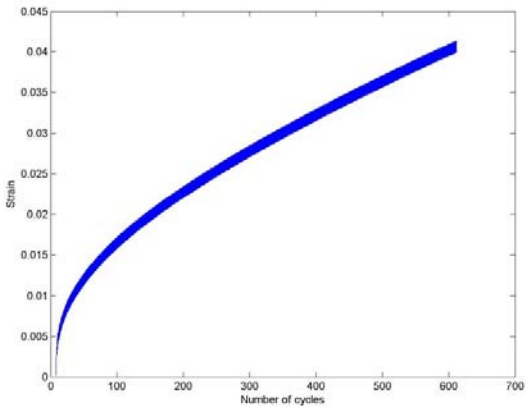

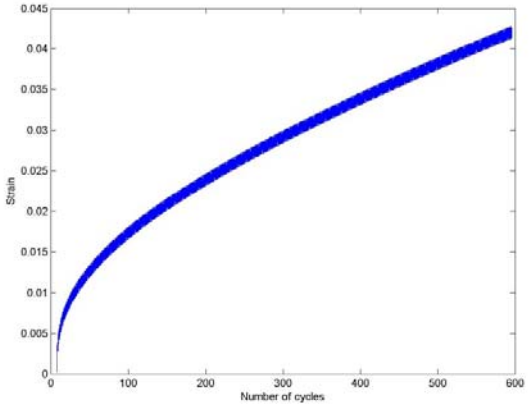

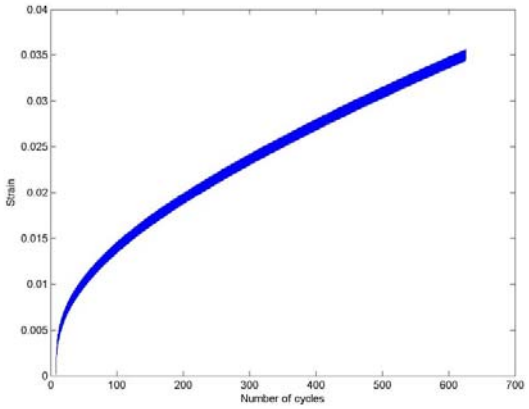

Figure 4-7 Axial strain of three asphalt binder specimens at -10 ^{o}C

Table 4-5 Fatigue test results of asphalt binder specimens at -15 °C

Specimens	Test temperature (°C)	Final strain	Number of loading cycle
Asphalt binder #1	-15	0.025	400
Asphalt binder #2	-15	0.031	420
Asphalt binder #3	-15	0.023	390

Table 4-6 Fatigue test results of asphalt binder specimens at -10 °C

Specimens	Test temperature (°C)	Final strain	Number of loading cycle
Asphalt binder #1	-10	0.046	606
Asphalt binder #2	-10	0.048	589
Asphalt binder #3	-10	0.036	624

The average final strain and number of loading cycle of three specimens at each temperature are calculated and shown in Table 4-7. Their relationships with test temperature are shown in Figure 4-8 and Figure 4-9 respectively. It can be seen from the results that the temperature has significant impacts on the fatigue behaviors of the asphalt binder. Both the final strain and number of loading increase as the temperature increases. From -20 °C to -10°C, the temperature is twice higher, the average final strain increases to seven times larger and the average number of loading cycles increases to about six times larger.

Table 4-7 Average results of asphalt binder at three temperatures

Test temperature (°C)	Average final strain	Average number of loading cycle
-10	0.043	606
-15	0.026	403
-20	0.0059	105

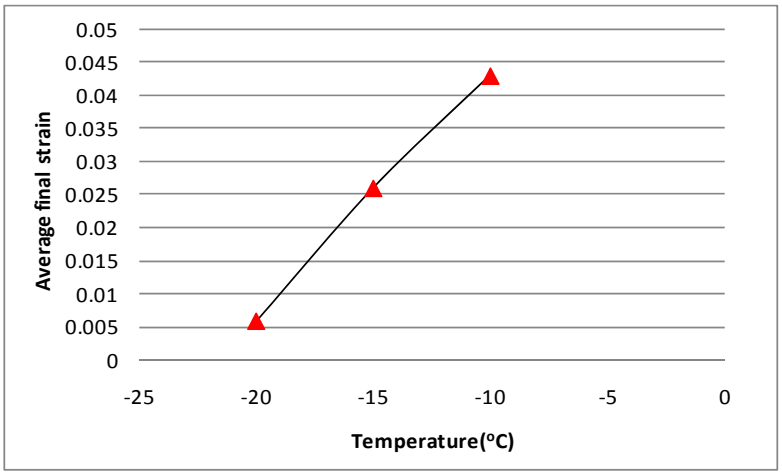

Figure 4-8 Average final strain at three temperatures

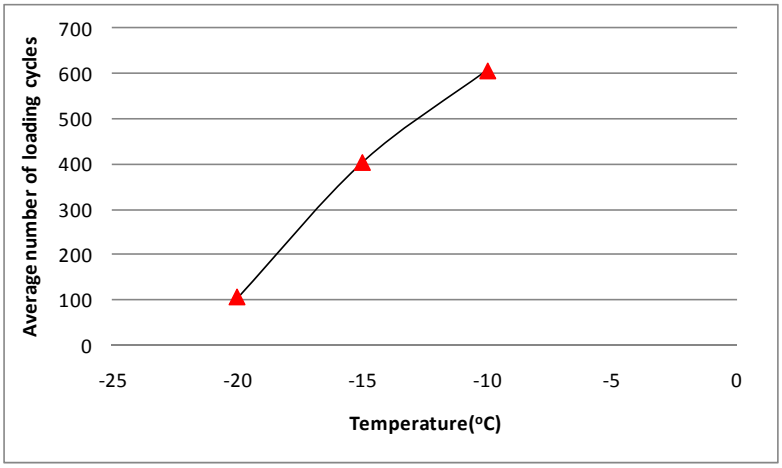

Figure 4-9 Average number of loading cycles at three temperatures

4.1.5 Fatigue test results of asphalt binder under different loading rates

The effect of loading rate to the fatigue behavior of the asphalt binder at low temperature is estimated by adjusting the frequency of the cyclic loading in the self-designed fatigue procedure. The asphalt binder specimens are tested at three different loading rates: 0.5Hz, 1Hz and 2Hz respectively. At each loading frequency, three specimens are tested. The magnitude of the cyclic loading is 20N and the test temperature is -20^{o}C for all three loading rates. The test results of

asphalt binder at 0.5Hz are shown previously. The axial strains of the specimens over the fatigue test at 1Hz and 2Hz are shown in Figure 4-10 and Figure 4-11 below. The final strain before the specimens fail and number of loading cycle are listed in the Table 4-8 and Table 4-9.

Table 4-8 Fatigue test results of asphalt binder specimens at 1Hz

Specimens	Loading rate (Hz)	Final strain	Number of loading cycle
Asphalt binder #1	1	0.0056	100
Asphalt binder #2	1	0.0059	95
Asphalt binder #3	1	0.0058	106

Table 4-9 Fatigue test results of asphalt binder specimens at 2Hz

Specimens	Loading rate (Hz)	Final strain	Number of loading cycle
Asphalt binder #1	2	0.0052	92
Asphalt binder #2	2	0.0049	89
Asphalt binder #3	2	0.0047	82

The average final strain and number of loading cycle of three specimens at each loading rate are calculated and shown in Table 4-10. Their relationships with loading rate are shown in Figure 4-12 and Figure 4-13 respectively. Compared with magnitude of cyclic loading and test temperature, the loading rate is not a significant factor to affect the fatigue resistance of the asphalt binder at low temperature. The final strain and number of loading slightly decrease as the loading rate increase. From 0.5Hz to 2Hz, the loading rate increases to 4 times larger, while the average final strain decreases 17%, the average number of loading cycle decreases 16%.

Table 4-10 Average fatigue test results of asphalt binder at three loading rates

Loading rate (Hz)	Average final strain	Average number of loading cycle
0.5	0.0059	105
1	0.0058	100
2	0.0049	88

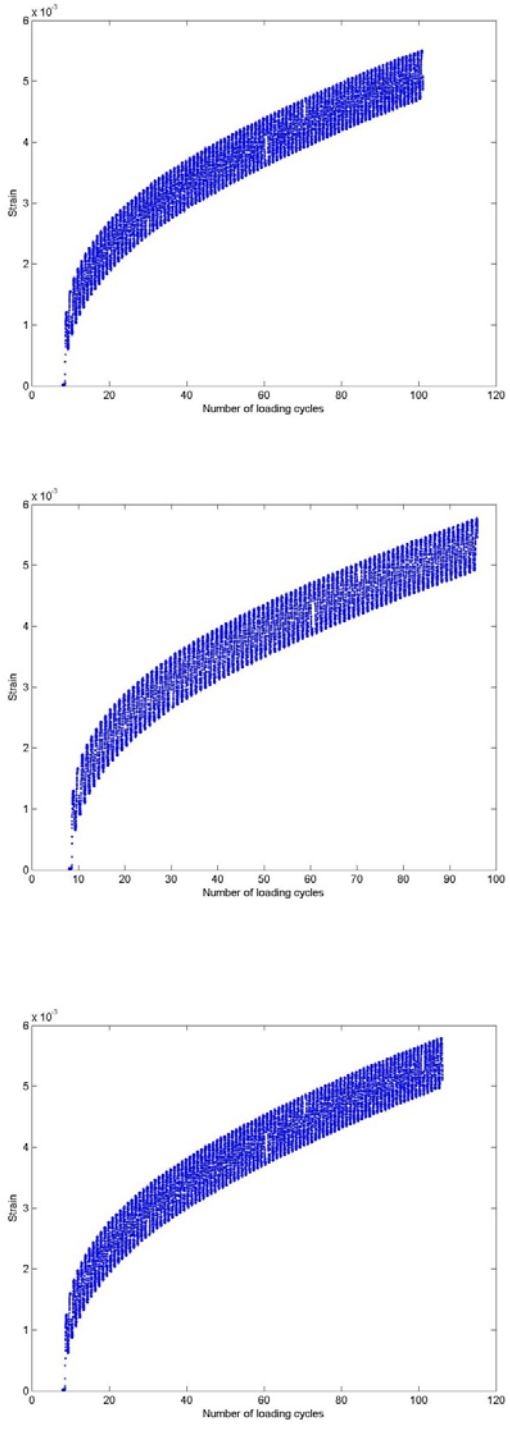

Figure 4-10 Axial strain of three asphalt binder specimens at 1 Hz

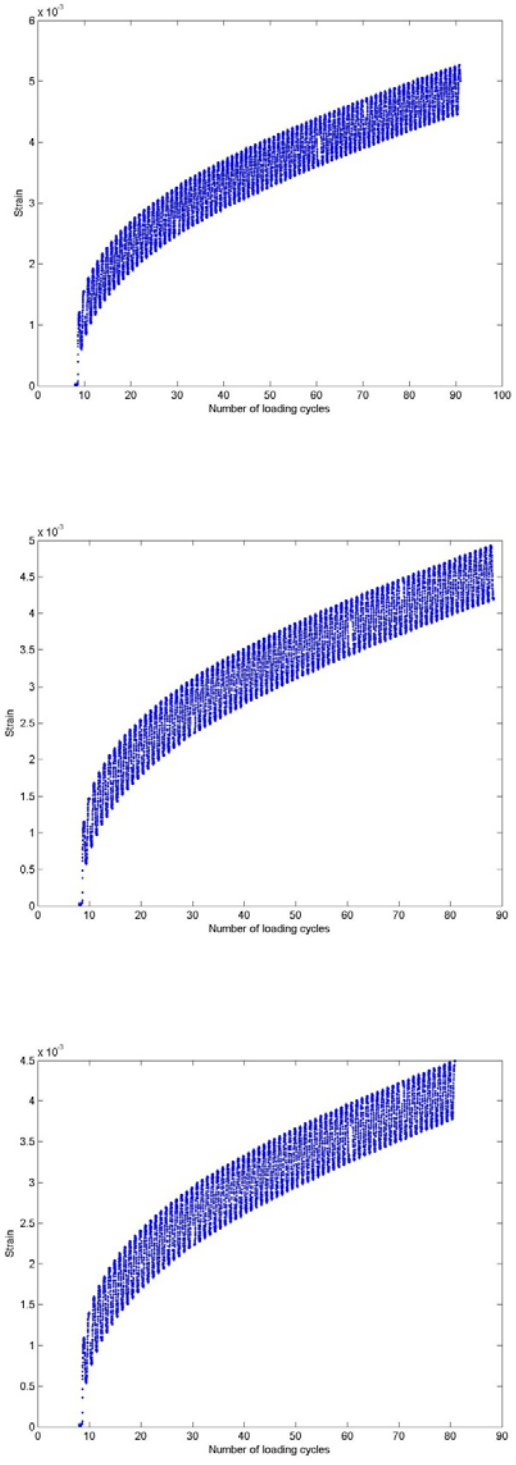

Figure 4-11 Axial strain of three asphalt binder specimens at 2 Hz

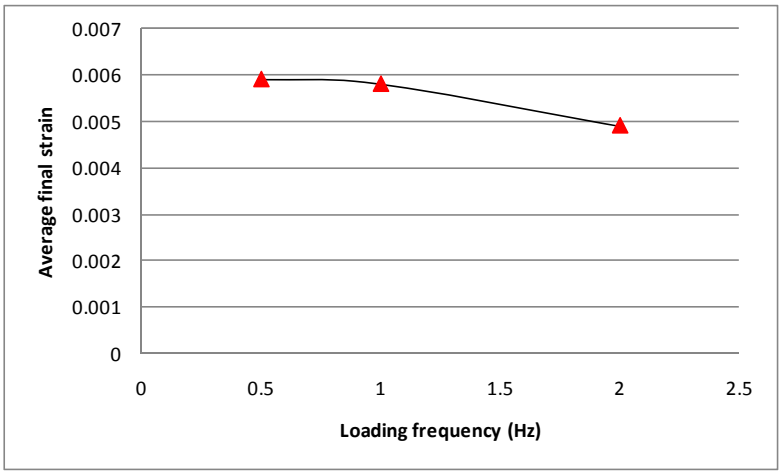

Figure 4-12 Average final strain of asphalt binder at three loading rates

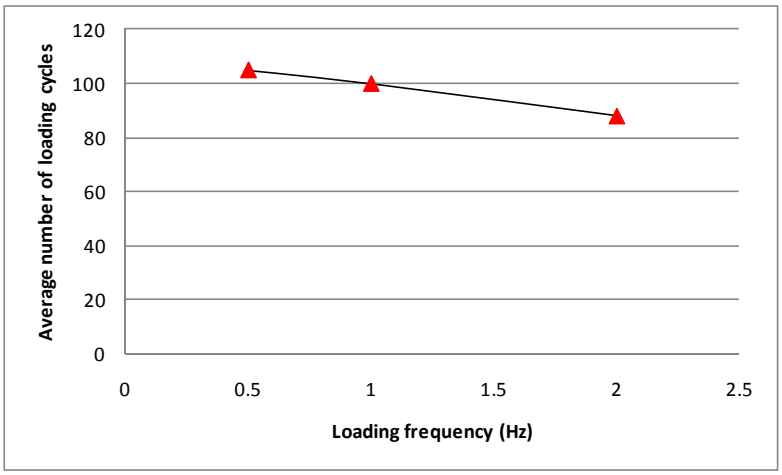

Figure 4-13 Average number of loading cycles at three loading rates

The tests described above show the fatigue test results of asphalt binder fatigue at different loading levels, test temperatures and loading rates. It is shown that both the loading magnitude and test temperature have significant impacts on the fatigue behavior of the asphalt binder. However, at low temperature, loading rate does not affect the fatigue behavior of the asphalt binder as much as loading level and test temperature. It is also found that, at -20^{o}C and 20N loading level, the asphalt binder is very easy to fail under cyclic loading, the average final strain

is 0.0059 and the average number of loading cycle is 105. This test temperature and loading magnitude will be used for further fatigue test of asphalt mastic and mixture so that behaviors of three kinds of materials can be compared at same condition. Since the loading rate is not a significant factor to affect the behavior of asphalt binder at -20^{o}C, 0.5Hz will be used for all the further fatigue tests of asphalt mastic and mixture.

4.2 Fatigue of asphalt mastic

4.2.1 Introduction

A major component of the binding medium among aggregates is asphalt mastic. It is asphalt binder mixed with fine aggregates which are generally called fillers. In this study, mastic specimen is prepared by mixing asphalt binder with fillers which can pass through the #200 sieve; the size of filler is less than 0.075mm. Similar with the fatigue tests of asphalt binder samples, the mastic samples are prepared and tested using self-designed fatigue test procedure.

The asphalt binder PG70-22 binder is used to prepare the mastic specimen. The filler is quartz material. The filler content is controlled by the weight ratio between the fillers and asphalt binder. Nine kinds of asphalt mastic specimens with different filler content are prepared: 10%, 15%, 20%, 25%, 30%, 35%, 40%, 45% and 50%. The asphalt binder and filler are weighted respectively and mixed in the oven at 320^{o}F. The asphalt mastic is stirred all the time when poured into the sample mode to make the fillers uniformly distributed.

4.2.2 Fatigue test results of asphalt mastic

Three specimens are prepared and tested for each kind of asphalt mastic. The final strain and number of loading cycle before the specimen fail are recorded. The results are listed below from Table 4-11. The average final strain and number of load cycles for each kind of asphalt mastic are listed in the Table 4-12. Their relationship with mastic filler content is plotted in the Figure 4-14 and Figure 4-15 respectively.

Table 4-11 Fatigue test of different mastic specimens

Specimens	Filler content	Final Strain	Number of cycles
Mastic #1	10%	0.0467	10453
Mastic #2	10%	0.0496	9894
Mastic #3	10%	0.0461	11330
Mastic #4	15%	0.0536	13424
Mastic #5	15%	0.0562	13038
Mastic #6	15%	0.0511	12965
Mastic #7	20%	0.0553	16383
Mastic #8	20%	0.0627	16702
Mastic #9	20%	0.0582	16100
Mastic #10	25%	0.0595	17634
Mastic #11	25%	0.0609	17035
Mastic #12	25%	0.0581	17921
Mastic #13	30%	0.0682	19634
Mastic #14	30%	0.0714	18569
Mastic #15	30%	0.0657	19422
Mastic #16	35%	0.0635	18725
Mastic #17	35%	0.0688	18209
Mastic #18	35%	0.0676	18653
Mastic #19	40%	0.0628	17727
Mastic #20	40%	0.0705	17200
Mastic #21	40%	0.0625	17444
Mastic #22	45%	0.0614	16072
Mastic #23	45%	0.0598	16724
Mastic #24	45%	0.0663	16457
Mastic #25	50%	0.0592	15179
Mastic #26	50%	0.0602	15728
Mastic #27	50%	0.0584	15547

Table 4-12 Average results of different asphalt mastic specimens

Mastic filler content	Average final strain	Average number of load cycle
10%	0.0475	10559
15%	0.0536	13142
20%	0.0587	16395
25%	0.066	17531
30%	0.0684	19208
35%	0.0666	18529
40%	0.0652	17457
45%	0.0614	16417
50%	0.0592	15484

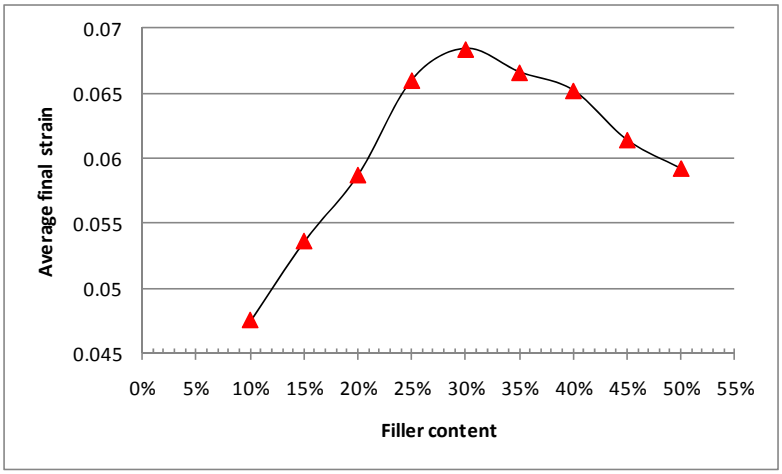

Figure 4-14 Average final strain of each kind of asphalt mastic specimen

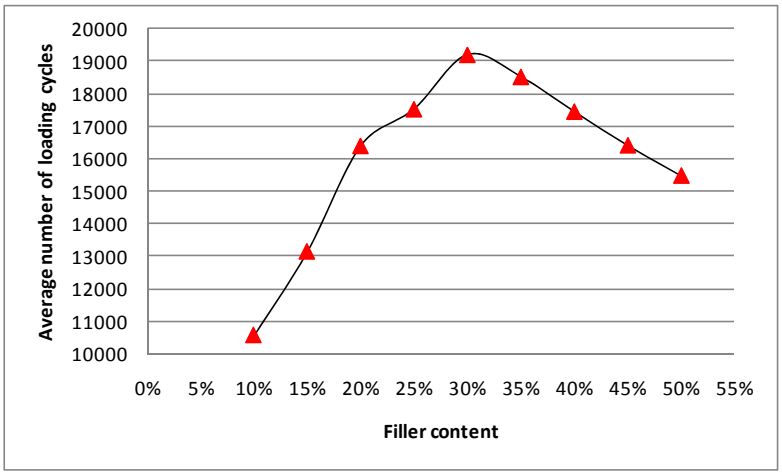

Figure 4-15 Average number of loading cycles of each kind of asphalt mastic specimen

The fatigue test results of different asphalt mastic show that the introduction of the fillers changes the fatigue property of the asphalt binder significantly. Both the final strain and the number of loading cycles are increased to a large extent. The final strain and the number of loading cycles before a mastic specimen fail is much larger than the asphalt binder specimens. It is also found that the fatigue resistance of the mastic is not linearly increase as the filler content increase. The average final strain and number of loading cycles reach the maximum values when the mastic contains 30% of fillers. The optimum filler content for asphalt mastic specimen is about 30% of asphalt binder.

4.3 Fatigue of asphalt mixture

4.3.1 Introduction

Two kinds of asphalt mixture samples are prepared for fatigue test. One is asphalt binder mixed with limestone aggregates only, while the other is asphalt binder mixed with 30% filler and limestone aggregates. As mentioned before, the size of the sample mode is limited so the

aggregates used to make the mixture samples are also controlled. The aggregates passing through the No.4 sieve but retained on the No.35 sieve are used to make the asphalt mixture specimen. The size range of the aggregates is from 0.5mm to 4.75mm. The amount of aggregates added into the asphalt binder is controlled by the weight ratio between aggregates and asphalt binder. In this study, 50% is used for both kinds of mixture. The loading magnitude, test temperature and the loading rate are same with previous tests for asphalt binder and mastic. The cyclic loading level is 20N, the test temperature is -20^{o}C and the loading rate of the cyclic loading is 0.5Hz.

4.3.2 Fatigue test results of asphalt mixture

Three specimens are prepared and tested for each kind of asphalt mixture. The axial strains of each kind of specimen over the fatigue test are shown in the Figure 16 and Figure 17. The measured final strain and number of loading cycle are listed in the Table 4-13 and Table 4-14. The average final strain and number of loading cycles for each kind of asphalt mixture are listed in the Table 4-15.

Table 4-13 Fatigue test results of asphalt mixture specimens without filler

Specimens	Filler content	Final Strain	Number of cycles
Mix #1	0	0.0121	1715
Mix #2	0	0.0128	1700
Mix #3	0	0.0124	1615

Table 4-14 Fatigue test results of asphalt mixture specimens with 30% filler

Specimens	Filler content	Final Strain	Number of cycles
Mix #1	30%	0.0462	12574
Mix #2	30%	0.0474	12139
Mix #3	30%	0.0442	11967

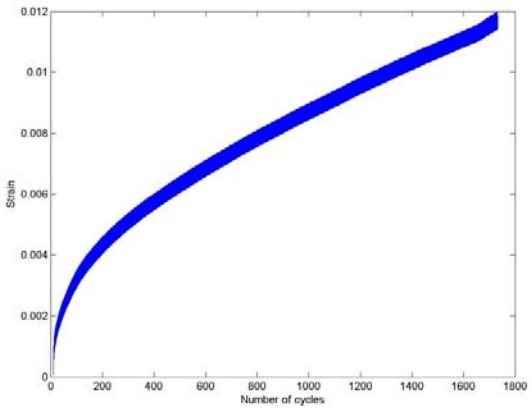

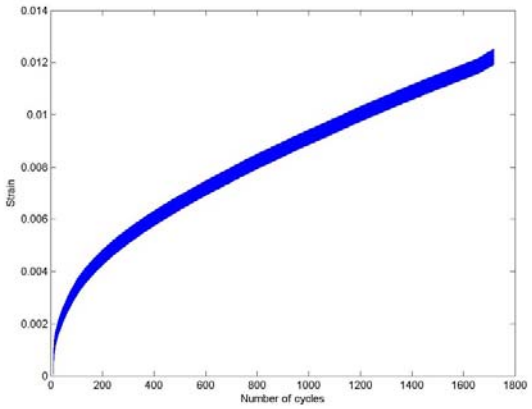

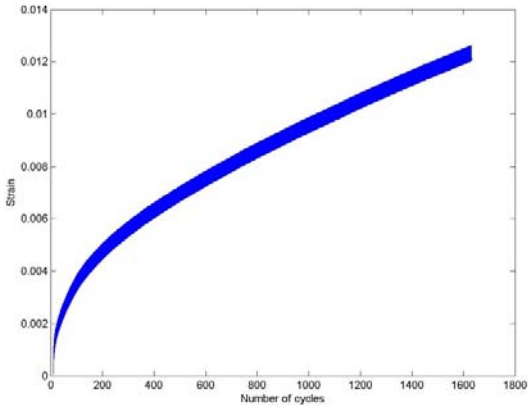

Figure 4-16 Axial strain of asphalt mixture specimens with no filler

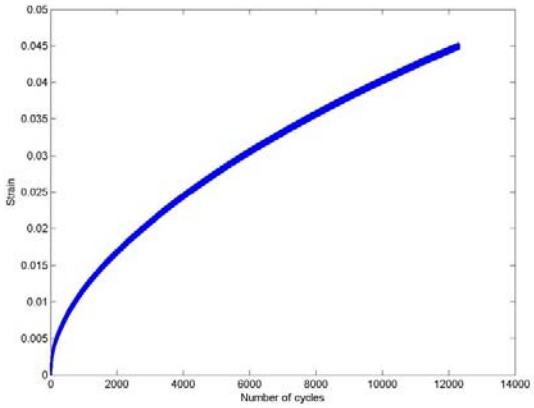

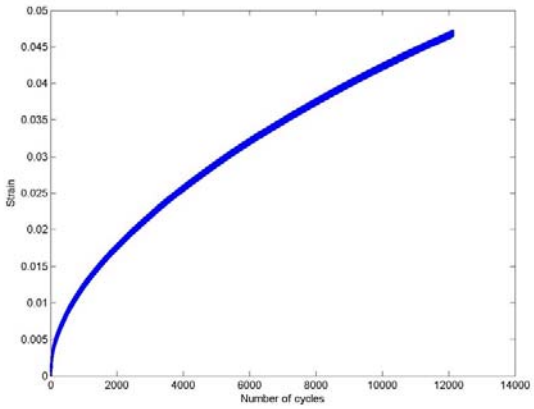

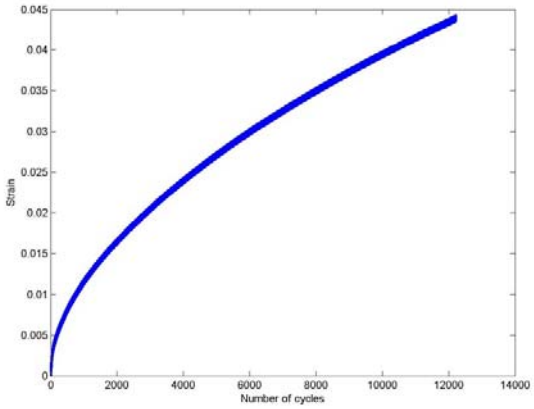

Figure 4-17 Axial strain of asphalt mixture specimens with 30% filler

Table 4-15 Average fatigue test results of two kinds of asphalt mixture specimens

Specimens	Average final strain	Average number of loading cycles
Mixture with no filler	0.0124	1677
Mixture with 30% filler	0.0459	12227

It is found that the addition of aggregates into the asphalt binder improves the fatigue resistance of asphalt binder. However, the performances of asphalt mixture are very different due to the addition of the fillers. Both the average final strain and the number of loading cycles for asphalt mixture contain 30% fillers are much larger than the asphalt mixture without fillers. This indicates that the addition of the fillers strengthen the material and form a better skeleton together with aggregates.

The average fatigue test results of asphalt binder, mastic and mixture are listed in the Table 4-16 below. It can be seen that although both the fillers and aggregates added into the asphalt binder can improve the fatigue resistance of the material, the fatigue performances of the asphalt mastic and mixture are very different. Introduction of large size aggregates does not necessarily improve the fatigue resistance of the material as expected. As shown in the table, the average final strain of the asphalt mixture containing 30% filler is smaller than all nine kinds of asphalt mastic specimen. The number of loading cycles is smaller than all the asphalt mastic specimens containing 15% above fillers. This indicates that the addition of large size aggregates changes the property of the mastic and makes the specimen vulnerable to the fatigue loading. However, compared with the asphalt mixture specimen without fillers added, the asphalt mixture containing 30% filler shows much better fatigue performance. Both the comparisons indicate that the fillers improve the fatigue resistance of the material, but when the large size aggregates are added, the material becomes vulnerable to the fatigue loading. A possible reason of this

phenomenon is that, compared with filler, the bonding between the asphalt binder and aggregate is not so tight that more air voids are introduced. These air voids behaves like initial micro cracks and make the material easier to fail under fatigue loading.

Table 4-16 Average fatigue test results of asphalt binder, mastic and mixture specimens

Specimens	Average final strain	Average number of load cycle
Asphalt binder	0.0059	105
Mastic containing 10% filler	0.0475	10559
Mastic containing 15% filler	0.0536	13142
Mastic containing 20% filler	0.0587	16395
Mastic containing 25% filler	0.066	17531
Mastic containing 30% filler	0.0684	19208
Mastic containing 35% filler	0.0666	18529
Mastic containing 40% filler	0.0652	17457
Mastic containing 45% filler	0.0614	16417
Mastic containing 50% filler	0.0592	15484
Mixture without filler	0.0124	1976
Mixture with 30% filler	0.0459	12226

Chapter 5. Fatigue analysis using x-ray tomography

X-ray tomography technique is used in this study to: analyze the internal structure change of the asphalt mastic specimen caused by fatigue loading; estimate the difference of the internal structure between asphalt mastic and mixture; obtain the 2D scanned images of asphalt mastic and mixture for further 3D reconstruction. As introduced in chapter 3, compact micro-CT system Skyscan 1174 is used in this study for x-ray scanning.

5.1 X-ray scanning of asphalt mastic before and after test

5.1.1 Introduction

The asphalt mastic specimens are scanned before and after the fatigue test to analyze the structure change caused by the fatigue loading. Asphalt mastic specimens containing 20%, 30% and 40% fillers are chosen to be scanned. For each kind of asphalt mastic, six specimens are prepared. Three specimens are scanned before the fatigue test, while the other three specimens are scanned after certain number of loading cycles before they fail. As described in chapter 3, only one section of the specimen will be used for scanning. After the asphalt mastic specimen is prepared and conditioned in the test bath at desired temperature for one hour, the loading end of the sample mode is marked shown in the Figure 5-1. A 10mm long section is cut off from a same position of the specimen using a heated knife, which 15 mm away from the marked end. Three sections are cut off from the asphalt mastic specimens before the fatigue test. The other three specimens are tested and taken out after 10000 loading cycles are applied. Then sections

are cut off from the tested specimens and scanned. A scanned asphalt mastic section is shown in Figure 5-2.

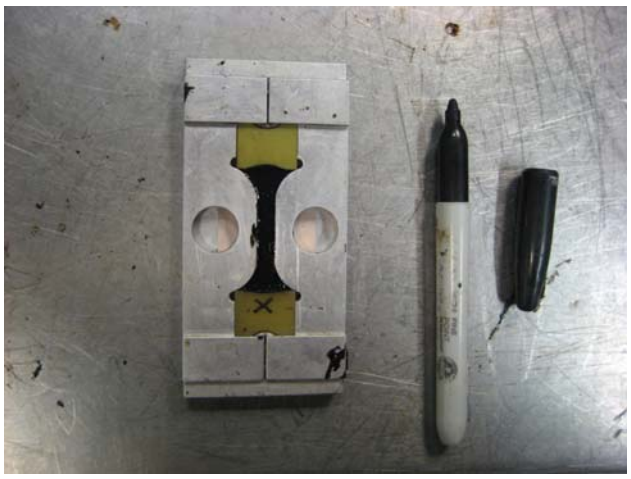

Figure 5-1 Marked end of the specimen

Figure 5-2 Asphalt mastic section to be scanned

5.1.2 Results and discussion

Three vertical cut view images are obtained for each asphalt mastic section before and after fatigue test. The average pixel values of each image are measured and the standard deviation is

calculated based on the Equation 5-1. The standard deviations of image pixel values are compared for the specimens before and after the fatigue test.

$$s = (\frac{1}{n}\sum_{i=1}^{n}(x_i - \overline{x})^2)^{\frac{1}{2}} \tag{5-1}$$

where

$$\overline{x} = \frac{1}{n}\sum_{i=1}^{n} x_i \tag{5-2}$$

x_i is the pixel value of each pixel and n is the number of pixels on the image. Three kinds of mastic specimens are scanned: 20% filler mastic, 30% filler mastic and 40% filler mastic. The vertical cut view images of specimens before and after test are shown in the Figure 5-3 to Figure 5-20 below. The calculated standard deviations of the pixel values for each image and average values are listed in the Table 5-1to Table 5-3 followed respectively.

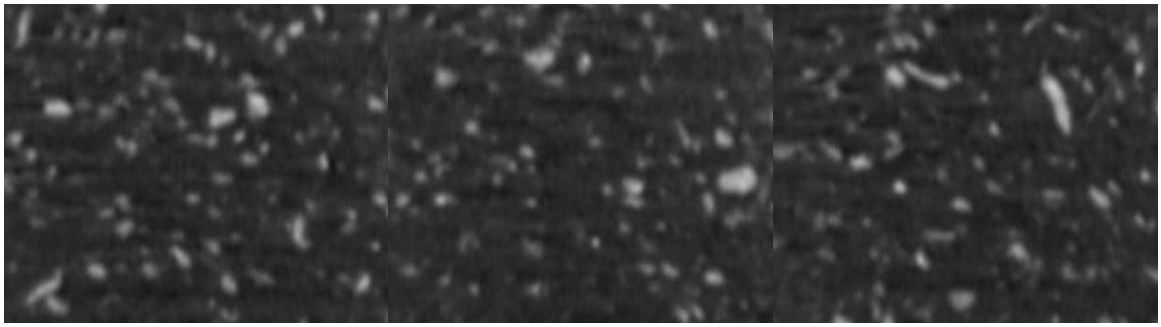

Figure 5-3 20% filler mastic before fatigue test-specimen #1

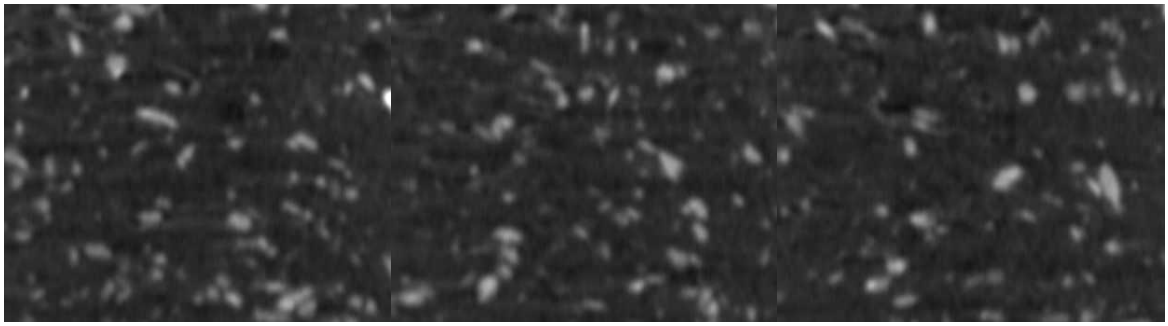

Figure 5-4 20% filler mastic before fatigue test-specimen #2

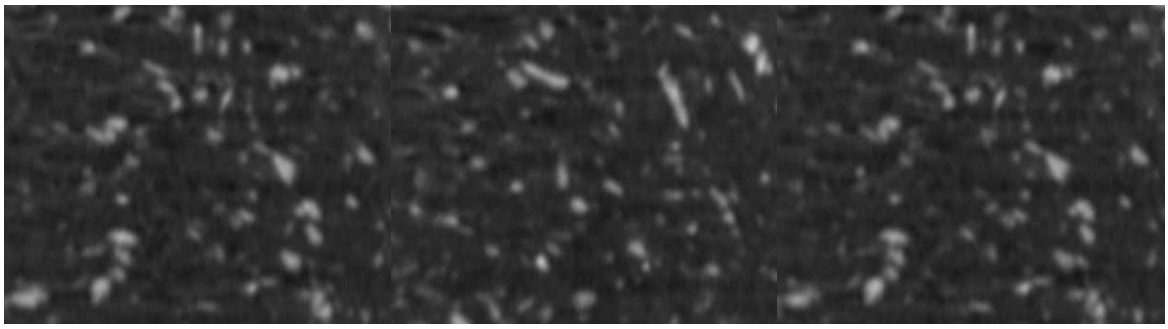

Figure 5-5 20% filler mastic before fatigue test-specimen #3

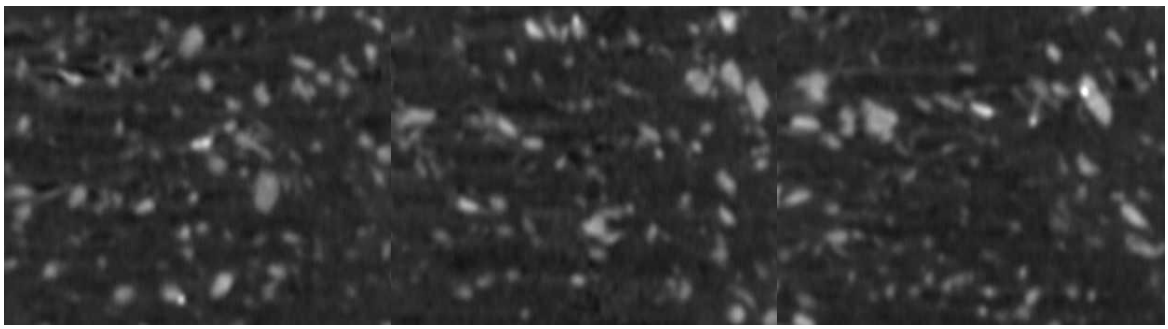

Figure 5-6 20% filler mastic after fatigue test-specimen #4

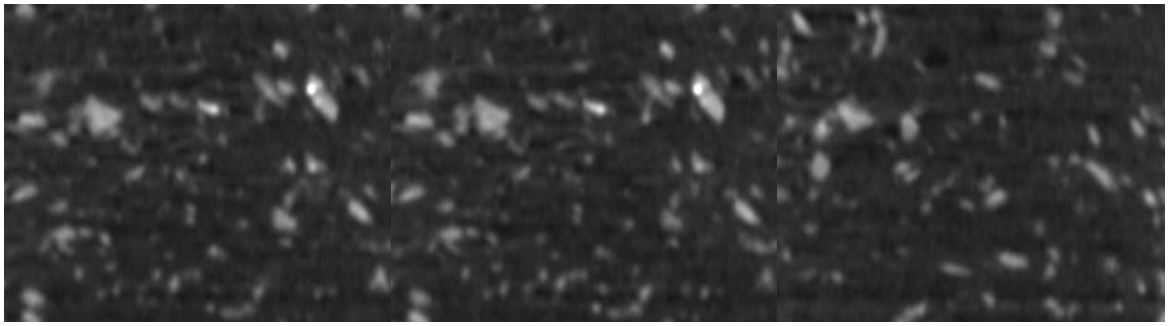

Figure 5-7 20% filler mastic after fatigue test-specimen #5

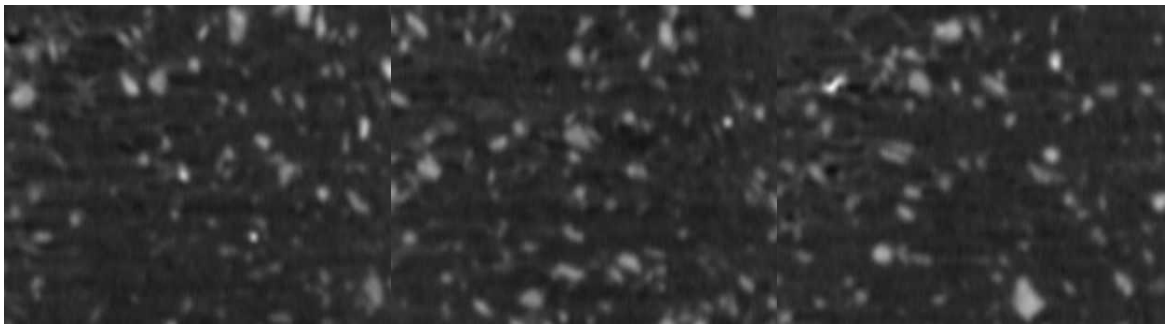

Figure 5-8 20% filler mastic after fatigue test-specimen #6

Table 5-1 Standard deviation of the scanned images for 20% filler mastic

Before fatigue test	Mastic sample #1			Mastic sample #2			Mastic sample #3		
	Image #1	Image #2	Image #3	Image #1	Image #2	Image #3	Image #1	Image #2	Image #3
Standard deviation	18.3	18.9	18.8	19.6	19.7	18.8	18.6	18.4	18.7
Average	18.7			19.4			18.5		
After fatigue test	Mastic sample #4			Mastic sample #5			Mastic sample #6		
	Image #1	Image #2	Image #3	Image #1	Image #2	Image #3	Image #1	Image #2	Image #3
Standard deviation	20.5	21.7	22.3	20.3	22.9	22.4	22.2	19.9	20.4
Average	21.5			21.9			20.8		

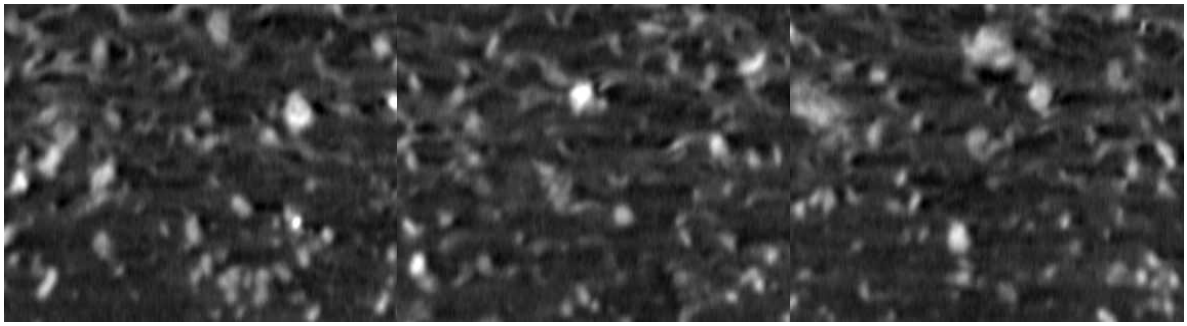

Figure 5-9 30% filler mastic before fatigue test-specimen #1

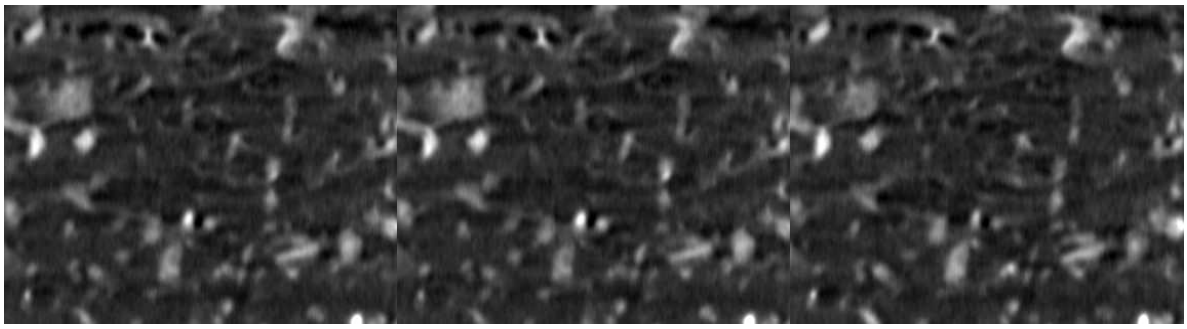

Figure 5-10 30% filler mastic before fatigue test-specimen #2

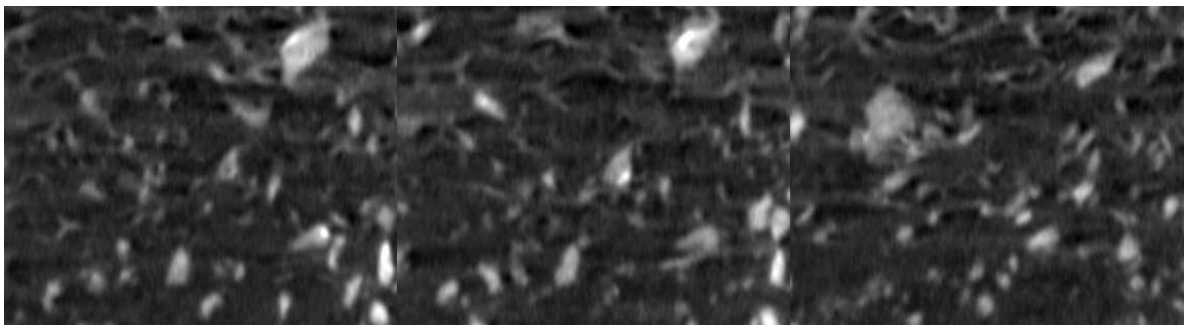

Figure 5-11 30% filler mastic before fatigue test-specimen #3

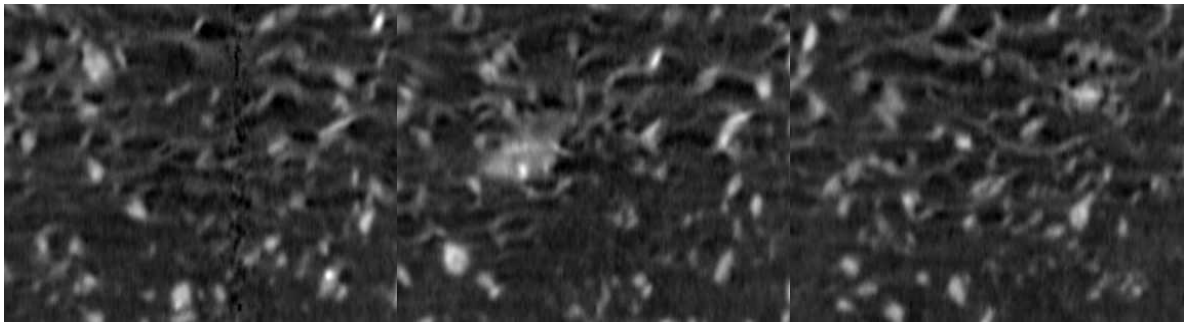

Figure 5-12 30% filler mastic after fatigue test-specimen #4

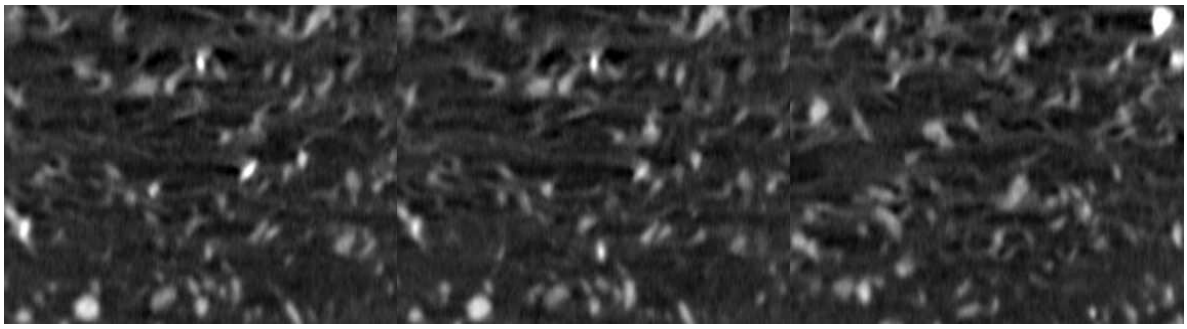

Figure 5-13 30% filler mastic after fatigue test-specimen #5

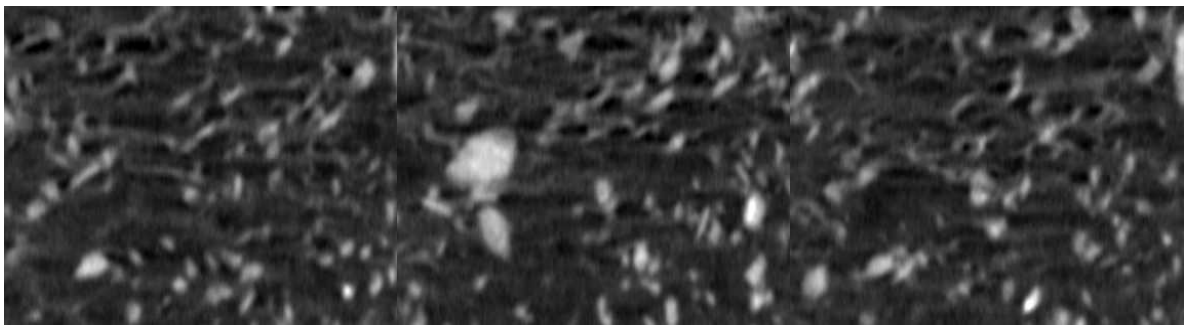

Figure 5-14 30% filler mastic after fatigue test-specimen #6

Table 5-2 Standard deviation of the scanned images for 30% filler mastic

Before fatigue test	Mastic sample #1			Mastic sample #2			Mastic sample #3		
	Image #1	Image #2	Image #3	Image #1	Image #2	Image #3	Image #1	Image #2	Image #3
Standard deviation	27.6	25.9	27.1	27.9	28.9	27.5	27.5	27.4	28.1
Average	26.9			28.2			27.7		
After fatigue test	Mastic sample #4			Mastic sample #5			Mastic sample #6		
	Image #1	Image #2	Image #3	Image #1	Image #2	Image #3	Image #1	Image #2	Image #3
Standard deviation	29.1	29.1	29.3	36.4	29.5	32.3	31.2	29.9	30.0
Average	29.1			32.8			30.4		

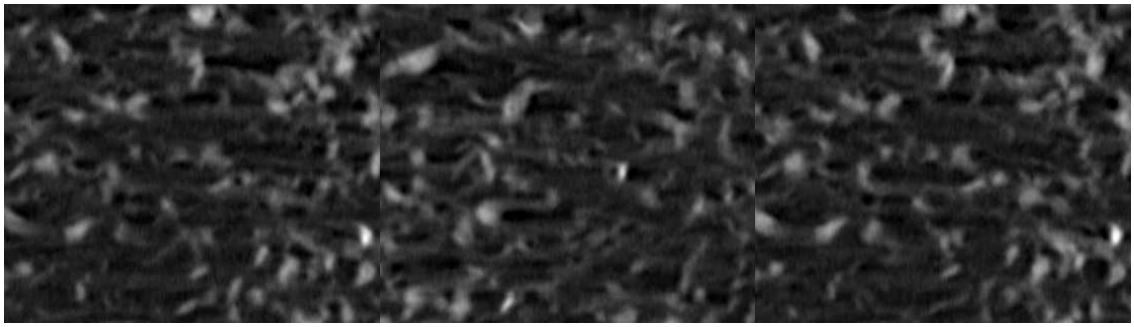

Figure 5-15 40% filler mastic before fatigue test-specimen #1

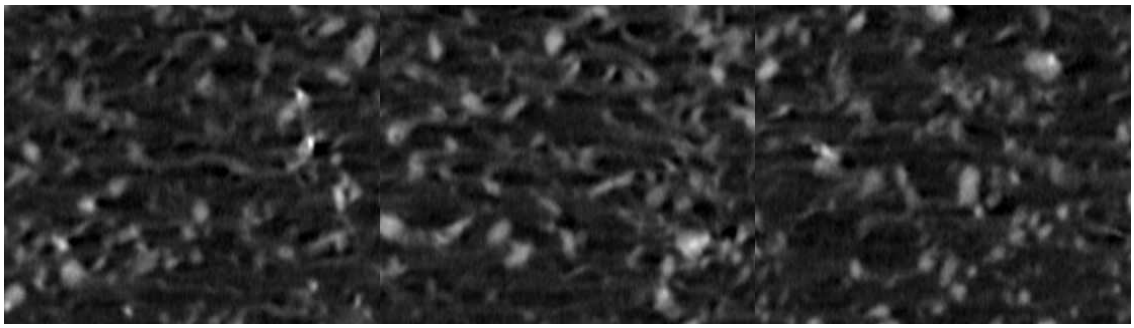

Figure 5-16 40% filler mastic before fatigue test-specimen #2

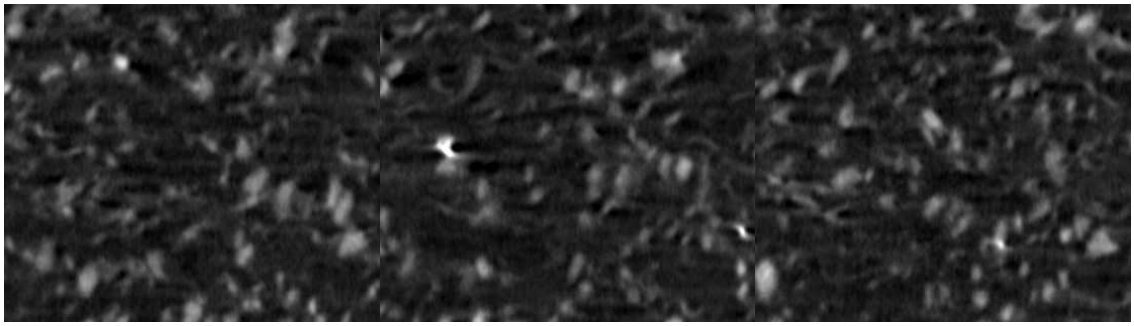

Figure 5-17 40% filler mastic before fatigue test-specimen #3

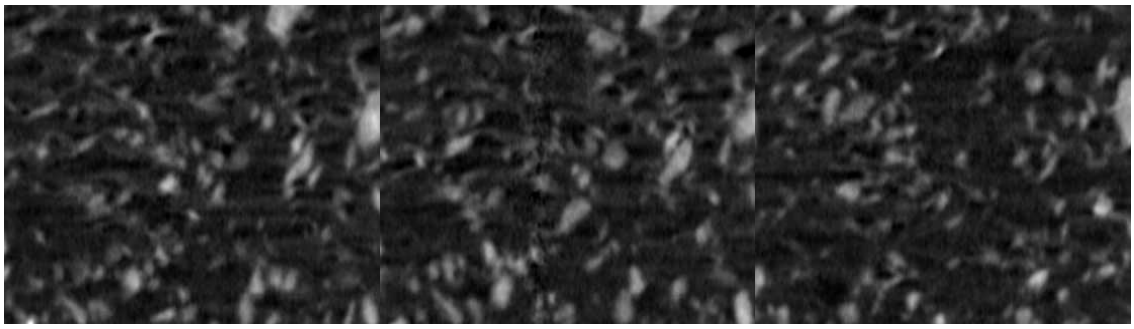

Figure 5-18 40% filler mastic after fatigue test-specimen #4

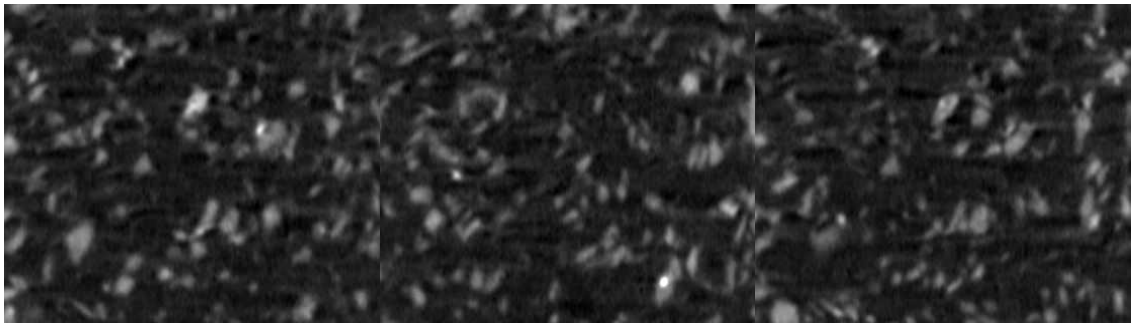

Figure 5-19 40% filler mastic after fatigue test-specimen #5

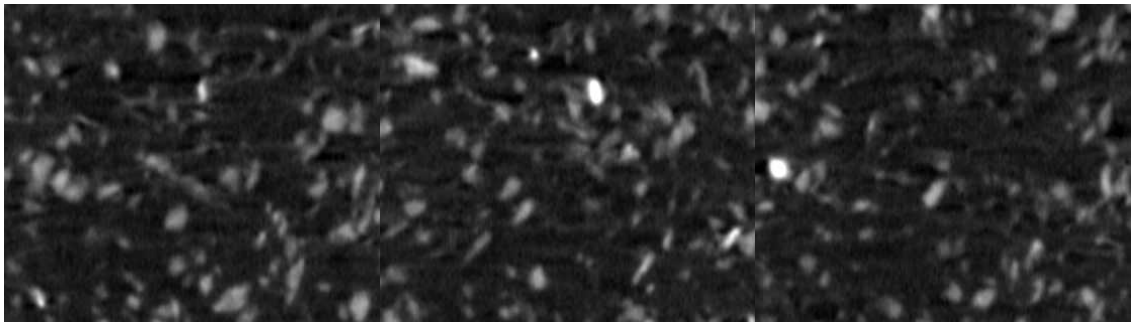

Figure 5-20 40% filler mastic after fatigue test-specimen #6

Table 5-3 Standard deviation of the scanned images for 40% filler mastic

Before fatigue test	Mastic sample #1			Mastic sample #2			Mastic sample #3		
	Image #1	Image #2	Image #3	Image #1	Image #2	Image #3	Image #1	Image #2	Image #3
Standard deviation	24.7	23.9	24.1	24.1	24.9	24.5	24.9	25.9	25.7
Average	24.2			24.5			25.5		
After fatigue test	Mastic sample #4			Mastic sample #5			Mastic sample #6		
	Image #1	Image #2	Image #3	Image #1	Image #2	Image #3	Image #1	Image #2	Image #3
Standard deviation	25.5	26.1	28.8	28.9	26.3	28.1	26.4	26.4	26.9
Average	26.8			27.8			26.6		

It is found that, for all three kinds of asphalt mastic specimen, the standard deviations of the pixel value are slightly increased after the fatigue test which indicates that the fatigue loading changes the internal structure of the asphalt mastic material. Although, these changes are very difficult to observe but can be detected by the image analysis of internal x-ray scanning. Image analysis and x-ray scanning can be used as tools to detect the structure change of the asphalt materials.

5.2 Air void content analysis of asphalt mastic and mixture

5.2.1 Introduction

Fatigue test results of asphalt mastic and mixture indicate that by adding larger size aggregates into the mastic material, the fatigue resistance is not increased but decreased. Both the final strain and number of loading cycles for asphalt mixture specimens are smaller than the asphalt mastic specimens. To compare the internal structure difference between the asphalt mastic and asphalt mixture specimens, three kinds of specimens are scanned using x-ray tomography respectively: Asphalt mastic with 30% fillers, asphalt mixture with 30% fillers and asphalt mixture without fillers. After the 2D scanned images of each kind of material are obtained, 3D internal structure of the specimen is reconstructed. Research conducted by Harvey and Tsai in 1996 showed that the fatigue life of asphalt mixture was higher when the air content was lower. In this study, the air void content of each kind of specimen is measured by using a same threshold value. Same with the previous scanning of the mastic samples, only a 10mm section of each kind of specimen is cut off and scanned. Three specimens are prepared for each kind of material and scanned. 10 slices of scanned images are use to reconstruct the 3-D model. All the elements belonging to the air void in the reconstructed structure are counted for each kind of material respectively.

5.2.2 Results and discussion

One typical scanned image and the reconstructed 3-D structure of each kind of specimen are shown in the Figure 5-21, Figure 5-22, and Figure 5-23 below. The counted air void elements for each reconstructed structure are listed in the Table 5-4, Table 5-5, and Table 5-6 followed.

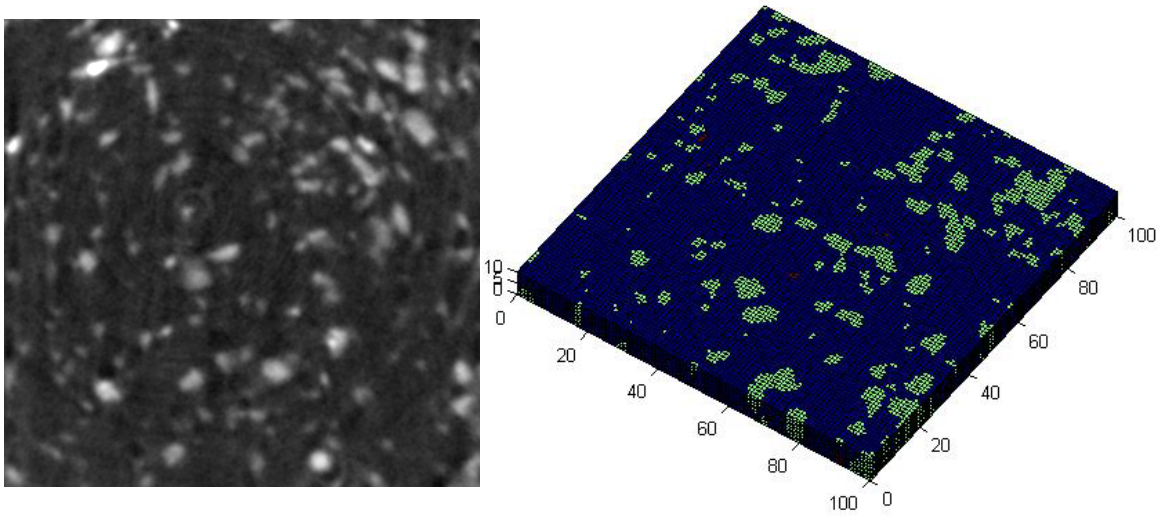

Figure 5-21 Reconstruction of 30% filler mastic specimen #1

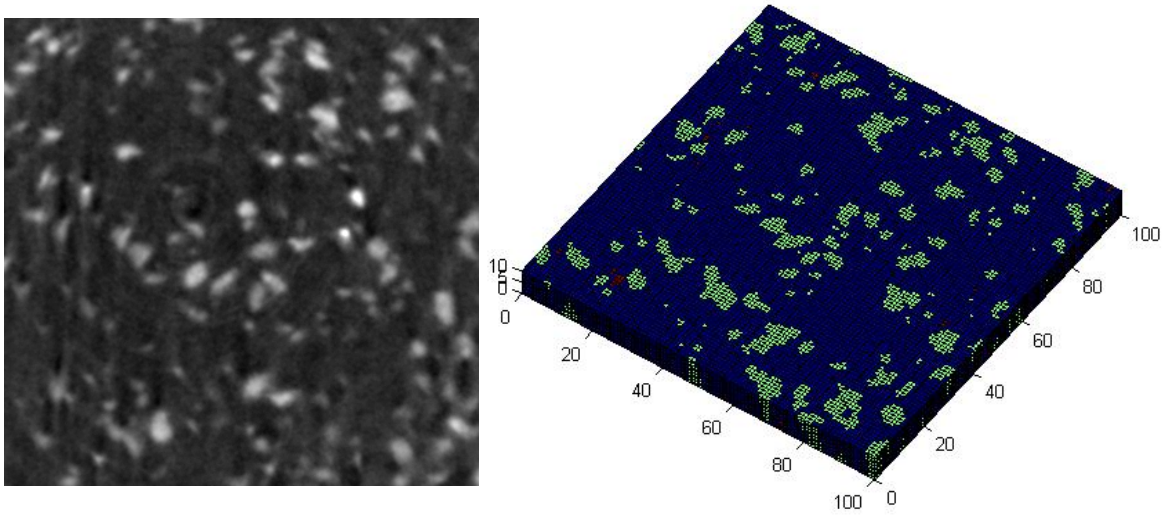

Figure 5-22 Reconstruction of 30% filler mastic specimen #2

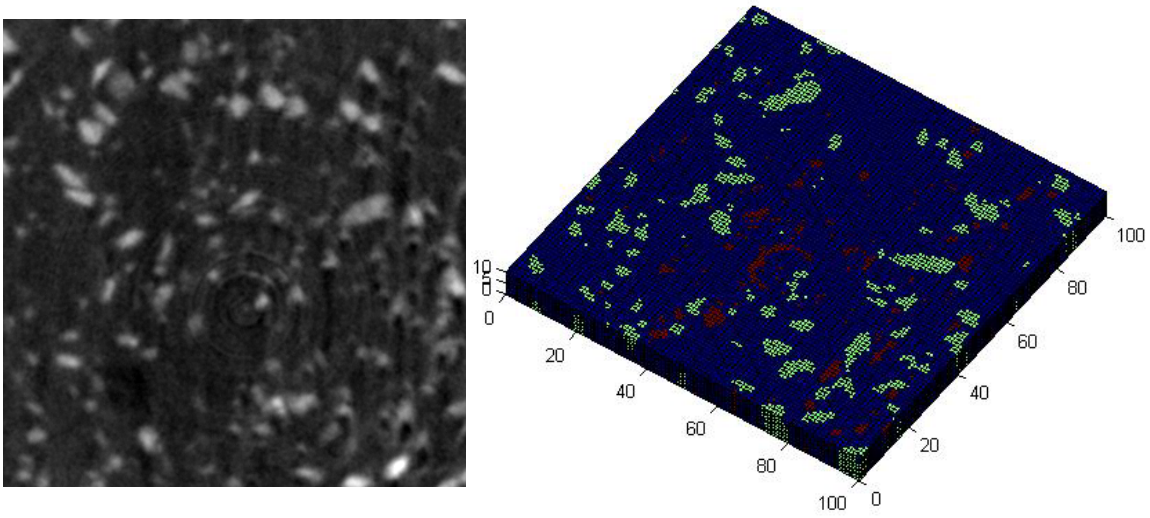

Figure 5-23 Reconstruction of 30% filler mastic specimen #3

Table 5-4 Air void content of 30% filler mastic sample

	30% Mastic #1	30% Mastic #2	30% Mastic #3
Number of air void elements	2760	3200	3360
Number of total elements	100000	100000	100000
Air void ratio	2.76%	3.2%	3.6%
Average	3.18 %		

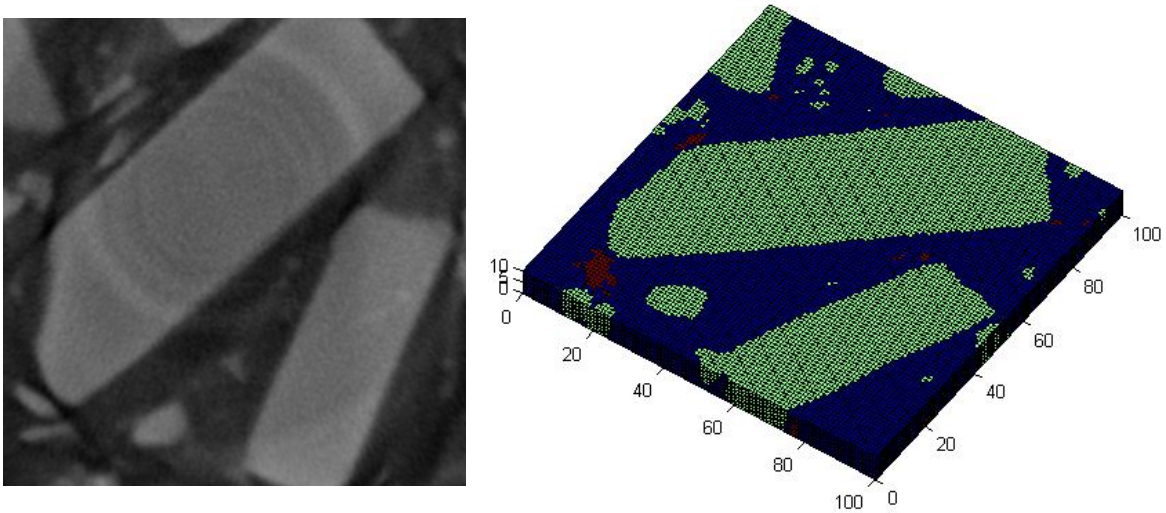

Figure 5-24 Reconstruction of asphalt mixture specimen without filler #1

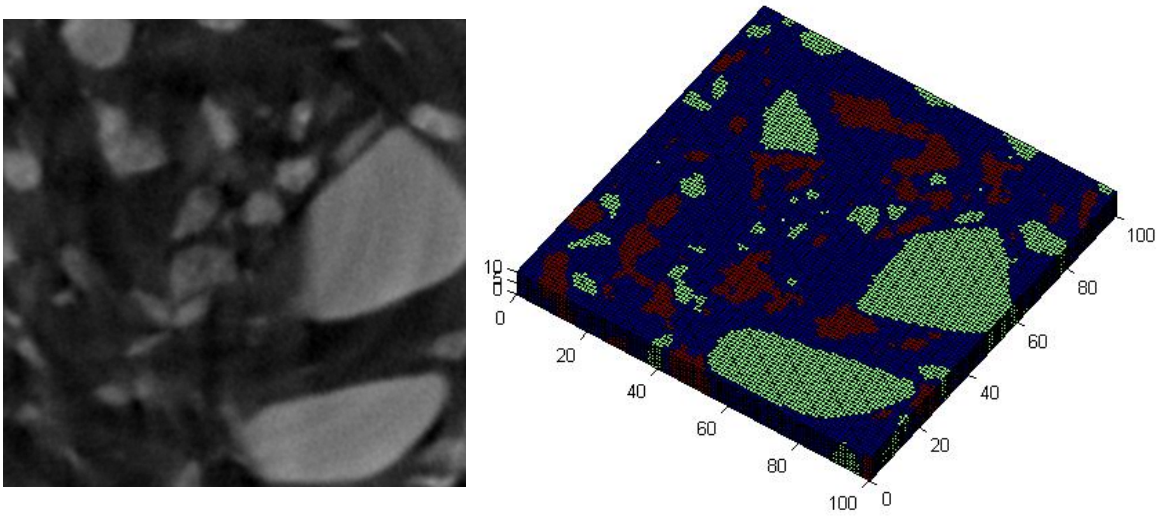

Figure 5-25 Reconstruction of asphalt mixture specimen without filler #2

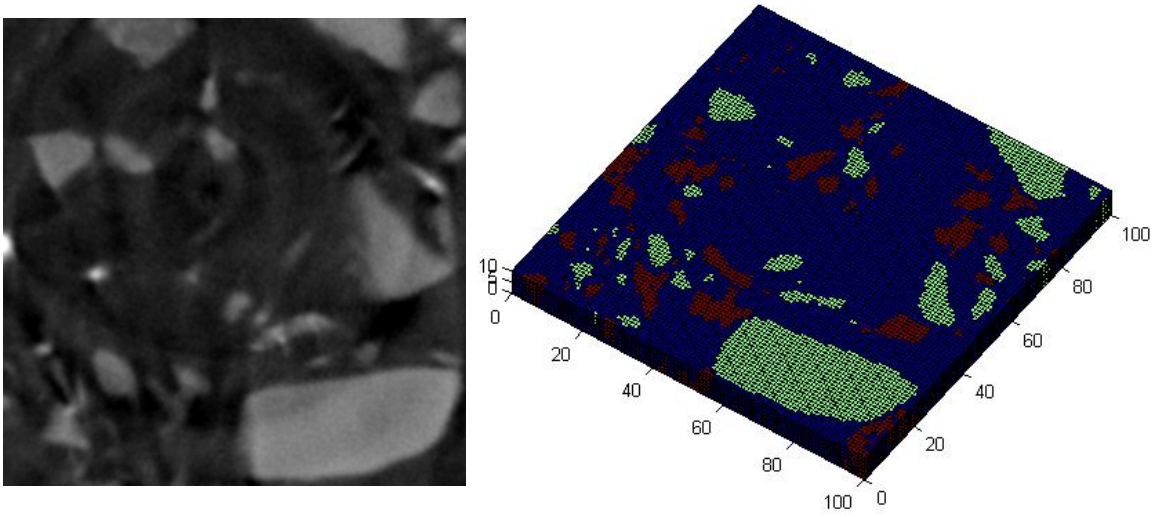

Figure 5-26 Reconstruction of asphalt mixture specimen without filler #3

Table 5-5 Void content of asphalt mixture specimen without filler

	Mixture with no filler #1	Mixture with no filler #2	Mixture with no filler #3
Air void element	8320	12975	11961
Total element	100000	100000	100000
Air void ratio	8.32%	12.975%	11.961%
Average	11.085 %		

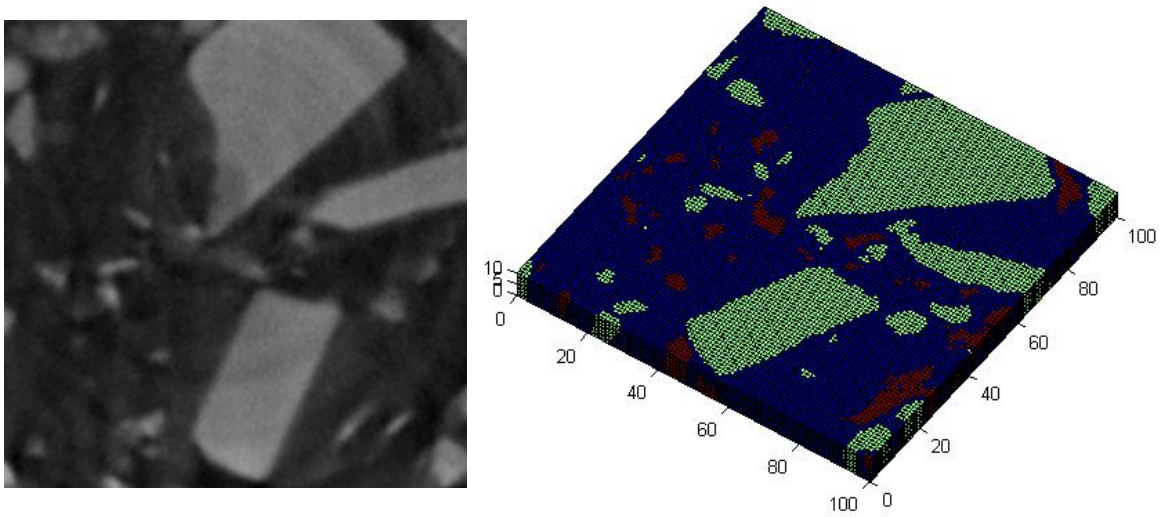

Figure 5-27 Reconstruction of mixture containing 30% filler specimen #1

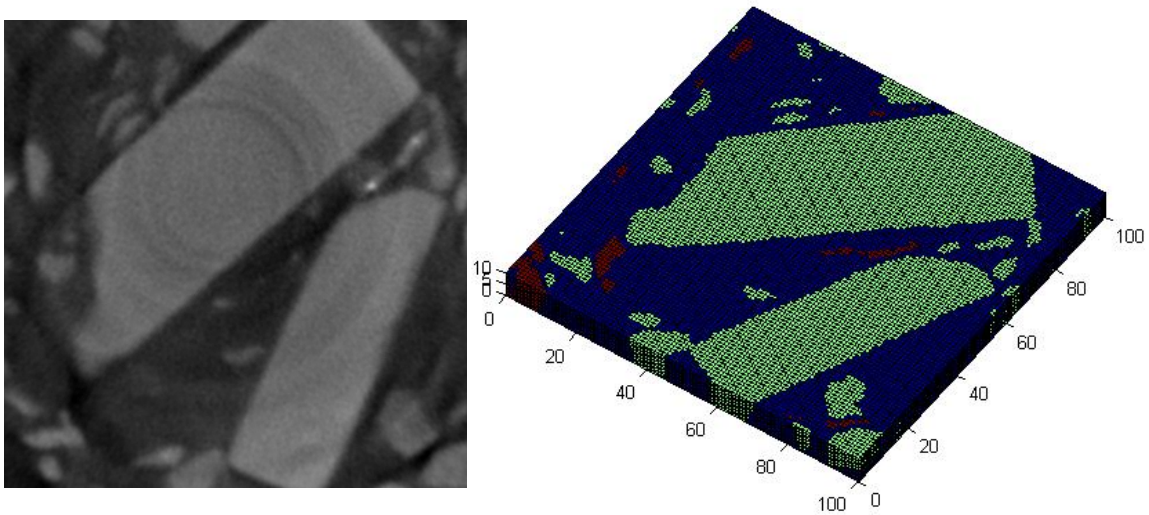

Figure 5-28 Reconstruction of mixture specimen containing 30% filler specimen #2

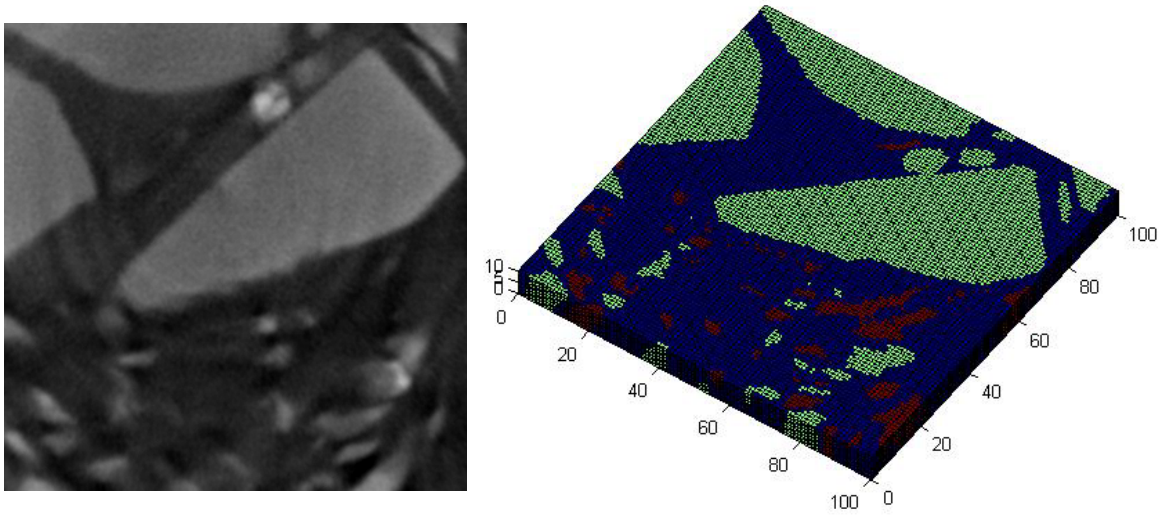

Figure 5-29 Reconstruction of mixture specimen containing 30% filler specimen #3

Table 5-6 Air void content of asphalt mixture specimen containing 30% filler

	Mixture with 30% filler #1	Mixture with 30% filler #2	Mixture with 30% filler #3
Air void element	4668	4449	5127
Total element	100000	100000	100000
Air void ratio	4.668%	4.449%	5.127%
Average	4.748%		

Air void content analysis of three kinds of specimens above shows asphalt mixture containing no filler has highest air void content and asphalt mastic has lowest air void content among three kinds of materials. Considering the fatigue test results of three kinds of material, the air void content is an important factor to affect the fatigue resistance of the material. The asphalt mastic specimen, with lowest air void content among three kinds of materials, reaches the highest final strain and largest number of loading cycles. When the large size aggregates are added, the air void content is increased and causes the decrease of the fatigue resistance. If the large size aggregates are added into the asphalt binder without any filler, the air void is much higher which decreases the fatigue resistance of the material to a larger extent. Since the air voids can be considered as a major source of the initial cracks, larger air voids makes the material more

vulnerable to the cyclic loading, which agrees with the fatigue test results shown in the previous chapter 4.

Chapter 6. Fatigue analysis using finite element method

6.1 Simple model of composite elastic material

The fatigue test results of asphalt mixture show that when the large size aggregates are added into the asphalt binder, the specimen is easy to fail under cyclic loading. To estimate the effect of the large size aggregate added into the asphalt binder, a direct tensile loading is applied on a model containing two kinds of element with different elastic modulus. Three models are described below. In the first model, one kind of element is used to model the binder only. In the second model, a regular shaped aggregate added in the binder medium with higher elastic modulus. In the third model, multiple aggregates are added in the binder medium. The stress and strain analyses of three models are described respectively.

A 10mm by 10mm by 3mm specimen is modeled using 8 nodes brick elastic elements. The elastic modulus of asphalt binder is 5Gpa and Poisson's ratio is 0.35. A 1Mpa tensile loading is applied on the front surface of the model in z direction; the back of the model is fixed in all six degrees of freedom shown in Figure 6-1. The element size of the model is 1mm by 1mm by 1mm. Two node paths are defined shown in the Figure 6-2 and there are 11 nodes on each path. The node ID and the axial stress s33 in z direction of these nodes on the two paths are measured and listed in the Table 6-1. The simulation results agree well with analytical results, the axial stresses of the nodes on both paths are all close to 1Mpa in this simple tension case. The axial strain in the z direction of the nodes along the path 1 and path 2 is plotted in the Figure 6-3. The axial strains of the nodes on the same path are almost same with each other in this simple tension case.

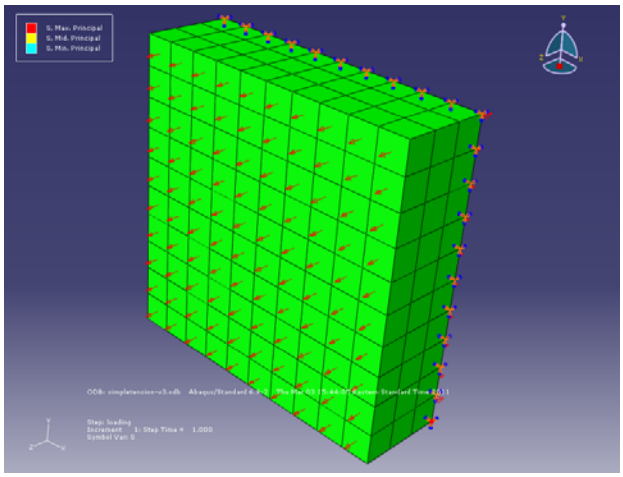

Figure 6-1 Boundary condition of the model

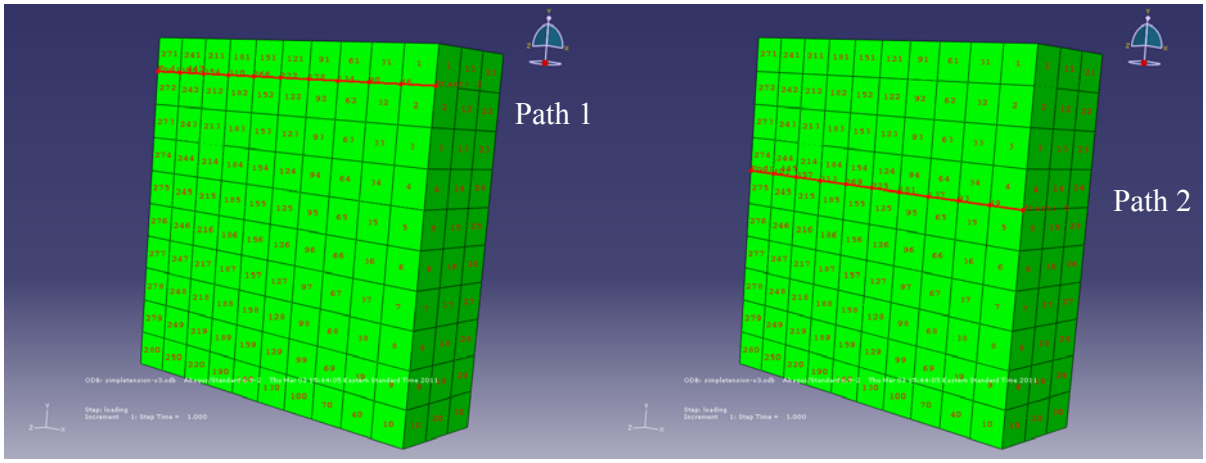

Figure 6-2 Two node paths defined on the model

Table 6-1 Axial stress s33 and strain e33 of two nodal paths

Node Number on path 1(Mpa)	Axial nodal stress s33	Axial strain e33	Node number on path 2(Mpa)	Axial nodal stress s33	Axial strain e33
2	1.002	0.0199	5	0.984	0.0189
46	1.001	0.0200	49	0.987	0.0190
90	1.015	0.0202	93	1.000	0.0190
134	1.001	0.0196	137	0.984	0.0182
178	0.987	0.0190	181	0.970	0.0175
222	1.001	0.0191	225	0.984	0.0176
266	0.987	0.0190	269	0.970	0.0175
310	1.001	0.0196	313	0.984	0.0182
354	1.015	0.0202	357	1.000	0.0190
398	1.001	0.0200	401	0.987	0.0190
442	1.002	0.0199	445	0.984	0.0189

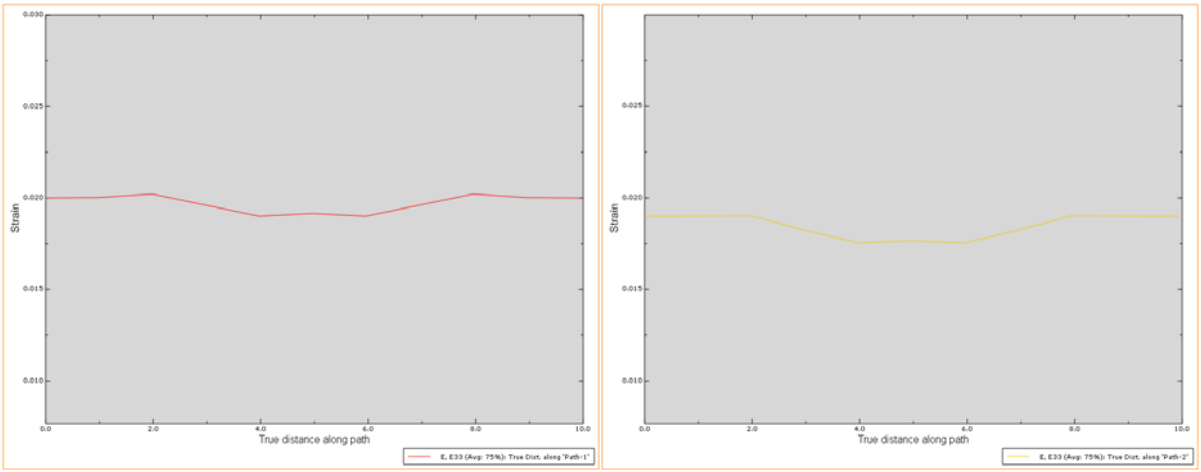

Figure 6-3 Axial strain of the nodes along two paths

In the second model, a composite specimen with same size is generated. Different with the previous one, this model contains two kinds of elastic elements: one with same material properties with the first model to simulate the asphalt binder, the other one with higher elastic modulus 300 Gpa to simulate an aggregate. The poisson's ratio of the aggregate elements is 0.25. The size of this single aggregate is 2mm by 2mm by 3mm thick. Two kinds of element are

shown in different colors in the Figure 6-4: aggregate is yellow and asphalt binder is blue. Same nodes paths are defined as the first model. The axial nodal stresses s33 are measured and listed in the Table 6-2. It can be seen that nodal stresses on path 1 are not affected by the inclusion of the aggregate element. On the path 2, three nodes are shared by both aggregate and binder elements: 181, 225, 269. Two nodal stresses are obtained for each of the three nodes because of the difference of elastic modulus between binder and aggregate element. The contour of axial stress s33 in z direction of the deformed model is shown in Figure 6-5. It can be seen that the axial stress s33 of the aggregate elements, shown as green color in the figure, are about twice larger than binder elements. For those binder elements around the aggregate, shown as dark blue color in the figure, the axial stresses is smaller which are around 0.6Mpa. For those binder elements not surrounding the aggregate, the axial stresses are still close to 1Mpa. The contour of axial strain e33 in z direction of the deformed model is shown in Figure 6-6. The axial strain values along two node paths are plotted in the Figure 6-7. Compared with the first model with only one kind of element, the axial strain along two defined paths of the model with two kinds of elements are different. Due to the introduction of the stiffer elements, the nodes shared by both binder and aggregate elements have smaller strain than those nodes far away from the aggregate elements. Although the node path 1 is further away from the aggregate elements, the nodes closer the aggregate elements are still affected.

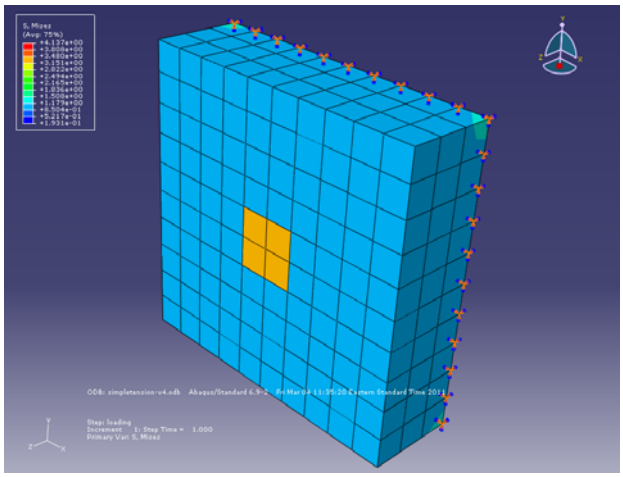

Figure 6-4 Model containing single aggregate

Table 6-2 Axial stress of the nodes on two node paths

Node Number on path 1(Mpa)	Axial nodal stress s33	Axial nodal strain e33	Node Number on path 1(Mpa)	Axial nodal stress s33	Axial nodal strain e33
2	1.00	0.0199	5	0.99	0.0189
46	1.00	0.0199	49	0.98	0.0186
90	1.02	0.0200	93	1.00	0.0187
134	1.00	0.0194	137	0.85	0.0166
178	0.99	0.0186	181	0.62	0.0137
222	0.99	0.0187	181	1.95	0.00008
266	0.98	0.0186	225	0.54	0.0127
310	1.00	0.0194	225	1.95	0.00008
354	1.02	0.0200	269	0.62	0.0137
398	1.00	0.0199	269	1.95	0.00008
442	1.00	0.0199	313	0.85	0.0166
			357	1.00	0.0187
			401	0.98	0.0186
			445	0.99	0.0189

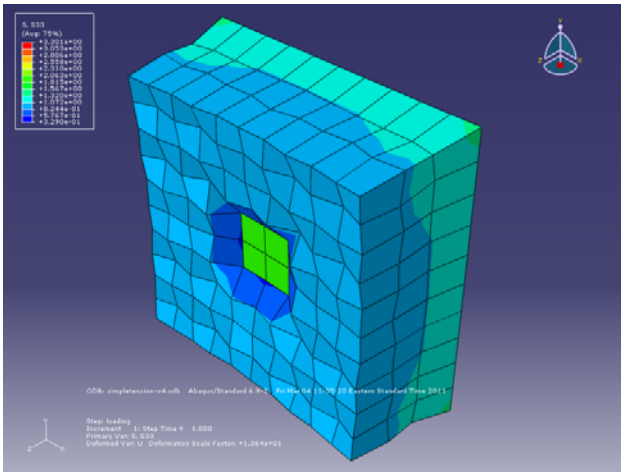

Figure 6-5 Contour of axial stress s33 of deformed model

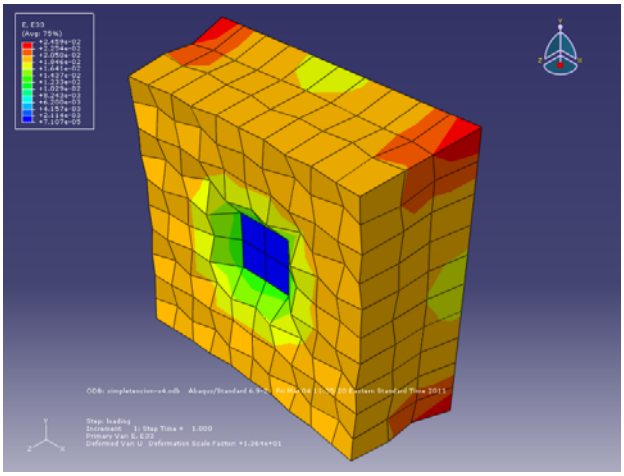

Figure 6-6 Contour of axial strain e33 of deformed model

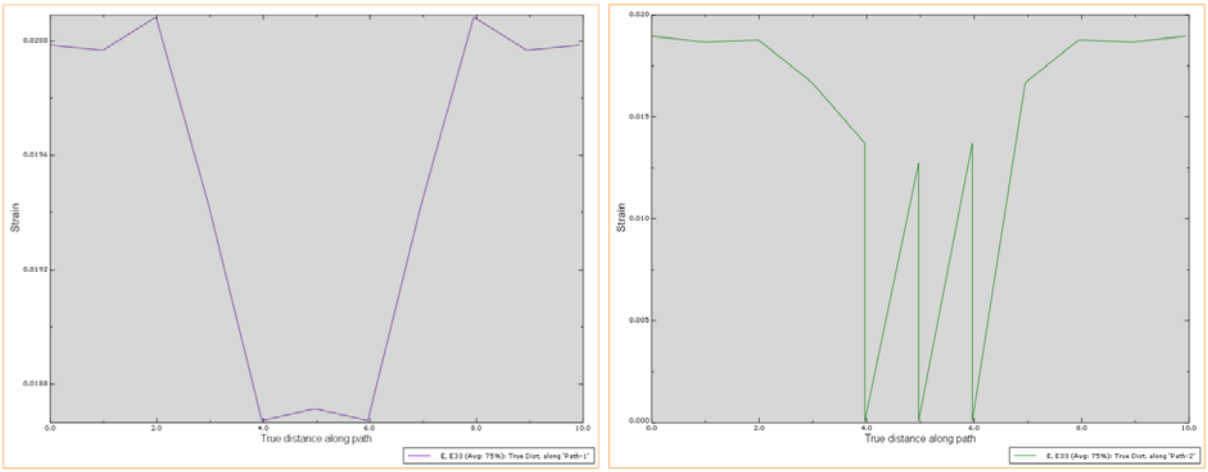

Figure 6-7 Axial strain of the nodes along the two node paths

In the third model, two more aggregates with same sizes as the second model are added. The position and ID of the aggregates are shown on the contour of axial stress of deformed model in Figure 6-8. The simulation results show that, similar with the second model, larger axial stresses are produced on the aggregate elements, while the axial stresses on the binder elements surrounding the aggregates are smaller than 1Mpa. Especially, for those elements between aggregate #2 and aggregate #3, all the nodes are shared with the aggregate elements. The axial stresses of the integration points of these elements are very small. And the axial strain of the aggregate elements is also very small due to the high stiffness of the aggregate element shown in the Figure 6-9.

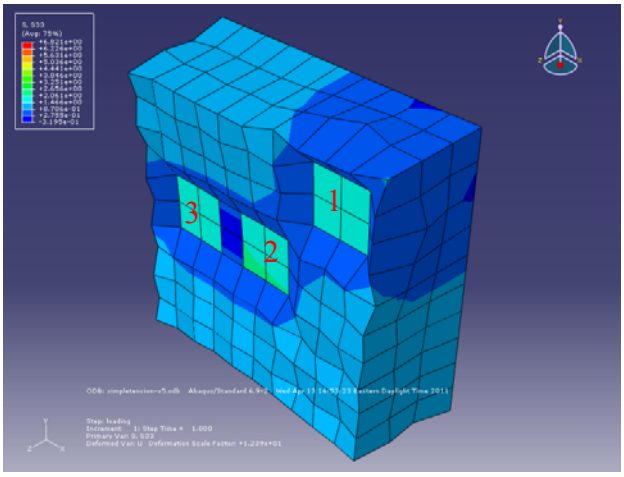

Figure 6-8 Contour of axial stress s33 of deformed model

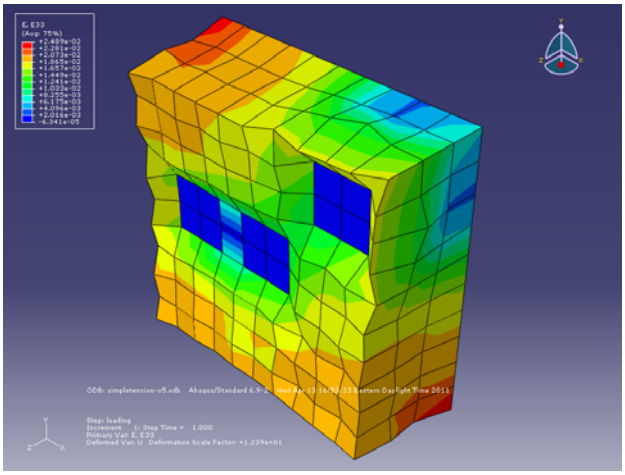

Figure 6-9 Contour of axial strain e33 of deformed model

In the fourth model, the mesh of the concrete block is refined. The element size is 0.5mm by 0.5mm by 0.5mm. Single aggregate is added same with the second model. The size of the aggregate is still 2mm wide by 2mm long by 3mm thick. The contour of axial stress s33 of the deformed model is shown in Figure 6-10. It is similar with second model that the axial stresses generated on the elements surrounding the aggregate are smaller than 1 Mpa. Axial stresses are majorly distributed on the aggregate elements. The axial stresses of all the other binder elements

not surrounding the aggregate is close to the analytical result, 1Mpa. The contour of axial strain e33 of the deformed model is shown in Figure 6-11. The axial strain of the aggregate elements is much smaller than the binder elements. The simulation results of the refined model agree with the previous model.

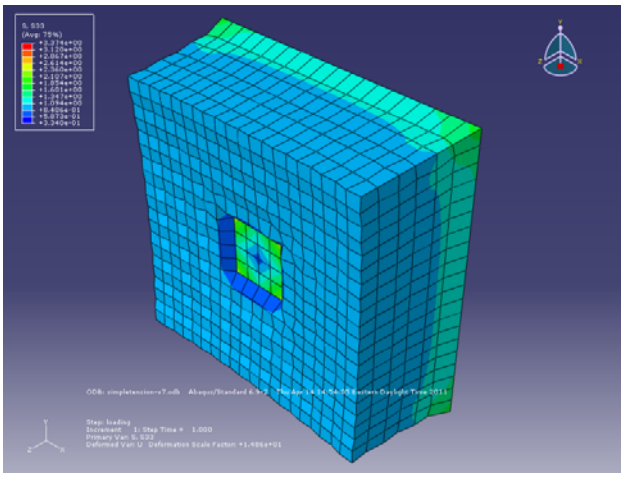

Figure 6-10 Contour of axial stress s33 of the deformed model

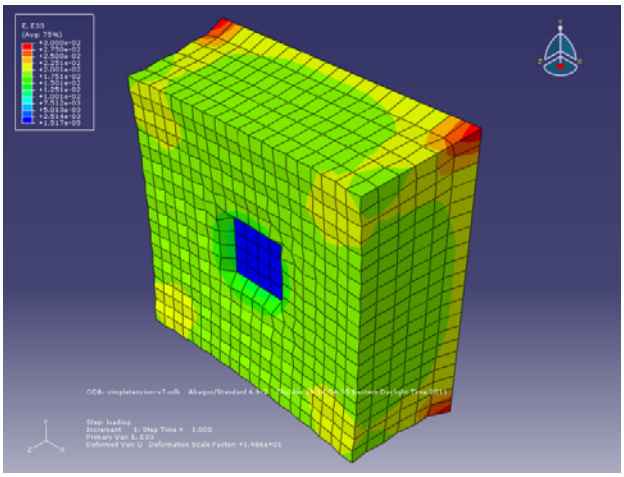

Figure 6-11 Contour of axial strain e33 of the deformed model

In the fifth model, the mesh size is same with the previous model but the aggregate is changed to 1.2mm by 1.2mm by 1.2mm cubic-shape aggregate which is embedded in the center of the model. The contour of the axial stresses s33 of the model is shown in the Figure 6-12. The contour of the axial stresses s33 of the model is shown in the Figure 6-13. It is shown that due to the existence of the high stiffness elements, larger axial stress is concentrated on the aggregate elements and axial stresses on the surrounding binder elements are smaller. For those elements not connecting with the aggregate, the axial stresses are not affected significantly. The axial strain of the center part of the model is smaller than the surrounding elements because of the existence of the aggregate elements.

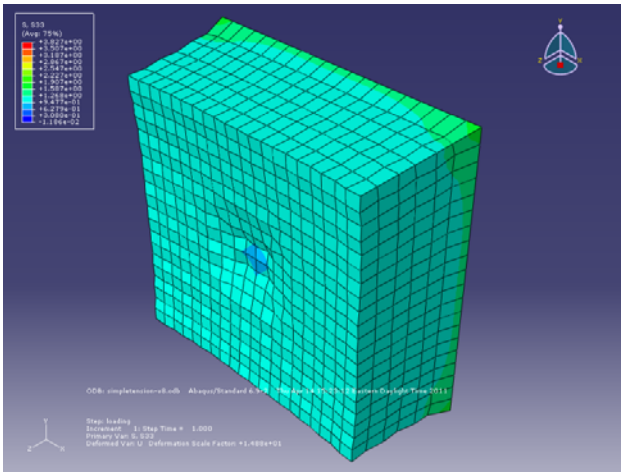

Figure 6-12 Contour of the axial stress s33 of deformed model

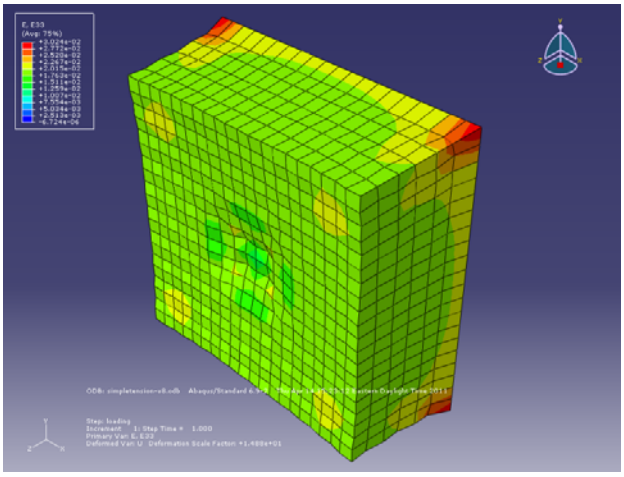

Figure 6-13 Contour of axial strain e33 of deformed model

All the models above show that, when two kinds of model are contained in a continuum model, the axial stress and strain of the element away from the stiffer elements are not significantly affected. The axial stress generated on the softer element surrounding the stiffer aggregate is smaller than axial stress generated on the stiffer element. And, due to the stiffness difference of two kinds of element, the axial strain is very different. The axial strain of the soft element is much larger than the stiffer elements.

6.2 Determination of parameters for fatigue modeling

The developed fatigue test for binder and mastics is modeled using a Finite Element Method (FEM) with an elasto-plastic model. Asphalt binder and aggregate of asphalt mixture are modeled using different constitutive models. The aggregates and fillers are modeled as linear elastic. The asphalt binder is modeled as elasto-plastic. In the mesh generation of asphalt mastic and mixture specimens, 2D x-ray scanned images are used to reconstruct the 3D internal structure. The elements belonging to different components are identified and assigned different

material properties. An assumption is made that fatigue damage only happens in asphalt binder but not in aggregates and fillers. The hardening behavior of the asphalt binder at low temperature is described using a combined isotropic/kinematic hardening model developed by Lemaitre and Chaboche in 1990. The model consists of two components: a nonlinear kinematic hardening component, which describes the translation of the yield surface in stress space through the backstress; and an isotropic hardening component, which describes the change of the equivalent stress defining the size of the yield surface as a function of plastic deformation. The elastic modulus of the asphalt binder is measured using direct tension test at a desired temperature. The parameters of the kinematic and isotropic hardening model are determined using the first half cycle data of the unidirectional tension test for asphalt binder. To address the fatigue damage caused by cyclic loading, the stiffness of the asphalt binder decreases during the fatigue process, which is described by a damage model proposed by Darveaux in 2000. The parameter analysis of the model is conducted and calibrated by comparing the fatigue simulation results and fatigue test results. To avoid the extremely high computational cost during the fatigue simulation, direct cyclic analysis is used to obtain the response of the structure after a large number of loadings.

6.2.1 Elastic modulus of asphalt binder, aggregate and filler

Asphalt binder is considered as elasto-plastic material. The elastic modulus and initial yielding stress are determined by the first half cycle data of the fatigue test for asphalt binder. For the designed fatigue test, the first half cycle is a unidirectional tension process. A typical stress-strain data is shown in Figure 6-14. At the elastic period, the stress increases linearly as the strain develops. After the plastic deformation starts, the relationship between stress and strain becomes nonlinear. The elastic modulus of the asphalt binder is determined by calculating the slope of the

regression line of the linear part. The initial yielding stress is the point where the plastic deformation starts and stress-strain curve becomes nonlinear. As described in the chapter 4, three asphalt binder specimens are tested at -20^{o}C. The elastic modulus and initial yielding stress of each specimen are calculated and listed in the Table 6-3. The Poisson's ratio of asphalt binder used in this study is 0.35.

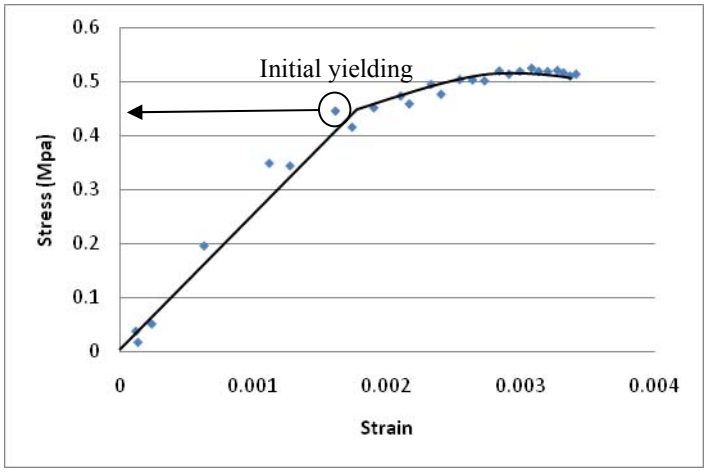

Figure 6-14 Stress strain data of first half cycle of the fatigue test for asphalt binder

Table 6-3 Elastic modulus and initial yielding stress of asphalt binder

	Binder #1	Binder #2	Binder #3
Elastic modulus (Mpa)	262.49	274.52	268.57
Initial yielding stress (Mpa)	0.47	0.44	0.43
Average elastic modulus(Mpa)	268.5		
Average initial yielding stress(Mpa)	0.45		

Both limestone aggregates and quartz fillers are considered as linear elastic materials in the simulation. The elastic modulus of two materials is assumed to be same which is 50Gpa. The Poisson's ratio is 0.25.

6.2.2 Isotropic hardening component of the model for asphalt binder

As described in the chapter 2, the plastic behavior of the asphalt binder is described by a combined isotropic/kinematic hardening model. The parameters of isotropic hardening component and kinematic hardening component are determined respectively.

The isotropic hardening component describes the change of the size of the yielding surface as function of equivalent plastic strain. It can be simply described by an exponential law shown in Equation 6-1.

$$\sigma^0 = \sigma\big|_0 + Q_\infty(1 - e^{-b\bar{\varepsilon}^{pl}}) \tag{6-1}$$

where σ^0 is the size of the yield surface, $\sigma\big|_0$ is the yield stress at zero plastic strain, Q_∞ is the maximum change in the size of the yield surface and *b* is the rate at which the size of the yield surface changes as plastic straining develops. $\sigma\big|_0$ Q_∞ and *b* are three paramters need to be determined by the fatigue test data.

$\sigma\big|_0$ is the initial yielding stress which is already determined by the first half cycle data of unidirectional tension test for asphalt binder. Three binder specimens are tested and the average initial yielding stress is listed in the Table 6-2, which is 0.45 Mpa.

The maximum change in the size of the yield surface, Q_∞, is assumed to be same with the initial yielding stress $\sigma\big|_0$, which is also 0.45Mpa.

In this uniaxial tesile fatigue test, the specimen is stretched along the loading direction, so the equivalent plastic strain $\bar{\varepsilon}^{pl}$ is equal to the palstic strain ε^{pl}. In the Figure 6-9, every point after the initial yielding experience both elastic and plastic strain. The plastic strain part is calculated using Equation 6-2.

$$\varepsilon_i^{pl} = \varepsilon_i - \frac{\sigma_i}{E} \tag{6-2}$$

where ε_i^{pl} is the plastic strain, ε_i is the measured total strain, σ_i is the measured total stress and the E is the ealstic modulus which is 268.5 Mpa for asphalt binder in this study. The ratio of σ_i and E is elastic strain part. It is assumed that the very next point after initial yielding is on the yield surface so the stress value of the point is σ^0 .With known σ^0 $\sigma|_0$ Q_∞ and plastic strain ε_i^{pl}, the parameters *b* can be calculated using Equation 6-3. The data points after the initial yielding for three asphalt binder specimens are shown in the Table 6-3 repectively. The corresponding elastic strain and plastic strain are calculated for each point. The pramater *b* and its average value are calculated. The average value of parameter *b* is 70.

$$b = -\frac{\ln(1 - \frac{\sigma^0 - \sigma|_0}{Q_\infty})}{\bar{\varepsilon}^{pl}} \tag{6-3}$$

Table 6-4 Parameter *b* of the isotrpic hardeing model

Total stress	Total strain	Elastic strain	Plastic strain	b
0.4864	0.002236	0.001811	0.0004242	87.83
0.4528	0.001905	0.001686	0.0002186	28.43
0.4406	0.001896	0.001641	0.0002547	94.22

6.2.3 Kinematic hardening component of the model for asphalt binder

The kinematic hardening component describes the translation of the yield surface in stress space through the backstress α. The evolution law of the backstress is shown in Equation 6-4 and 6-5.

$$\dot{\alpha} = C\dot{\bar{\varepsilon}}^{pl}\frac{1}{\sigma^0}(\sigma - \alpha) - \gamma\alpha\dot{\bar{\varepsilon}}^{pl} \tag{6-4}$$

where C is the initial kinematic hardening modulus. $\dot{\bar{\varepsilon}}^{pl}$ is the equivalent plastic strain. σ^0 is the size of the yielding surface defined in the isotropic hardeing component. γ is the parameter which determines the rate at which the kinematic hardening modulus decrease with increasing plastic deformation. C and γ need to be determined to define the evolution of the backstress α.

The first half cycle data of the fatigue test are used calibrate C and γ. An example of data points after initial yielding is shown in Figure 6-15. For each data point ($\sigma_{i,}\varepsilon_i$), a value of α_i is obtained as

$$\alpha_i = \sigma_i - \sigma_i^0 \tag{6-5}$$

where σ_i^0 is the size of the yield surface at the corresponding plastic strain for the isotropic hardening component. Integration of the backstress evolution law over a half cycle yields the expression:

$$\alpha = \frac{C}{\gamma}(1 - e^{-\gamma\varepsilon^{pl}}) \tag{6-6}$$

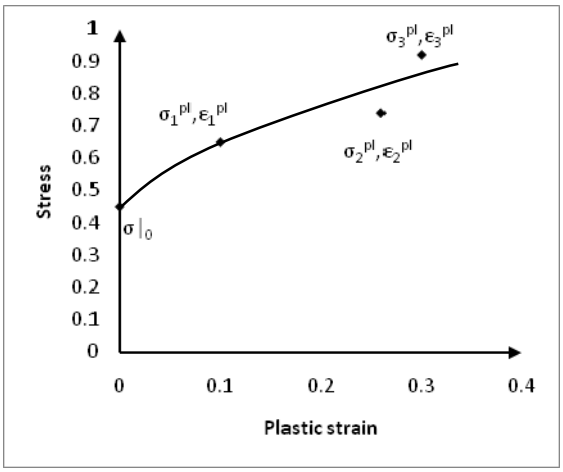

Figure 6-15 First half cycle of unidirectional tension test

As described before, the first half cycle of the fatigue test is a unidirectional tension process, the equivalent plastic strain equals to the plastic strain which can be calculated based on Equation 6-2. With known α_i and corresponding $\bar{\varepsilon}^{pl}$, the C and γ can be determined. The very first point after initial yielding and the end point of the half cycle are used to calculate C and γ. The stress and corresponding plastic strain used to calibrate C and γ are listed in the Table 6-5.

Table 6-5 Plastic strain of the first half cycle of the fatigue test

Stress	Total Strain	Plastic Strain
0.4528	0.001905	0.000219
0.5151	0.002915	0.000997

6.2.4 Damage model for asphalt binder

Damage of the asphalt binder caused by fatigue loading is described by an energy based damage model proposed by Darveaux in 2000. The model was developed to describe the crack initiation and propagation of joint solder. In this study, this model is utilized to describe the stiffness

decrease of the asphalt binder during the fatigue process. The damage model consists of two: damage initiation and damage evolution.

The damage initiation criterion is a phenomenological model to predict the number of loading cycles when the damage occurs due to stress reversals and the accumulation of inelastic strain. The model is described by

$$N_0 = c_1 \Delta w^{c_2} \tag{6-6}$$

where c_1 and c_2 are material constants determined by the test data. Δw is inelastic hysteresis energy.

Once the damage initiation criterion is satisfied at a material point, the damage evolution is modeled by the rate of the damage in a material point per cycle which is given by

$$\frac{dD}{dN} = \frac{c_3 \Delta w^{c_4}}{L} \tag{6-7}$$

where c_3 and c_4 are material constants, and L is the characteristic length associated with an integration point. D is damage variable which describes the stiffness decrease of the material. The characteristic length L is based on the element geometry and formulation; it is a typical length of a line across an element for a first-order element.

At any given loading cycle during the analysis the stress in the material is given by Equation 6-8

$$\sigma = (1 - D)\bar{\sigma} \tag{6-8}$$

where $\bar{\sigma}$ is the effective stress tensor that there is no damage in the material. The load carrying capacity of the material is lost when $D = 1$.

The crack initiation and propagation of the asphalt binder specimen is very difficult to obtain in this study. The damage parameters used for joint solder materials in Darveaux's work are initially used. $c1$=20000, $c2$=-1.45, $c3$=5, $c4$=1.15. The parameter analysis will be conducted and calibrated by a comparison between the fatigue test results and simulation results.

6.3 Modeling of fatigue process

6.3.1 Fatigue of asphalt binder

An asphalt binder specimen is generated shown in the Figure 6-11. The size of the specimen is 10mm by 10mm by 10 mm. 8 nodes brick element is used for mesh generation. The size of the element is 1mm by 1mm by 1mm. A cyclic tensile stress is applied on the front surface of the model as lab test. The back surface of the model is fixed. The cyclic tensile stress applied on the specimen follows the sinusoidal format shown in the Equation 6-9.

$$T = T_0(A_0 + \sin \omega(t - t_0)) \tag{6-9}$$

where T_0 is the magnitude of the cyclic stress, A_0 is a constant term, ω is the circular frequency, t_0 is the starting time. In the fatigue lab test of asphalt binder, the peak value of the cyclic sinusoidal loading is 20N. The effective cross section area is 36mm^2. The frequency of the sinusoidal loading is 0.5Hz. The parameters shown in the Equation 6-10 are chosen so the cyclic tensile stress of the simulation is same with the loading condition of the lab test.

$$T = 0.28(1+\sin\pi(t-0.5)) \tag{6-10}$$

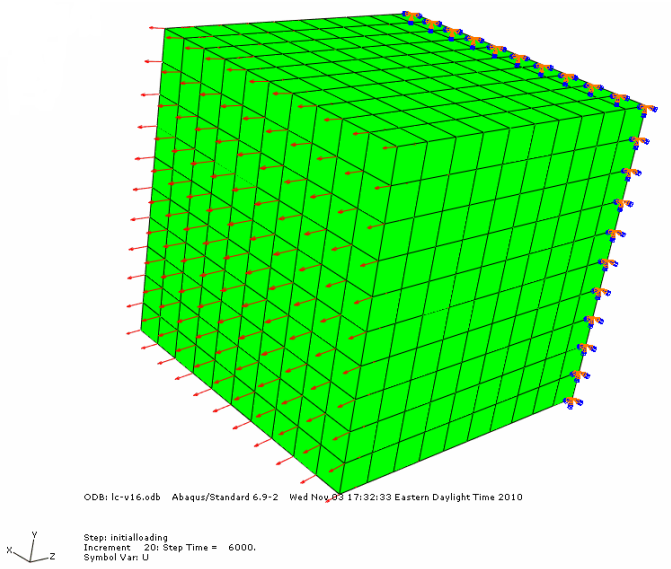

Figure 6-16 Fatigue model of asphalt binder

The previous fatigue test results of asphalt binder show that the average number of loading cycles before a binder specimen fails is 105. In the simulation, 105 loading cycles are applied on the model. The axial displacement of the center node of front surface is measured. The axial strain is calculated. The measured axial strain from lab test and simulation are listed in the Table 6-6.

Table 6-6 Loading number and final axial strain of asphalt binder

	Number of cycles	Axial strain
Simulation	105	0.0069
Lab test	105	0.0059

The convergence of the simulation results is checked by changing the mesh size of the asphalt binder model to 0.2mm by 0.2mm by 0.2mm. The new mesh of the model is shown in Figure 6-17. The simulation results are listed in the Table 6-7, which agree with the previous modeling.

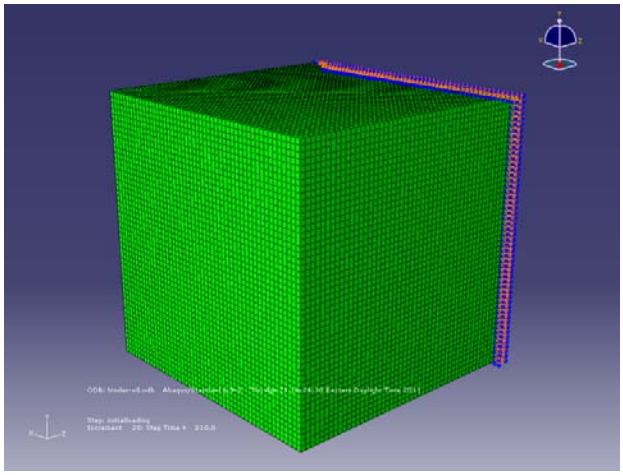

Figure 6-17 Refined mesh of asphalt binder model

Table 6-7 Simulation result of refined asphalt binder model

	Number of cycles	Axial strain
Simulation result	19208	0.0069

6.3.2 Fatigue of asphalt mastic

As introduced before, the fatigue test of asphalt mastic is also simulated. In the first model, the material property of asphalt binder is still used for all the elements. Different from the previous model, 19028 cyclic loading cycles are applied on the specimen, which is the average number of loading cycles before a 30% filler mastic specimen fails measured in the fatigue lab test. The final strain of the loading end is measured. The simulation result is compared with lab test result of mastic and listed in the Table 6-8.

Table 6-8 Loading number and final axial strain of mastic

	Number of loading cycles	Axial strain
Simulation result	19208	0.462
Lab test result	19208	0.0684

Since the filler of the mastic is not considered, the simulation result is much larger than the lab test result. To improve the fatigue model, the fillers of the mastic specimen are considered in the second model. The internal structure of mastic model is based on the 3-D reconstruction of x-ray scanned mastic samples. 10 slices scanned images of mastic specimen containing 30% fillers are used to reconstruct the internal structure of the mastic specimens. The asphalt binder is still considered as elasto-platic material and the fillers are considered as elastic material. The model parameters for the asphalt binder are same with the previous simulation. The elastic modulus of fillers is 50Gpa and the Poisson's ratio is 0.25. It is assumed that no damage happens on the filler materials so the damage properties are assigned to binder materials only. The number of element of the model is controlled by the size of the scanned images. In the first model, the size of the scanned image is 10 by 10, which is same with previous asphalt binder model. 19208 loading cycles are applied on the specimen and the simulation result is listed in the Table 6-9.

Table 6-9 Loading number and final axial strain of mastic modeling

	Number of loading cycles	Axial strain
Simulation	19208	0.0237
Lab test	19208	0.0684

Compared with the first model, the introduction of stiffer elements which are representing the fillers of the mastic material decreases the final strain after fatigue process; the simulation result is much closer to the lab test result.

A parametric analysis of damage model is conducted to improve the fatigue modeling. In the damage model, the parameters $c1$ and $c2$ determines the initiation of the fatigue damage. In the following analysis, the damage parameters $c2$=-1.45, $c3$=5, $c4$=1.15, which are same with first binder model, the parameter $c1$ is changing. The different $c1$ values and its corresponding simulation results are shown in the Table 6-10.

Table 6-10 Simulation results with different $c1$ values

Parameter $c1$	Axial strain
40000	0.00351
30000	0.00351
20000	0.0237
10000	0.0656
1000	0.292

It can be seen that parameter $c1$ defines the number of loading cycle at which the fatigue damage is initiated. Smaller $c1$ indicates early initiation of the fatigue damage so that the stiffness of the binder elements decreases earlier and the final axial strain of the model is larger. Similar with parameter $c1$, the parameter $c2$ also affects the initiation of the fatigue damage. Keep the other parameters constant, the parameter $c2$ is changing. The different $c2$ values and its corresponding simulation results are shown in the Table 6-11.

Table 6-11 Simulation results with different $c2$ values

Parameter $c2$	Axial strain
-10	0.00351
-5	0.00351
-1.45	0.0237
-0.5	0.0793
-0.1	0.252
-0.001	0.252

The analysis above shows that if the parameter $c1$is too large or the parameter $c2$ is too small, the number of loading cycles to initiate the fatigue damage will be so large that there is no fatigue damage happened in the desired number of loading cycles. To address the fatigue effect caused by cyclic loading, appropriate parameters to initiate the fatigue damage need to be used.

The parameter $c3$ and $c4$ determines the damage propagation of the model if the initiation condition is satisfied. In the following analysis, only the parameter $c3$ is changing, the other damage parameters keep constant. Different $c3$ values and its corresponding simulation results are shown in the Table 6-12.

Table 6-12 Simulation results with different parameter *c*3

Parameter *c*3	Axial strain
100	Too large
10	0.0628
5	0.0237
1	0.0093
0.1	0.0015
0.01	0.0015

Similar with parameter $c3$, parameter $c4$ is changing and the different simulation results are listed in the Table 6-13.

Table 6-13 Simulation results with different parameter c4

Parameter *c*4	Axial strain
10	0.0015
5	0.0015
1.15	0.0237
0.5	0.0581
0.1	0.674
0.01	Too large

It can be seen that if the parameter $c3$ is too large or the parameter $c4$ is too small, the axial deformation of the model will be too large and not reasonable. Small parameter $c3$ or large parameter $c4$ will make the damage propagates slowly in certain number of loading cycles so that axial deformation of the model will be small.

Based on the fatigue test results, both the final strain and total number of loading cycles of mastic are much larger than the asphalt binder. Previous simulation shows that if the aggregates are not considered, the final strain of the model will be too large at larger number of loading cycles. After the stiffer aggregates elements are considered, the results are closer to the lab test results. To improve the simulation results, in the fatigue modeling of mastic, appropriate damage parameter $c1$ is chosen and the other damage parameters are used same values as asphalt binder modeling. The parameters used for mastic fatigue modeling and corresponding final axial strain is listed in the Table 6-14.

Table 6-14 Damage parameters used for fatigue simulation of mastic

Number of loading cycles	Parameter $c1$	Parameter $c2$	Parameter $c3$	Parameter $c4$	Axial strain
19208	10000	-1.45	5	1.15	0.0656

When the high resolution scanned images are used, the mesh size of the model becomes smaller and the computation time will also be increased. To analyze the mesh dependency of the model, different meshes are used. The size of the model is still 10mm by 10mm by 10mm. The sizes of the images used to reconstruct the model are 10 by 10, 30 by 30 and 50 by 50. The parameters for the model are same with the previous mastic modeling. With higher resolution images, the size of the mesh to build up model is smaller. The computational cost will be increased. The

models based on images with higher resolution are shown in the Figure 6-18 and Figure 6-19 respectively. The simulation result of refined model and computational time are compared with previous modeling in the Table 6-15. Since high resolution images are used, the number of elements belonging to each component is also changed. The simulation results will be affected and the damage parameters need to be adjusted for different models. In this study, only damage parameter $c1$ is adjusted. The parameter $c1$ used and corresponding simulation results are listed in Table 6-16.

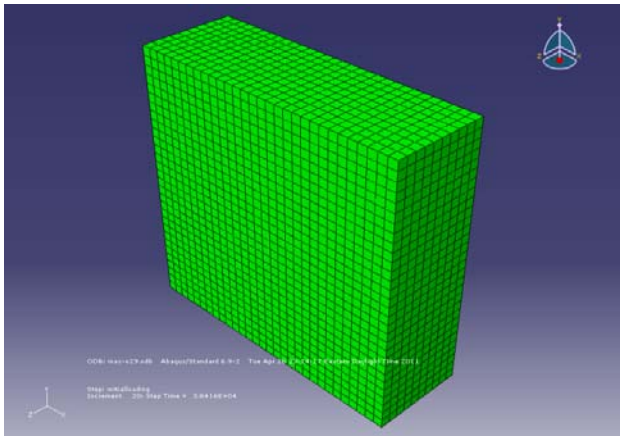

Figure 6-18 Model developed from 30 by 30 images

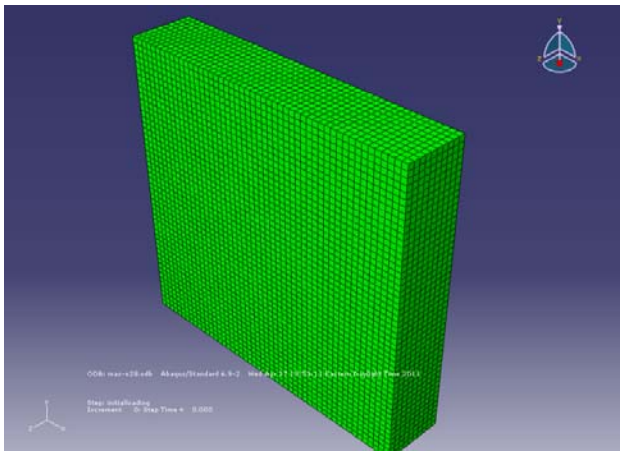

Figure 6-19 Model developed from 50 by 50 images

Table 6-15 Simulation results of models with different mesh size

Image resolution	Element number	Axial strain	Computational Time (seconds)
10x10	1000	0.0656	4500
30x30	9000	0.215	40500
50x50	25000	0.455	259200

Table 6-16 Simulation results of models with different mesh size

Image resolution	Adjusted Parameter $c1$	Axial strain
30x30	14500	0.0592
50x50	17000	0.0614

6.3.3 Fatigue of asphalt mixture

The fatigue simulation of asphalt mixture is similar with mastic specimen, 10 slices scanned images of asphalt mixture specimen with 30% fillers are used to reconstruct the internal structure. However, compared with mastic specimen, the number of aggregate elements in the mixture specimen is larger. Based on the lab test result, the average number of loading cycles before a mixture specimen containing 30% filler fails is 12200. The average final strain of the specimen is 0.0402. Since both final stain and number of loading cycles of a mixture specimen are smaller than the mastic specimen, another damage parameter $c1$ is used. The corresponding simulation result is shown in the Table 6-17.

Table 6-17 Damage parameters used for fatigue simulation of mastic

Number of loading cycles	Parameter $c1$	Parameter $c2$	Parameter $c3$	Parameter $c4$	Axial strain
12200	16500	-1.45	5	1.15	0.0429

It can be seen that the designed fatigue lab test of asphalt binder, mastic and mixture can be simulated based on FEM method. With proper calibration of damage model parameters, the complicated fatigue process of the specimen can be simply modeled. The developed FEM model will be used as an alternative tool to study the fatigue problem of the asphalt binder mastic and mixture at low test temperature and replace the time costly lab fatigue test in the further research under certain conditions.

Chapter 7. Influence of the basalt fiber to the fatigue resistance

7.1 Introduction

The basalt fiber recently captures the interest of research community due to its good performance in terms of strength, temperature range and durability. Due to the low tensile strength and low strain at fracture of plain concrete, fibers are randomly dispersed throughout the concrete mix to increase the concrete ductility and its energy absorption capacity. Ramakrishnan *et al.* (1998) conducted an experimental research to evaluate the performance characteristics of basalt fiber reinforced concrete and basalt bar reinforced concrete. It is reported that the addition of the basalt fiber into the cement concrete causes a noticeable increase in the post crack energy absorption capacity and ductility. And the impact resistance increases as the fiber content is increased. Sim *et al.* (2005) conducted a study to investigate the applicability of the basalt fiber as a strengthening material for structural concrete members by using various experimental methods. The durability, mechanical properties, and flexural strengthening of the basalt fiber used are evaluated. It is found that the basalt fiber keeps about 90% of the normal temperature strength after exposure at 600 ^{o}C for two hours and the basalt fiber strengthening improved both the yielding and the ultimate strength of the concrete beam specimen up to 27% in the flexural strengthening evaluation test. Ludovico *et al.* (2010) used basalt fiber as confinement of cement concrete and compare its effect with other traditional confinement method like uniaxial glass-fiber-reinforced polymer laminates; alkali-resistant fiberglass grids bonded with a cement-based motar; bidirectional basalt laminates preimpregnated with epoxy resin or latex and then bonded with a cement-based motar and cement-based mortar jacket. Their study shows that confinement

based on basalt fiber bonded with a cement-based mortar could be a good method to overcome some limitations of epoxy-based FRP laminates. The reinforcement effect of the basalt fiber to the confinement of concrete is widely discussed in traditional research works. (Brik 1999; Mstthys *et al*. 1999; Spoelstra and Monti 1999; Tepfres 2001). In this study, as an innovative additive, the influence of basalt fibers to the asphalt concrete at low temperature is investigated using direct tension test and developed fatigue test. The basalt fiber, made from extremely fine fibers of basalt, is cut to short sections and added into the pure asphalt binder and asphalt mastic materials to prepare fiber-treated asphalt binder and mastic specimens. The fiber-treated asphalt binder and mastic specimens are tested using direct tension test and fatigue test at low temperature. The test results are compared with test results of asphalt binder. The fiber-treated asphalt binder and mastic specimens are scanned using Xradia microXCT with a resolution of 0.5 um. Based on the scanning images, the fiber-treated asphalt binder and mastic specimens are modeled using FEM. The effect of fiber to the binder and mastic material under tensile and cyclic loadings are analyzed.

The basalt fiber is a high-performance fiber made of basalt rocks which are melted around 1500 ^{o}C and manufactured to fibers. Compared with polyester fiber and lignin fiber, the basalt fiber has higher tensile strength and elastic modulus. (Table7-1). It is also found that the absorption rate of the basalt fiber is high which can avoid the bleeding and raveling problem of the asphalt concrete pavement under high temperature. The basalt fiber retains 95% strength under 600 ^{o}C and very good resistance to the water, acid and alkali damage. The high temperature resistance and good chemical stability make the basalt fiber a very good modifier of asphalt concrete. Moreover, when the fibers are added into the mastic materials, they behave as "bridges" to

connect small fillers and reinforce the structure. The reinforcement effect can avoid stress localization and improve the strength of the pavement.

Table 7-1 Mechanical properties of fibers

Fiber	Tensile strength (Mpa)	Elastic modulus (Gpa)	Elongation rate (%)
Basalt fiber	4100~4840	93.1~110	3.1~3.2
Polyester fiber	650~850	10.0~15.0	7~17
Lignin fiber	560~610	3.5~7.5	10~25

In order to mix with asphalt materials, the basalt fibers are cut to short sections as shown in the Figure 7-1. The diameter of the fiber is 13um and the length is about 4.5mm. These fibers are mixed with heated asphalt binder and mastic during the specimen preparation. It is found that the fluidity of the specimen decreases to a large extent as the content of the basalt fibers added into specimen increases. Since low fluidity of the specimen will cause failure of the specimen preparation. Fiber content added into the asphalt binder and mastic specimen need to be controlled. In this study, the fiber content is 0.5% of the asphalt binder weight for both asphalt binder and mastic specimen. The filler content of the mastic specimen is 30%, which is found the optimum filler content in the previous fatigue study of the mastic specimen at low temperature.

The asphalt used to prepare the binder specimen and mastic specimen is asphalt binder PG 64-22. Both binder and mastic specimens are tested at -20^{o}C using direct tension test and fatigue test. Then the fibers are added into both specimens to prepare fiber-treated asphalt binder and mastic specimens. Direct tension test and fatigue test are conducted again on these materials and the results are compared with previous materials.

Figure 7-1 Basalt fiber

Different with the previous method described in the chapter 4, the peak value of the cyclic loading applied in the fatigue test is not a constant value for different materials. For each kind of the specimen, the peak value of the cyclic loading is 75% of the break stress obtained from direct tension test. The loading rate is 1 Hz and the test temperature is -20^{o}C. The number of loading cycles and final strain for each kind of specimen before the specimen fails are recorded.

7.2 Direction tension test of asphalt binder

Three asphalt binder specimens are prepared for direct tension test. The measured and strain and stress for each specimen are plotted in the Figure 7-2.A linear regression line is drawn for each curve. The slope of each line is calculated and considered as stiffness modulus of the specimen. The break stresses and maximum strains of three are listed in the Table 7-2. The average values of the break stresses and maximum strains are calculated.

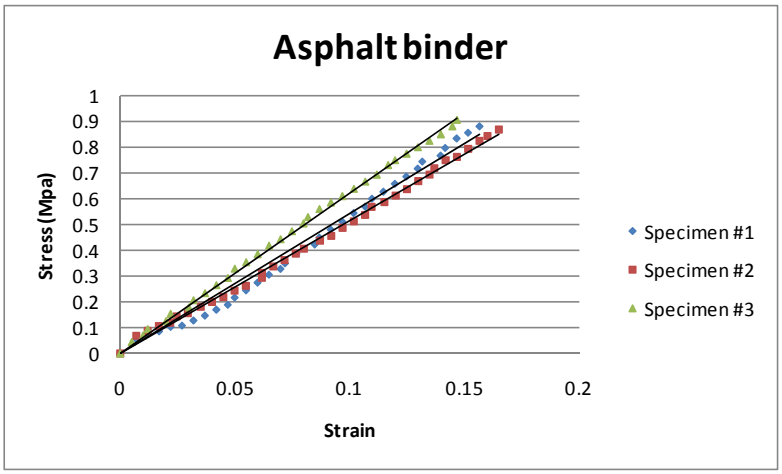

Figure 7-2 Stress-strain of asphalt binder in direct tension test

Table 7-2 Direct tension test results of asphalt binder

	Specimen #1	Specimen #2	Specimen #3
Modulus (Mpa)	5.38	5.14	6.21
Break stress (Mpa)	0.835	0.865	0.904
Break strain	0.16	0.17	0.15
Average modulus	5.58		
Average break stress (Mpa)	0.868		
Average break strain	0.16		

7.3 Direct tension test of fiber-treated asphalt binder

The basalt fibers are added in the asphalt binder to prepare the fiber-treated asphalt binder specimen. The fluidity of the fiber-treated asphalt binder specimen becomes so slow when the fiber content is higher than 1% of the weight of the asphalt binder that the specimen cannot be poured into the specimen mode. So, 0.5% of the binder weight is the fiber content added. Three 0.5% fiber-treated asphalt binder specimens are prepared and tested using direct tension test. The stress and strain of each specimen are plotted in the Figure 7-3.The stiffness modulus, break stress, maximum strain and the average results of three specimens are calculated in the Table 7-3.

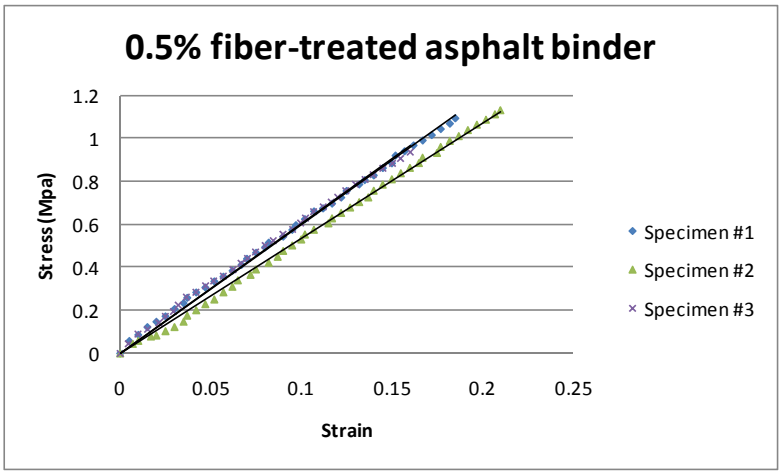

Figure 7-3 Stress-strain of 0.5% fiber-treated asphalt binder in direct tension test

Table 7-3 Direct tension test results of 0.5% fiber-treated asphalt binder

	Specimen #1	Specimen #2	Specimen #3
Modulus (Mpa)	5.99	5.34	6.04
Break stress (Mpa)	1.09	1.13	0.93
Maximum strain	0.19	0.21	0.16
Average modulus (Mpa)	5.79		
Average break stress (Mpa)	1.05		
Average maximum strain	0.19		

7.4 Direct tension test of asphalt mastic

Three asphalt mastic specimens containing 30% filler are tested using direct tension test. The stress and strain of three mastic specimens are plotted in the Figure 7-4. The stiffness modulus, break stress, maximum strain and the average results of the specimens are calculated in the Table 7-4.

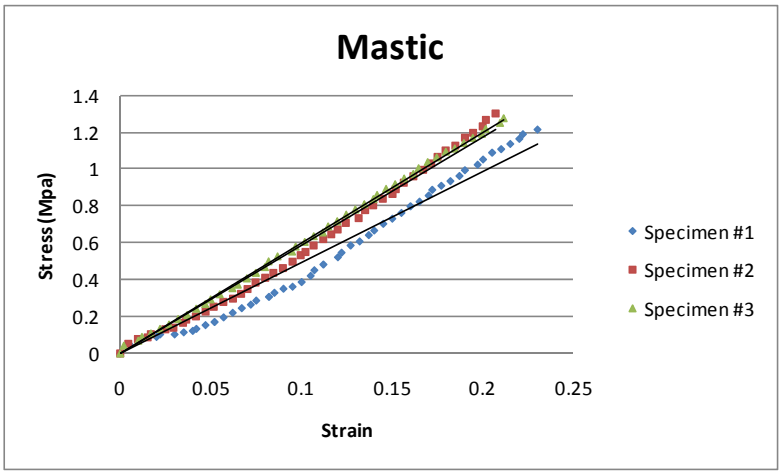

Figure 7-4 Stress-strain of 30% filler mastic in direct tension test

Table 7-4 Direct tension test results of mastic

	Specimen #1	Specimen #2	Specimen #3
Modulus (Mpa)	4.94	5.86	5.99
Break stress (Mpa)	1.21	1.30	1.27
Maximum strain	0.23	0.21	0.21
Average modulus (Mpa)	5.60		
Average break stress (Mpa)	1.26		
Average maximum strain	0.22		

7.5 Direct tension test of fiber-treated asphalt mastic

Both quartz fillers and basalt fibers are added into the asphalt binder to prepare fiber-treated mastic specimen. Since high filler and fiber content will decrease the fluidity of the specimen. The filler and fiber content are controlled so that the specimen can be prepared successfully. The filler content is 30% of the weight of the asphalt binder. The fiber content is 0.5% of the weight of the asphalt binder. The stress and strain of each specimen are plotted in the Figure 7-5. The stiffness modulus, break stress, maximum strain and average results of three specimens are listed in the Table 7-5.

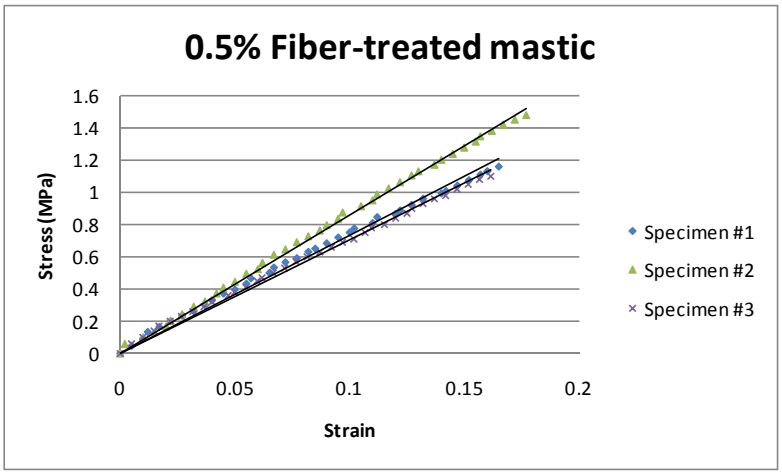

Figure 7-5 Stress-strain of fiber-treated mastic in direct tension test

Table 7-5 Modulus, break stress and maximum strain of fiber-treated asphalt mastic

	Specimen #1	Specimen #2	Specimen #3
Modulus (Mpa)	5.62	8.58	7.04
Break stress (Mpa)	1.16	1.5	1.14
Maximum strain	0.172	0.18	0.165
Average modulus (Mpa)	7.08		
Average break stress (Mpa)	1.27		
Average maximum strain	0.17		

The average direct tension test results of four different kinds of materials are listed in the Table 7-6. It can be seen that due to the addition of the fiber, the break stress of the fiber-treated asphalt binder increases about 24% compared with binder without fibers. Since the break stress of the specimen is increased, the maximum strain of the specimen is also slightly increased about 18%. The stiffness of the fiber-treated binder is also slightly higher than the pure binder. For the mastic specimens, although the break stress of the fiber-treated mastic is not much higher than the mastic specimen, the maximum strain is decreased about 20%. The high modulus fiber reduces the strain of the material under same loading level. And the stiffness modulus increases about 26%. Both of the binder and mastic test results show that, the break stress and stiffness

modulus of the specimen are increased due to the addition of the fibers. The results of mastic specimen also indicate that under same loading level, the strain of the specimen will be decreased by addition of the fiber. The direct tension test data of all four kinds of materials described above are listed in the Table 2 to Table 5 of Appendix C.

Table 7-6 Average results of direct tension test of different specimens

Specimen	Average Modulus (Mpa)	Average break stress (Mpa)	Average maximum strain
Asphalt binder	5.58	0.868	0.16
0.5% Fiber-treated asphalt binder	5.79	1.05	0.19
Asphalt mastic	5.60	1.26	0.22
0.5% Fiber-treated asphalt mastic	7.08	1.27	0.17

7.6 Fatigue test results of asphalt binder and fiber-treated asphalt binder

The direct tension test results of asphalt binder specimens show that the average break stress is 0.868 Map. Since the effective cross-section area of the specimen is 36 mm^2, the average break force of the specimen is 31N. The peak value of the cyclic loading applied on the specimen is 75% of the break force, which is 23N. The fatigue test temperature is -20^oC and the loading frequency is 1Hz. Three pure asphalt binder specimens are prepared and tested. The axial strains of the specimens are shown in the Figure 7-6.The axial strain of the asphalt binder specimens over the fatigue test are listed in the Table 7-7.The direct tension test results of 0.5% fiber-treated asphalt binder show that the average break stress is 1.05Mpa. The average break force of the specimen is 38N. The peak value of the cyclic loading applied on the specimen is 28N. The axial strains of three specimens in fatigue test are shown in the Figure 7-7. The total number of loading cycles and final axial strain of the fiber-treated asphalt binder specimens are listed in the Table 7-8.

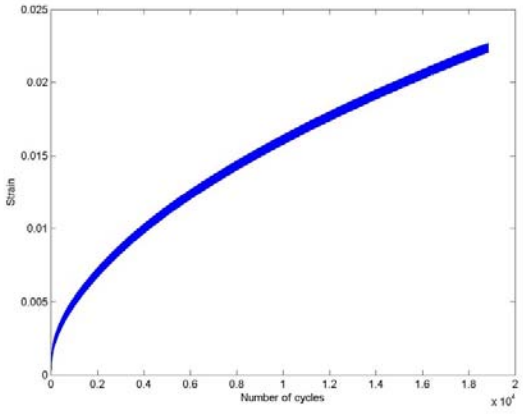

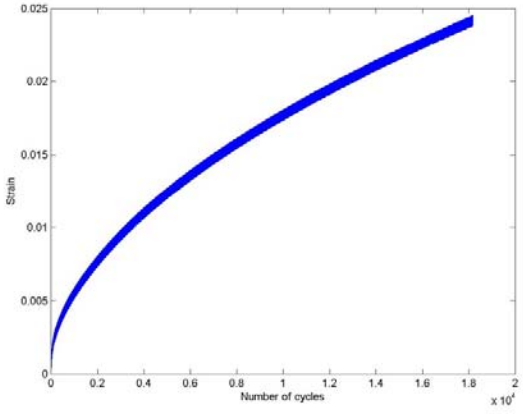

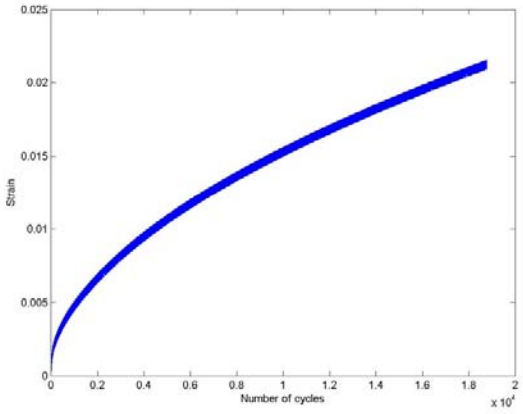

Figure 7-6 Axial strain of the asphalt binder

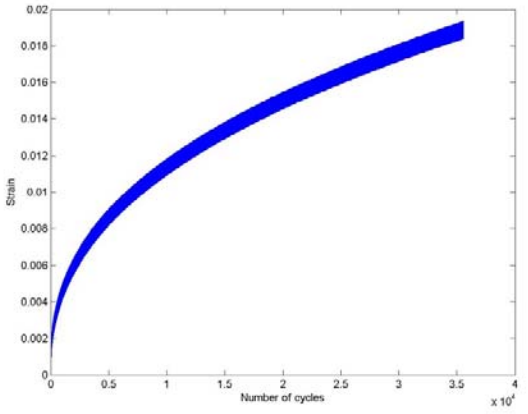

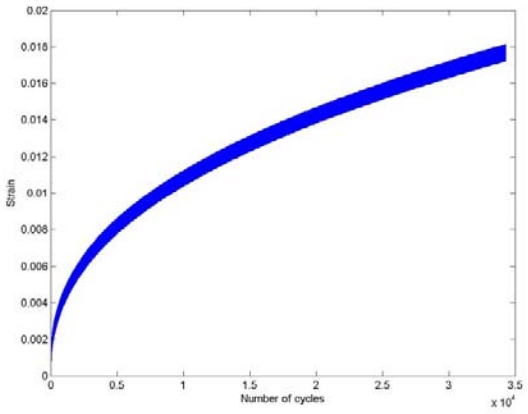

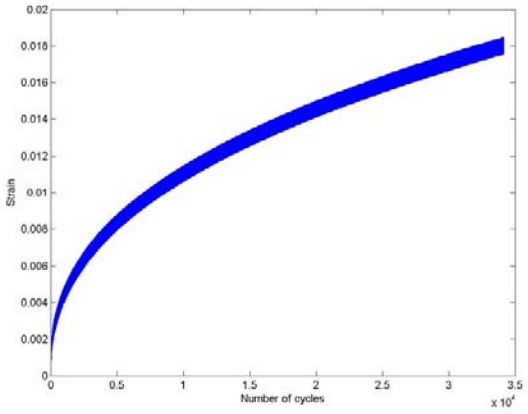

Figure 7-7 Axial strain of fiber-treated asphalt binder

Table 7-7 Fatigue test results of the asphalt binder

	Total number of loading cycles	Final axial strain
Specimen #1	18863	0.0221
Specimen #2	17175	0.0245
Specimen #3	19284	0.0215

Table 7-8 Fatigue test results of the fiber-treated asphalt binder

	Total number of loading cycles	Final axial strain
Specimen #1	35552	0.0187
Specimen #2	34316	0.0191
Specimen #3	34139	0.0178

7.7 Fatigue test results of asphalt mastic and fiber-treated mastic

The direct tension test results of mastic specimens show that the average break stress is 1.26 Mpa. The average break force of the specimen is 45N. The peak value of the cyclic loading applied on the specimen in the fatigue test is 34N. The axial strains of mastic specimens are shown in the Figure 7-8. The final strain and number of loading cycles of three specimens are listed in the Table 7-9.

The direct tension test results of fiber-treated mastic show that the average break stress is 1.27 Mpa. The average break force of the specimen is 46N. The peak value of the cyclic loading applied on the specimen in the fatigue test is 34N. The axial strains of three fiber-treated mastic specimens are shown in the Figure 7-9. The final strains and numbers of loading cycles of three specimens are listed in the Table7-10.

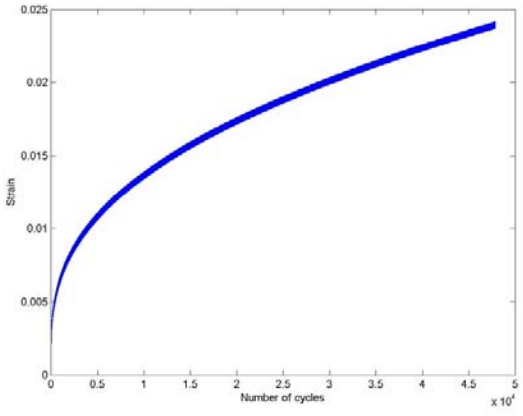

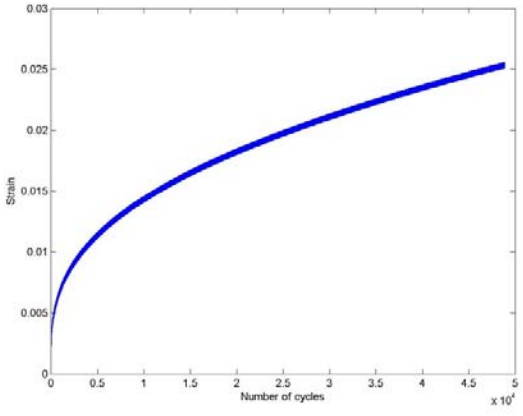

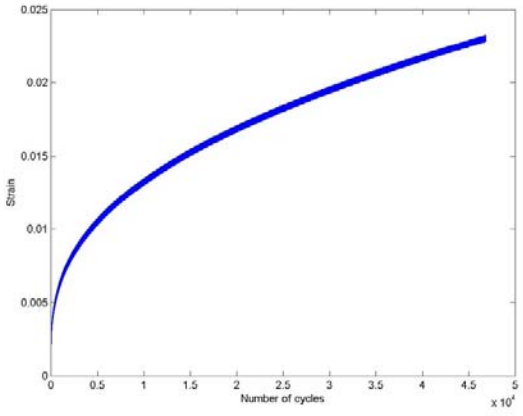

Figure 7-8 Axial strain of the mastic

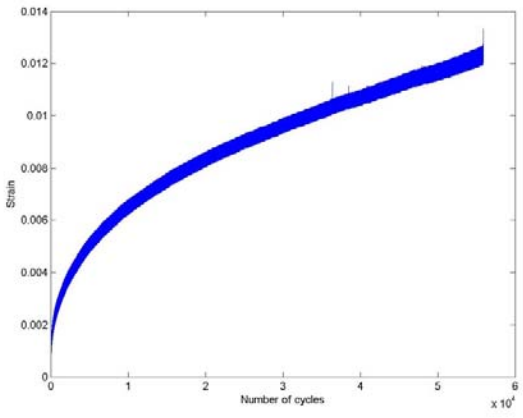

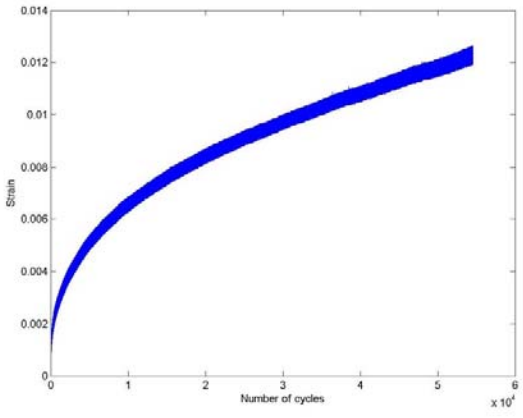

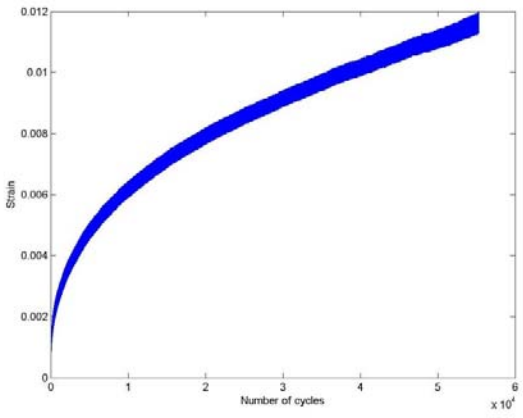

Figure 7-9 Axial strain of fiber-treated mastic

Table 7-9 Fatigue test results of the mastic specimen

	Total number of loading cycles	Final axial strain
Specimen #1	47891	0.0239
Specimen #2	48901	0.0255
Specimen #3	46880	0.0228

Table 7-10 Fatigue test results of the fiber-treated mastic specimen

	Total number of loading cycles	Final strain
Specimen #1	54012	0.0140
Specimen #2	55348	0.0133
Specimen #3	54748	0.0126

The average total number of loading cycles and final axial strain of four kinds of specimen are listed in the Table 7-11. It can be seen the addition of the fibers can improve the number of loading cycles for both binder and mastic specimens. From the asphalt binder to the fiber-treated asphalt binder, the number of loading cycles before a specimen fails increases 91%. From the mastic to the fiber-treated mastic, the total number of loading cycles before a specimen fails increases 14%. The effect of the fiber to reduce the axial strain of the specimen along the loading direction is more obvious in the fatigue test. Compared with asphalt binder, the final strain decreases 18.5% even the number of loading cycles is increased almost twice. The final strain of the fiber-treated mastic is decreased about 45% compared with mastic specimen.

Table 7-11 Average fatigue test resutls of the fiber-treated mastic specimen

Specimen	Average total number of loading cycles	Average final strain
Asphalt binder	18440	0.0227
0.5% Fiber-treated asphalt binder	34669	0.0185
Asphalt mastic	47891	0.0241
0.5% Fiber-treated asphalt mastic	54703	0.0133

From both the direct tension test and fatigue test results above, it can be seen that basalt fiber changes the performance of asphalt materials. The fiber-treated asphalt binder and mastic specimens hold longer number of loading cycles than the asphalt binder and mastic specimens

without fiber added. And, the addition of the fiber reinforces the specimens that the final axial strain of the fiber-treated materials is much smaller than the specimens without fibers.

7.8 Simulation of fiber-treated materials

7.8.1 X-ray scanning of the fiber-treated binder and mastic specimens

The effect of fiber is analyzed by adding fiber elements into the binder and mastic model. The fiber-treated binder and mastic specimens are scanned using x-ray system to view the internal structure. Since the average diameter of the basalt fiber added into the binder and mastic is only 13μm, the x-ray scanner with higher resolution is needed to view the internal structure of the fiber-treated materials. The Xradia CT-200 system (Figure 7-10) with 6 μm resolution is utilized to scan the fiber-treated materials. The size of the scanned specimens is limited so that it can be scanned by detectors with high magnification. The fiber-treated binder and mastic specimens are reshaped and put into a plastic holder for scanning (Figure 7-11). 10x magnification can be used to scan the samples. The projection view of the binder sample is shown in the Figure 7-12. The projection views of the fiber-treated mastic specimen are shown in the Figure 7-13. In the scanned images of fiber-treated mastic specimen, it can be seen that the fibers are mixed with fillers and form a tangled inter-locking structure. This internal structure is modeled using FEM to analyze the effect of the fiber to the binder and mastic in which fibers are modeled using high elastic modulus materials.

Figure 7-10 Xraida MicroCT-200 system

Figure 7-11 Specimens used for scanning

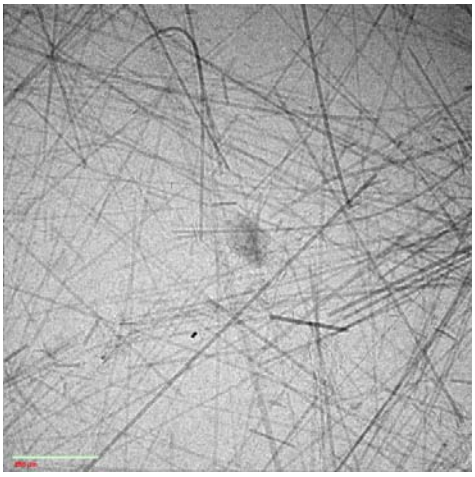

Figure 7-12 Fiber-treated asphalt binder

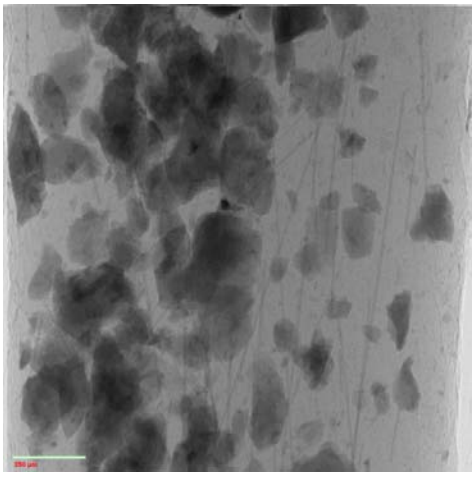

Figure 7-13 Fiber-treated mastic specimen

7.8.2 Modeling of fiber-treated asphalt binder

From the scanning images of asphalt binder, mastic, fiber-treated binder and fiber-treated mastic, it can be seen that the fibers in the fiber-treated asphalt binder and fiber-treated mastic form some inter-locking structure. This inter-locking structure is considered in the generation of digital specimens. Asphalt binder is considered as ealsto-plastic material, the properties are same

as the model used in chapter 6. Damage caused by fatigue is not considered in the direct tension simulation. Both the fillers and the fibers are considered as elastic material. The fibers have higher elastic modulus and lower Poisson's ratio. The property parameters for each material are listed in the Table 7-12. Stress and corresponding plastic strain used to calibrate parameter C and γ are listed in the Table 6-4 of Chapter 6.

Table 7-12 Parameters of model

	Elastic modulus (Mpa)	Poisson's ratio	Yield stress (Mpa)	Q	b
Binder	268.5	0.35	0.45	0.45	70
Filler	50000	0.25	/	/	/
Fiber	100000	0.15	/	/	/

The size of the model is 20mm x 20mm x 20mm shown in the Figure 7-14. The element used is brick element. The size of element is 1mm x 1mm x 1mm. The back surface of the model is fixed and a 0.6 Mpa tensile loading is applied on the front surface. A model containing asphalt binder element only is compared with a model containing a fiber with different lengths inside. The fibers are placed in two directions: along the loading direction and perpendicular to the loading direction respectively.

When the fiber is placed along the loading direction, the effect of the fiber to the element 805 at the surface is analyzed. The element 805 located at the front surface of the model along the fiber direction shown in the Figure 7-14. The axial displacements of four nodes of the element 805 at the front surface are measured. Three kinds of fibers with different lengths are added in the binder model. The axial nodal displacements are measured respectively and listed in the Table 7-

13. It can be seen when the fibers are added, the nodal displacement of the element 805 at the front surface is decreased. The longer the fiber is, the smaller the nodal displacement is.

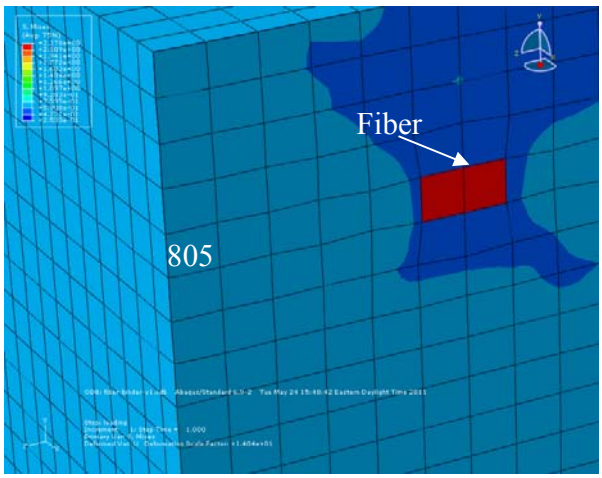

Figure 7-14 Fiber-treated binder model

Table 7-13 Axial displacement of the nodes at the surface

Node number	887	888	1328	1329
Binder	0.142	0.142	0.142	0.142
Binder + 2mm fiber	0.140	0.140	0.140	0.140
Binder + 4mm fiber	0.137	0.137	0.137	0.137
Binder + 6mm fiber	0.132	0.132	0.132	0.132

When the fiber is placed perpendicular to the loading direction shown in Figure 7-15, the nodal displacement of the element 805 at the front surface is measured and shown in the Table 7-14. Similar with previous model, the length of the fiber added into the binder model is varied from 2mm to 4mm and 6mm. The measured nodal displacement of element 805 shows that although the fiber is perpendicular to the loading direction, the nodal displacement of the element 805 at the surface is still decreased. However, compared with the previous model when the fiber is placed along the loading direction, the decrease of the nodal displacement at the surface is less.

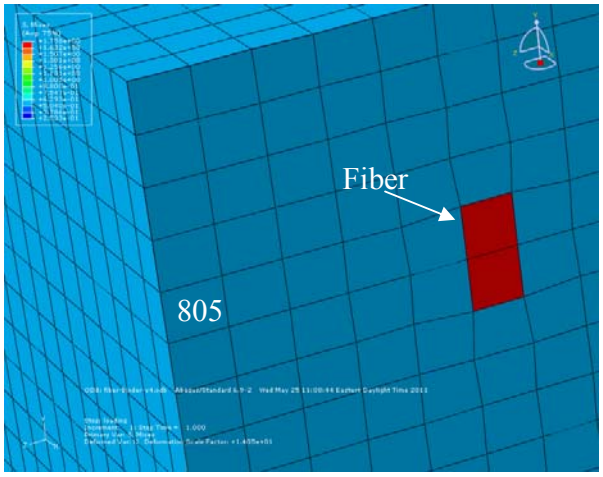

Figure 7-15 Fiber-treated binder model

Table 7-14 Axial displacement of the nodes at the surface (vertical placement of fiber)

Node number	887	888	1328	1329
Binder	0.142	0.142	0.142	0.142
Binder + 2mm fiber	0.141	0.141	0.141	0.141
Binder + 4mm fiber	0.139	0.139	0.139	0.139
Binder + 6mm fiber	0.136	0.136	0.136	0.136

When the fiber is placed along the loading direction, the contours of the axial stress of the binder and fiber-treated binder models are shown in the Figure 7-16. It can be seen that the fiber causes the stress concentration in front of and behind the fiber. The longer the fiber is, the larger the axial stress generated in front of the fiber. The contours of the axial strain of binder and fiber-treated binder models are shown in the Figure 7-17.The increased axial stress in front of and behind the fiber causes the increase of the axial strain. The longer the fiber is, the higher axial strain is caused.

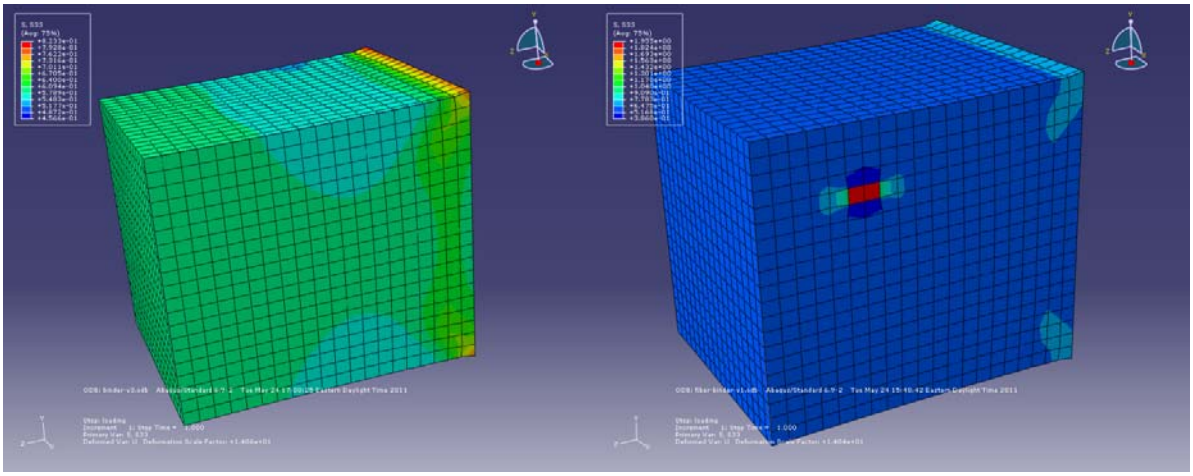

(a) Binder

(b) Binder + 2mm fiber

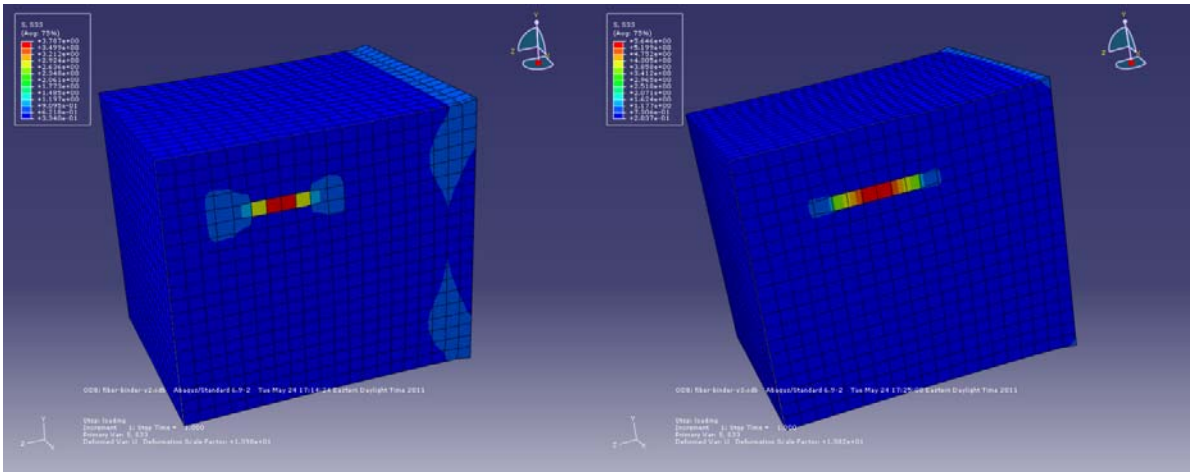

(c) Binder + 4mm fiber

(d) Binder + 6mm fiber

Figure 7-16 Contours of the axial stress of the binder and fiber-treated binder models

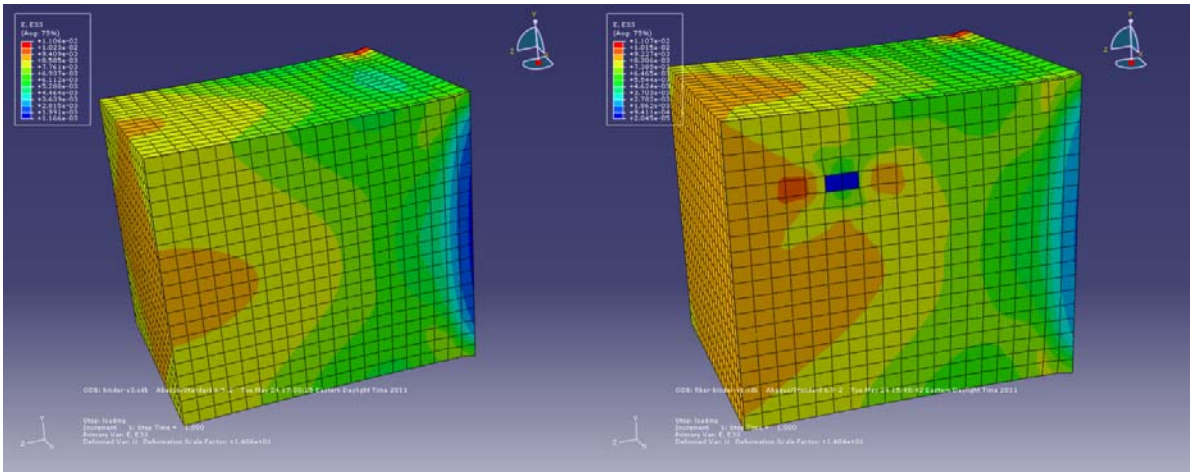

(a) Binder (b) Binder + 2mm fiber

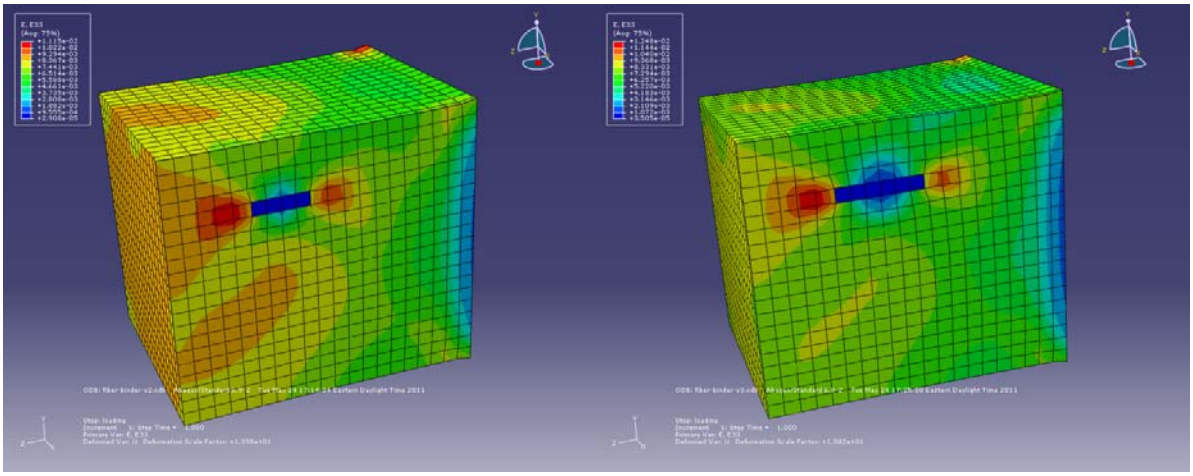

(c) Binder + 4mm fiber (d) Binder + 6mm fiber

Figure 7-17 Contours of the axial strain of the binder and fiber-treated fiber models

When the fiber is placed perpendicular to the loading direction, the contours of the axial stress of the binder and fiber-treated binder models are shown in the Figure 7-18. It can be seen that similar with the previous model, the fiber also causes the stress concentration in front of and behind the fiber. However, the length of the fiber does not affect the increase of the axial stress as much as the previous model when the fiber is placed along the loading direction. Longer fiber affects more elements in front of and behind the fiber. The contours of the axial strain of binder

and fiber-treated binder models are shown in the Figure 7-19.The increased axial stress in front of and behind the fiber also causes the increase of the axial strain, but the increase of the axial strain is not affected by the length of the fiber significantly.

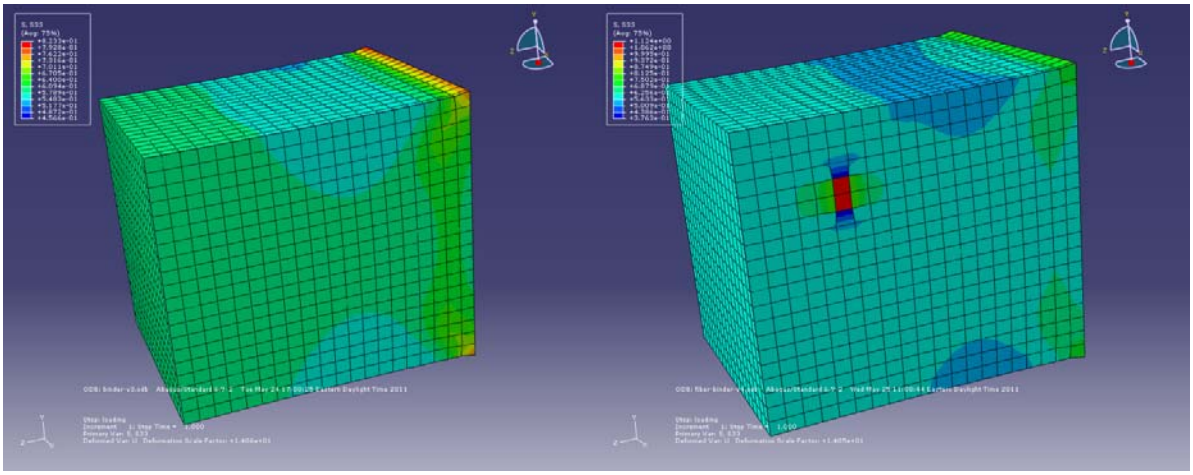

(a) Binder (b) Binder + 2mm fiber

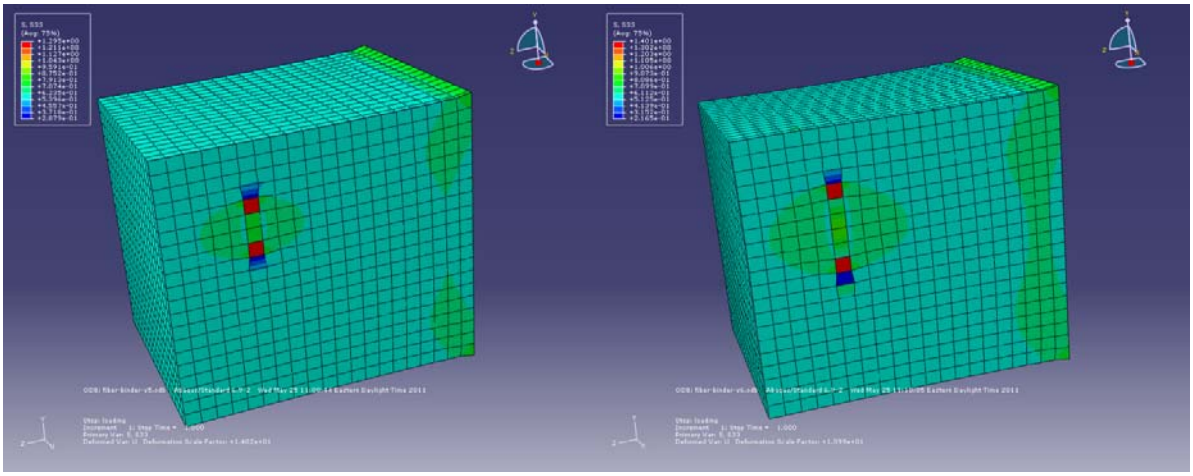

(c) Binder + 4mm fiber (d) Binder + 6mm fiber

Figure 7-18 Contours of the axial stress of the binder and fiber-treated binder models

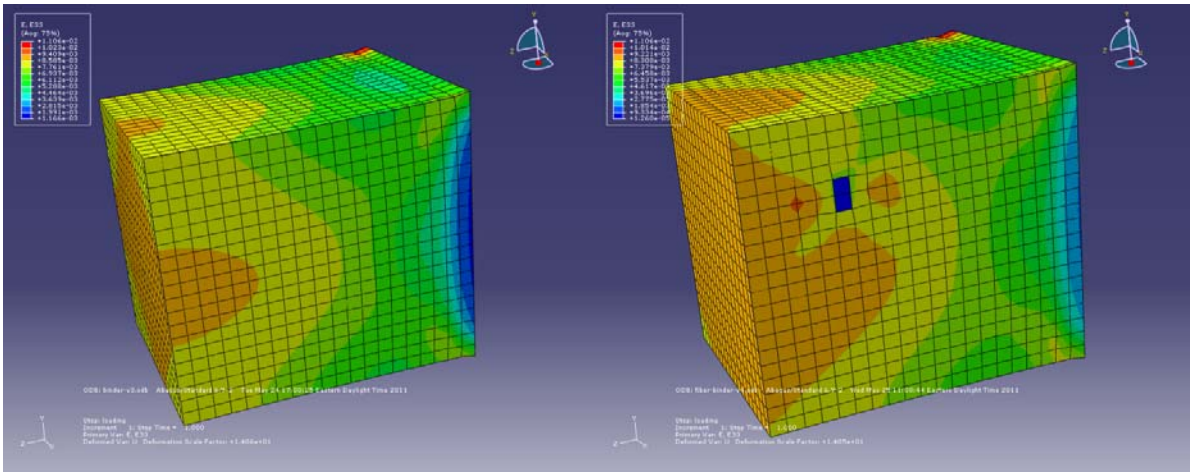

(a) Binder (b) Binder + 2mm fiber

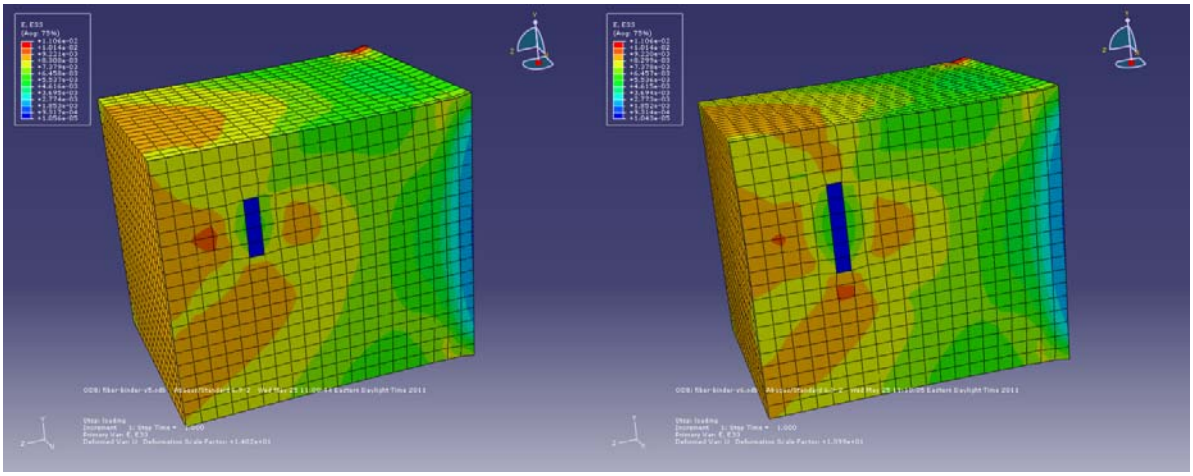

(c) Binder + 4mm fiber (d) Binder + 6mm fiber

Figure 7-19 Contours of the axial strain of the binder and fiber-treated binder models

The analysis above shows that the addition of the fiber can decrease the axial deformation of the model in the loading direction. No matter how the fibers are placed into the binder mode, both along and perpendicular to the loading direction, the addition of the fiber will cause the increase of the axial stress and corresponding axial strain in front of and behind the fiber. However, when the fiber is placed along the loading direction, the increase amount of the stress and strain is affected by the length of the fiber, the longer the fiber is, the more the stress and strain are

increased. When the fiber is placed perpendicular to the loading direction, the increase amount of the stress and strain is not closely related with the length of the fiber. This indicates that the placement of the fiber in the binder material will affect the performance of the material.

7.8.3 Stress and strain analysis of the binder and mastic model

The binder model is compared with mastic model. Same tensile loading is applied on both models. The mastic model is shown in the Figure 7-20. There are three fillers in the mastic model which are composed of elastic elements. The filler #1 is rectangular shaped filler composed of 9 elements, the size of which is 3mm in y direction by 3mm in z direction by 1mm in x direction. The filler #2 is triangular shaped filler composed of 9 elements. It is located behind the filler #1 along the loading direction. The size of the filler in y and z direction can be seen in the Figure 7-20, the size in the x direction is 1mm. Filler #3 is a smaller rectangular-shape filler composed of 4 elements. It is located under the filler #1. The size of the filler is 2mm in y and z directions respectively. It is 1mm in the x direction. All three fillers are not at the surface of the model, they are located at a surface which is 17 mm away from the x=0 surface. Without any fillers added, the axial stress s33 contour in z direction of the binder model is shown in the Figure 7-21. It can be seen from the contour that the axial stress s33 is uniformly distributed over the model. The axial stress of those elements on back surface is slightly higher because of the fixed boundary on the z direction. The axial stress s33 contour in z direction of the mastic model is shown in the Figure 7-22. Five areas before and after each filler are defined as area A1, A2, A3, A4 and A5. The axial stress of the elements in the area A1, A2, A3, A4 and A5 for both models are compared.

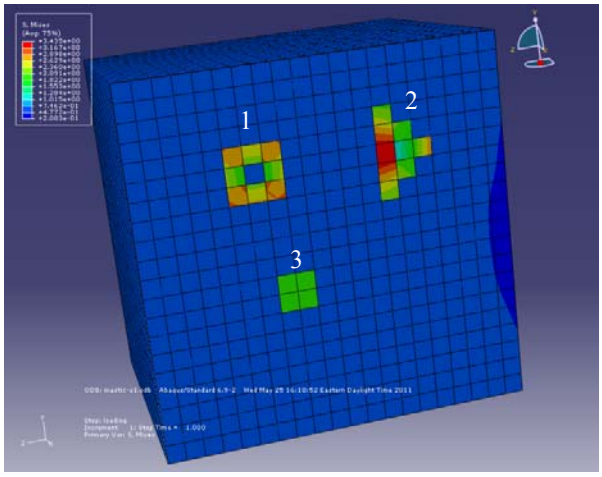

Figure 7-20 Mastic model

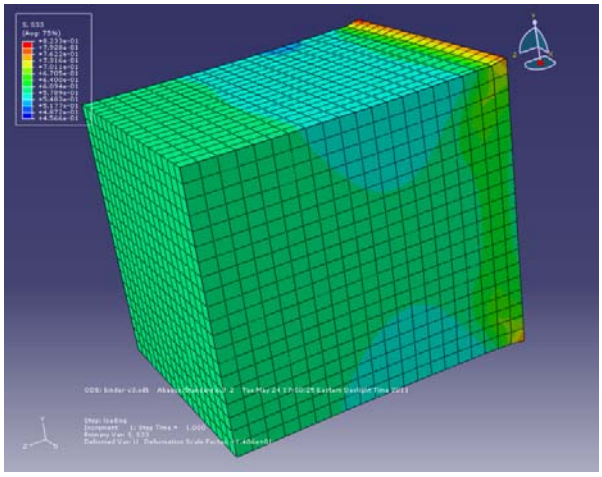

Figure 7-21 Axial stress s33 contour of the binder model

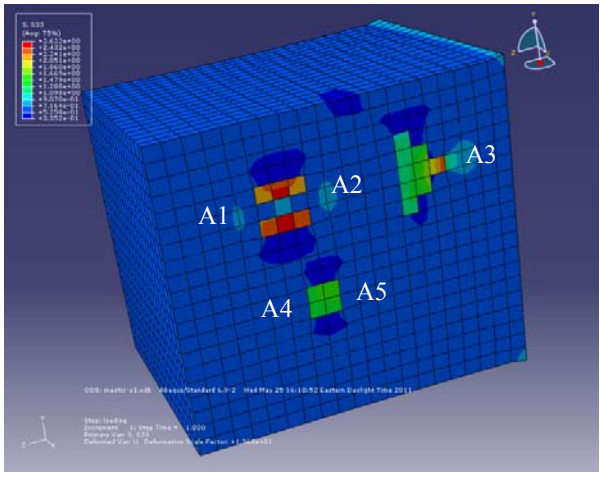

Figure 7-22 Axial stress s33 contour of the mastic model

The elements in area A1 are shown in the Figure 7-23. Area A1 includes 15 elements between the front surface and the filler #1. The axial stress of the elements in area for both binder and mastic models are listed in the Table 7-15. The axial stresses are calculated at the integration point of each element. From the binder model, it can be seen that the axial stresses are close to the tensile stress applied at the front surface of the model, 0.6Mpa. After the filler #1 is added the stress distribution in this area is changed. For those elements not close to the filler, for example, the elements 805, 806, 807, 825, 826, 827, 845, 846, 847, the axial stress is not affected significantly. The axial stress is still close to the tensile stress applied at the front surface, 0.6 Mpa. However, the axial stress of the elements next to the filler, the axial stress increased a lot. The axial stress of the element 885 is increased from 0.602 Mpa to 0.967 Mpa. The axial stress of the element 886 is increased from 0.604 Mpa to 0.827 Mpa. The axial stress of the element 887 is increased to from 0.606 Mpa to 0.974 Mpa. The average increase percentage of axial stress of the three elements is 52.7%.

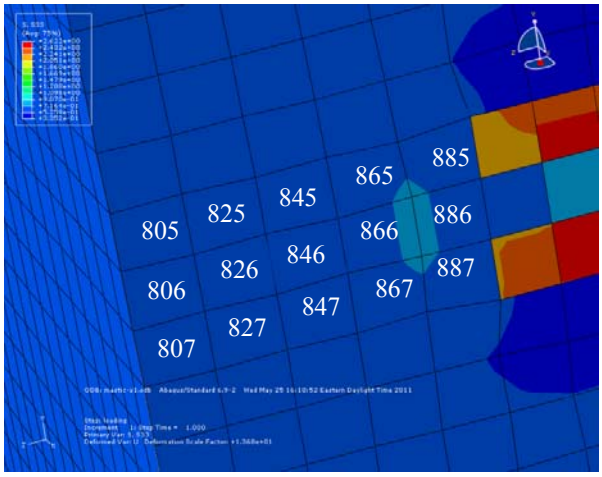

Figure 7-23 Elements in area A1

Table 7-15 Axial stress of the elements in A1 area

Element ID in A1	Binder model (Mpa)	Mastic model (Mpa)
805	0.605	0.588
825	0.605	0.605
845	0.604	0.653
865	0.603	0.617
885	0.602	0.967
806	0.606	0.601
826	0.606	0.616
846	0.606	0.601
866	0.605	0.758
886	0.604	0.827
807	0.607	0.590
827	0.607	0.606
847	0.607	0.649
867	0.607	0.615
887	0.606	0.974

The elements in area A2 are shown in the Figure 7-24. Area A2 includes 15 elements between the filler #2 and the filler #3. The axial stress of the elements in area A2 for both binder and mastic models are listed in the Table 7-16. The axial stresses are calculated at the integration point of each element. Same with elements in area A1, the axial stresses of the elements in

binder model are close to the 0.6Mpa tensile stress. However, after two fillers are added, the axial stresses of the elements in area A2 are increased. Especially for those elements next to the filler element, like elements 965, 966, 967, 1045, 1046 and 1047, the axial stresses are much higher than the binder model. The average increase percentage of axial stress of the six elements is 46%.

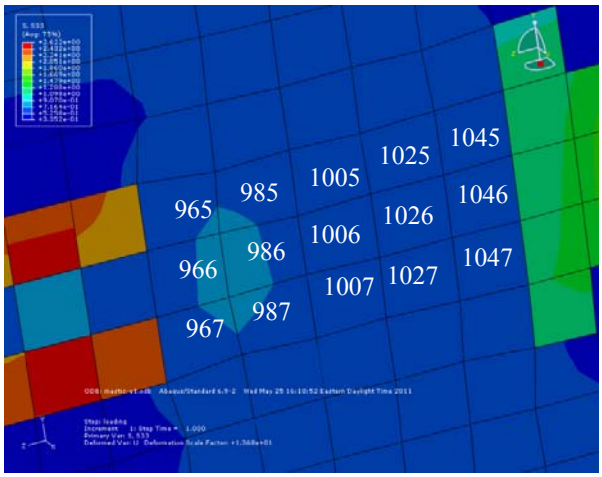

Figure 7-24 Elements in area A2

Table 7-16 Axial stress of the elements in A2 area of binder model

Element ID in A2	Binder model (Mpa)	Mastic model (Mpa)
965	0.585	0.966
985	0.583	0.638
1005	0.578	0.689
1025	0.578	0.657
1045	0.573	0.786
966	0.590	0.853
986	0.587	0.776
1006	0.585	0.655
1026	0.583	0.695
1046	0.584	0.742
967	0.592	0.996
987	0.592	0.649
1007	0.589	0.693
1027	0.591	0.660
1047	0.587	0.794

The elements in area A3 are shown in the Figure 7-25. Area A3 includes 9 elements after the filler #2. The axial stress of the elements in area A3 for both binder and mastic models are listed in the Table 7-17. The axial stresses of the elements in binder model are close to the 0.6Mpa tensile stress. From the binder model to the mastic model, the axial stress of the element 1125 increases from 0.606 Mpa to 0.703 Mpa; the axial stress of the element 1126 increases from 0.604 Mpa to 1.207 Mpa; the axial stress of the element 1127 increases from 0.592 Mpa to 0.705 Mpa. The axial stress of element 1145 increases from 0.663 Mpa to 0.801Mpa. The axial stress 1147 increases from 0.641 Mpa to 0.810 Mpa. Especially, at the tip of the triangular filler, the axial stress of the element 1126 increases about twice larger than the binder model. The other elements further away from the filler are not significantly affected and the axial stresses are close to the stresses in the binder model.

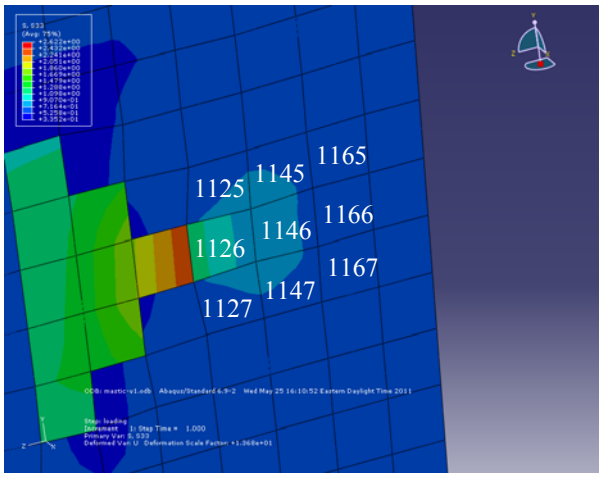

Figure 7-25 Elements in area A3

Table 7-17 Axial stress of the elements in A3 area of binder model

Element ID in A3	Binder model (Mpa)	Mastic model (Mpa)
1125	0.606	0.703
1145	0.663	0.801
1165	0.634	0.622
1126	0.604	1.207
1146	0.646	0.604
1166	0.631	0.737
1127	0.592	0.705
1147	0.641	0.810
1167	0.621	0.617

The elements in area A4 are shown in the Figure 7-26. Area A4 includes 6 elements located in front of the filler #3. The axial stress of the elements in area A4 for both binder and mastic models are listed in the Table 7-18. The axial stresses of the elements in binder model are close to the 0.6Mpa tensile stress. Same with area A1, the axial stress of the elements close to the filler is increased a lot compared with binder model. From the binder model to the mastic model, the axial stress of the element 932 increases from 0.597 Mpa to 0.909 Mpa; the axial stress of the

element 933 increases from 0.597 Mpa to 0.888 Mpa. The average increase percentage is 51%. The axial stress of elements 892, 893, 912 and 913 is not affected a lot because they are further away from the filler.

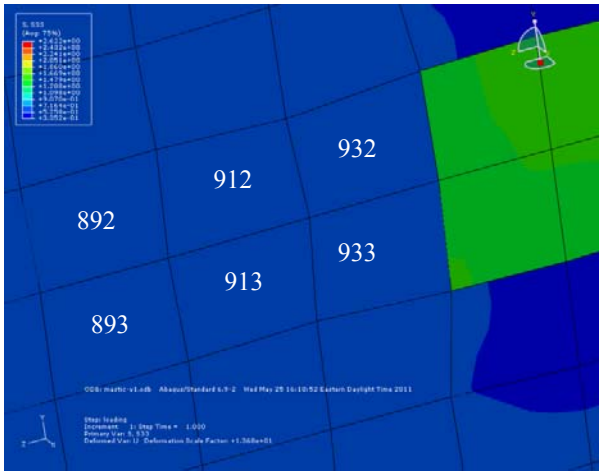

Figure 7-26 Elements in area A4

Table 7-18 Axial stress of the elements in A4 area of binder model

Element ID in A4	Binder model (Mpa)	Mastic model (Mpa)
892	0.598	0.631
912	0.598	0.625
932	0.597	0.909
893	0.598	0.604
913	0.598	0.658
933	0.597	0.888

The elements in area A5 are shown in the Figure 7-27. Area A5 includes 6 elements located behind the filler #3. The axial stress of the elements in area A5 for both binder and mastic models are listed in the Table 7-19. The axial stresses of the elements in binder model are close to the 0.6Mpa tensile stress. The axial stress of the elements close to the filler is increased a lot. From the binder model to the mastic model, the axial stress of the element 992 increases from 0.598 Mpa to 0.909 Mpa; the axial stress of the element 993 increases from 0.595 Mpa to 0.865

Mpa. The average increase percentage is 49%. The axial stress of elements 1012, 1032, 1013 and 1033 is not affected a lot because they are further away from the filler.

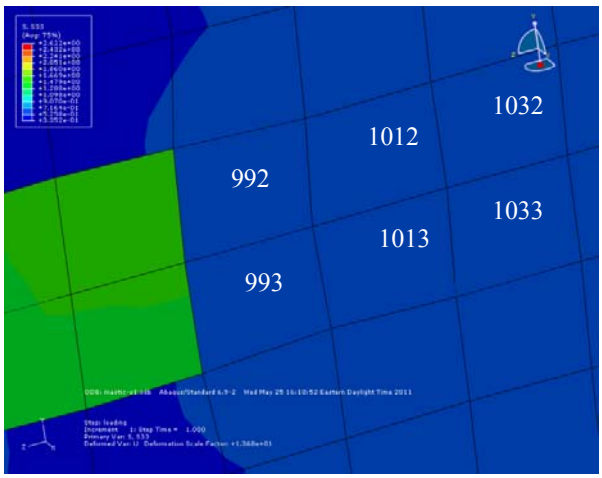

Figure 7-27 Elements in area A5

Table 7-19 Axial stress of the elements in A5 area of binder model

Element ID in A5	Binder model (Mpa)	Mastic model (Mpa)
992	0.598	0.909
1012	0.597	0.614
1032	0.599	0.625
993	0.595	0.865
1013	0.595	0.645
1033	0.594	0.592

The axial stress analysis of the elements in five areas described above show that when the filler is added into the binder, the axial stress in front of and behind the filler is increased along the loading direction. The axial stress increases more for those elements located closer to the fillers. Especially, for the elements between two fillers along the loading direction, the axial stresses of all the elements are increased. The increased axial stress will cause the change of the strain distribution which will be analyzed below. The contour of axial strain e33 of the binder model is shown in the Figure 7-28 and axial strain e33 of the mastic model is shown in the Figure 7-29.

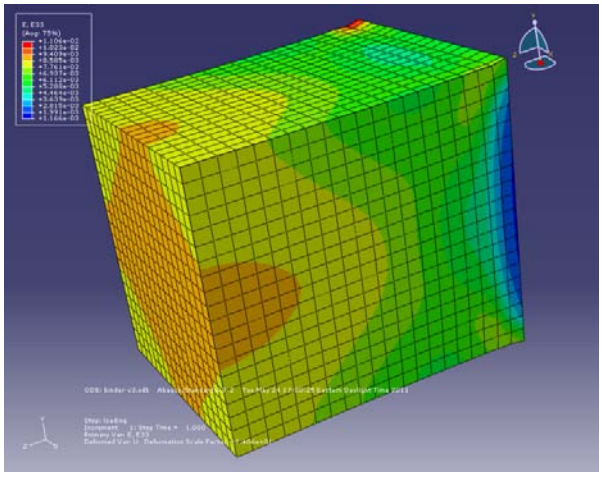

Figure 7-28 Contour of axial strain e33 of the binder model

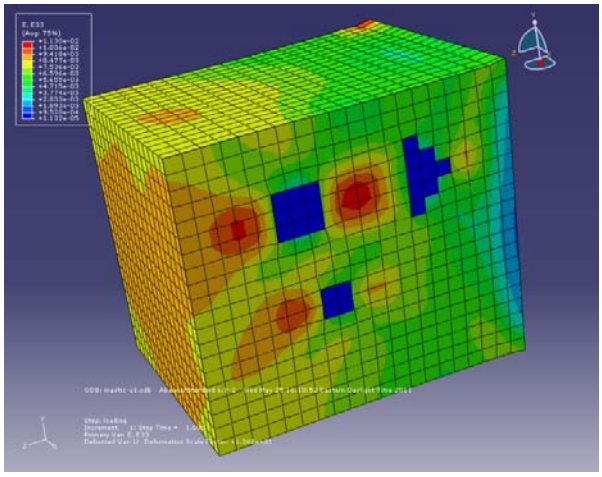

Figure 7-29 Contour of axial strain e33 of the mastic model

The axial strain of the elements in area A1 for both binder and mastic models are listed in the Table 7-20. It can be seen that the axial strain distribution of the binder model is uniformly distributed. The axial strain under 0.6 Mpa tensile stress is around 0.0085 for all the elements. The axial strain of the elements of mastic model is changed due to the addition of the filler. The previous axial stress analysis shows that the axial stress is concentrated in front of and behind the filler elements. The increased stress causes the increase of the axial strain. It can be seen from

the results below that the axial strain of the elements in mastic model is increased compared with binder model. Especially for those elements closer to the filler elements, the axial strains are larger than those elements further away from the filler. This is reasonable because the axial stress caused on these elements is also larger than those elements further away from the filler. The average increase of the axial stress in area A1 from binder model to the mastic model is 18%.

Table 7-20 Axial strain of the elements in area A1

Element ID in A1	Binder model	Mastic model
805	0.0085	0.0086
825	0.0085	0.01
845	0.0085	0.0091
865	0.0084	0.0114
885	0.0083	0.0112
806	0.0086	0.0092
826	0.0085	0.0095
846	0.0085	0.0098
866	0.0085	0.0134
886	0.0084	0.0089
807	0.0086	0.0087
827	0.0086	0.01
847	0.0086	0.009
867	0.0086	0.011
887	0.0085	0.011

The axial strains of the elements in other four areas for both binder and mastic model are listed in Table 7-21 to Table 7-24. Same conclusion can also be made for the elements in other four areas. The stress concentration in front of and behind the filler elements causes the increase of the strain along the loading direction. The increase of the strain is also related with the position of the element. The axial strain is larger at the elements closer to the filler elements.

Table 7-21 Axial strain of the elements in area A2

Element ID in A2	Binder model	Mastic model
965	0.0078	0.0109
985	0.0075	0.0119
1005	0.0074	0.0086
1025	0.0070	0.0112
1045	0.0070	0.0070
966	0.0079	0.0089
986	0.0077	0.0144
1006	0.0075	0.0105
1026	0.0073	0.0104
1046	0.0071	0.0068
967	0.0081	0.0116
987	0.0079	0.0129
1007	0.0077	0.0089
1027	0.0074	0.0114
1047	0.0072	0.0072

Table 7-22 Axial strain of the elements in area A3

Element ID in A3	Binder model	Mastic model
1125	0.0065	0.0089
1145	0.0063	0.0086
1165	0.0039	0.0048
1126	0.0061	0.0123
1146	0.0058	0.0103
1166	0.0036	0.0034
1127	0.0057	0.0082
1147	0.0056	0.0078
1167	0.0033	0.0043

Table 7-23 Axial strain of the elements in area A4

Element ID in A4	Binder model	Mastic model
892	0.0087	0.009
912	0.0086	0.0117
932	0.0086	0.011
893	0.0086	0.0087
913	0.0086	0.0122
933	0.0085	0.0109

Table 7-24 Axial strain of the elements in area A5

Element ID in A5	Binder model	Mastic model
992	0.0082	0.0096
1012	0.0080	0.0106
1032	0.0076	0.0074
993	0.0081	0.0098
1013	0.0078	0.0104
1033	0.0075	0.0072

7.8.4 Stress and strain analysis of the mastic and fiber-treated mastic model

To analyze the effect of fibers to the mastic material, a fiber-treated mastic model is generated. The model has same fillers as the mastic model. The fiber is modeled with elastic element with higher elastic modulus and lower Poisson's ratio than the filler material. One fiber is added between filler #1 and filler #2. Five binder elements are replaced by fiber elements. Another fiber is added between fiber #1 and fiber #3. This internal structure is generated to model the inter-locking structure observed from the x-ray scanning of fiber-treated mastic materials. The fibers are tangled with fillers and behave like bridges among fillers. The fiber-treated mastic model is shown in the Figure 7-30.

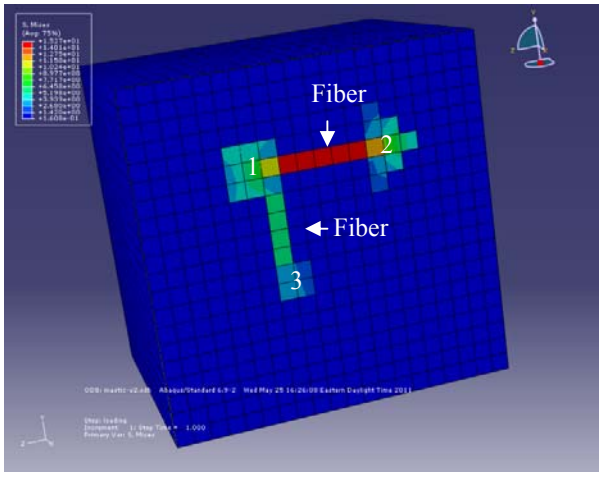

Figure 7-30 Mastic and fiber-treated mastic model

The contour of the axial stress of fiber-treated mastic model is shown in the Figure 7-31. The axial stresses of the elements in the five defined areas are measured for both mastic and fiber-treated mastic model.

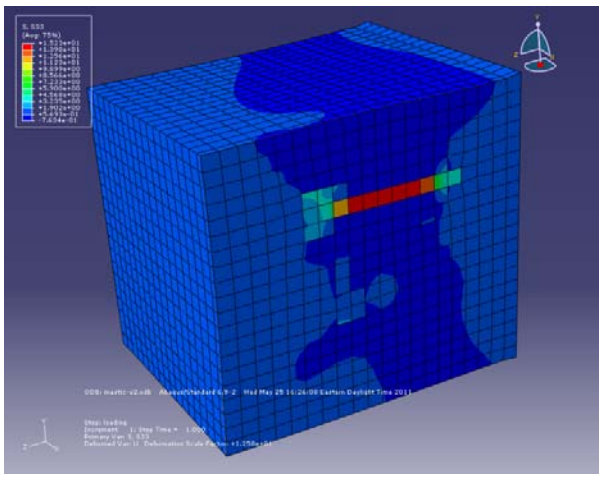

Figure 7-31 Contour of axial stress of fiber-treated mastic model

The axial stresses of the elements in area A1 for both mastic and fiber-treated mastic model are listed in the Table 7-25. Due to the addition of the fiber between filler #1 and filler #2, the axial

stresses of the elements next to the filler #1 are increased. From the mastic model to the fiber-treated mastic model, the axial stress of the element 885 increases from 0.967 Mpa to 1.197Mpa; the axial stress of the element 886 increases from 0.827 Mpa to 0.969 Mpa; the axial stress of the element 887 increases from 0.974 Mpa to 1.144 Map. The average axial stress increase of the three elements is 19%.

Table 7-25 Axial stresses of the elements in area A1

Element ID in A1	Mastic model (Mpa)	Fiber-treated mastic model (Mpa)
805	0.588	0.585
825	0.605	0.607
845	0.653	0.672
865	0.617	0.615
885	0.967	1.197
806	0.601	0.596
826	0.616	0.626
846	0.601	0.613
866	0.758	0.810
886	0.827	0.969
807	0.590	0.589
827	0.606	0.605
847	0.649	0.684
867	0.615	0.643
887	0.974	1.144

The axial stresses of the elements in area A2 for both mastic and fiber-treated mastic model are listed in the Table 7-26. In the fiber-treated mastic model, the elements 966, 986, 1006, 1026, 1046 are replaced by the fiber elements. The axial stresses on these elements are not measured. The other 10 elements in this area are measured and compared. It can be seen that due to the addition of the fiber between filler #1 and filler #2, the axial stresses of the elements in this area are significantly decreased. The average axial stress decrease of these elements is 85%. From the previous comparison between the binder and mastic model, the stress concentration between

filler #1 and filler #2 in the mastic model is released to a large extent by the addition of the fiber elements.

Table 7-26 Axial stress of the elements in area A2

Element ID in A2	Mastic model (Mpa)	Fiber-treated mastic model (Mpa)
965	0.966	0.013
985	0.638	0.088
1005	0.689	0.066
1025	0.657	0.165
1045	0.786	-0.095
966	0.853	/
986	0.776	/
1006	0.655	/
1026	0.695	/
1046	0.742	/
967	0.996	-0.089
987	0.649	0.289
1007	0.693	0.218
1027	0.660	0.292
1047	0.794	0.032

The axial stresses of the elements in area A3 for both mastic and fiber-treated mastic models are listed in the Table 7-27. The results show that similar with the elements in area A1, the addition of the fiber causes slight increase of the axial stress in this area. The average axial stress increase of these elements is 9%. The axial stresses of the elements in area A4 for both mastic and fiber-treated mastic models are listed in the Table 7-28. It can be seen that since fiber between the filler #1 and filler #3 is perpendicular to the loading direction, the effect of the fiber to the axial stress distribution of the elements in area A4 is not significantly affected. The average axial stress of the elements in this area decreases about 5%. The axial stresses of the elements in area A5 for both mastic and fiber-treated mastic models are listed in the Table 7-29. The axial stress concentration of the elements in this area observed in the mastic model is released. Compared

with mastic model, the axial stress of the elements in this area is decreased. The average axial stress decrease of the elements is 9%.

Table 7-27 Axial stress of the elements in area A3

Element ID in A3	Mastic model (Mpa)	Fiber-treated mastic model (Mpa)
1125	0.703	0.784
1145	0.801	0.889
1165	0.622	0.610
1126	1.207	1.544
1146	0.604	0.596
1166	0.737	0.797
1127	0.705	0.793
1147	0.810	0.905
1167	0.617	0.614

Table 7-28 Axial stress of the elements in area A4

Element ID in A4	Mastic model (Mpa)	Fiber-treated mastic model (Mpa)
892	0.631	0.589
912	0.625	0.656
932	0.909	0.747
893	0.604	0.592
913	0.658	0.541
933	0.888	0.933

Table 7-29 Axial stress of the elements in area A5

Element ID in A5	Mastic model (Mpa)	Fiber-treated mastic model (Mpa)
992	0.909	0.797
1012	0.614	0.599
1032	0.625	0.563
993	0.865	0.769
1013	0.645	0.563
1033	0.592	0.563

The axial stress analysis above shows that if the fiber is placed along the loading direction between two fillers, like the fiber between filler #1 and filler #2, the axial stress is slightly increased in front of the filler #1 and behind the filler #2. However, for the area between two

fillers, the axial stress is significantly decreased due the addition of the fiber. The stress concentration between two fillers in the mastic model is released to a large extent. The change of the stress distribution will cause the change of the strain distribution. The axial strain of the elements in the defined areas is measured. The contours of axial strain of the mastic model and fiber-treated mastic model are shown in the Figure 7-32 and Figure 7-33 respectively.

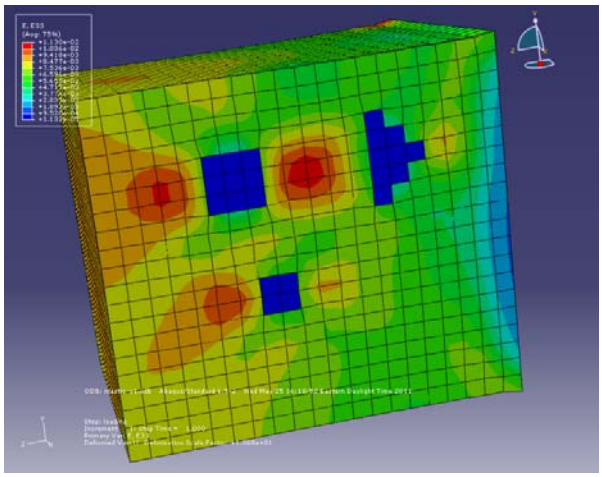

Figure 7-32 Contour of axial strain of mastic model

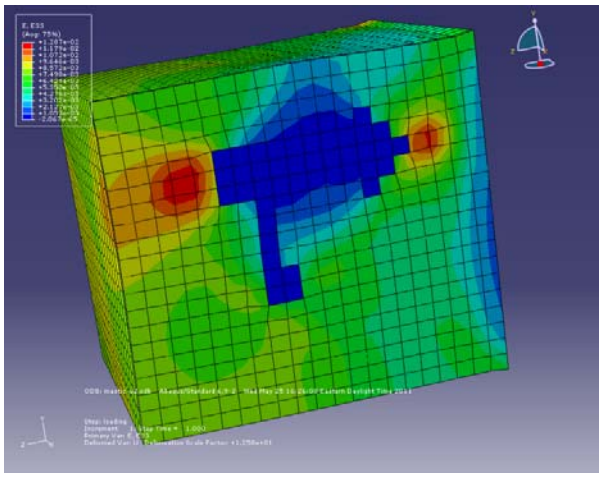

Figure 7-33 Contour of axial strain of fiber-treated mastic model

The axial strain of the elements in A1 area is listed in the Table 7-30. The previous stress analysis shows that the axial stress is increased in this area from mastic model to the fiber-treated mastic model. So, the axial strain is also increased in this area shown in the table below. The average strain increase is this area is 19%. The axial strain of the elements in area A2 for both models is shown in the Table 7-31. It can be seen since the stress concentration is this area is released to a large extent due to the addition of the fiber. Very small axial stress is generated for the elements in this area of the fiber-treated mastic model. Compared with the mastic model, the average axial strain of the elements decreases 99%. The axial strain of the elements in area A3 is shown in the Table 7-32. Similar with the elements in area A1, the increased axial stress in this area causes the increase of the axial strain. The average axial strain increases 36%. The axial strain of the elements in area A4 is shown in the Table 7-33. The axial strain of the elements in this areas decreases because of the decrease of the axial stress described previously. The average axial strain decrease of the elements in this area is 21%. The axial strain of the elements in area A5 is shown in the Table 7-34. The decreased axial stress causes the decrease of the axial strain. The average axial strain increases 36%.

Table 7-30 Axial strain of the elements in A1 area

Element ID in A1	Mastic	Fiber-treated mastic
805	0.0086	0.0089
825	0.0099	0.011
845	0.0091	0.0096
865	0.0114	0.0145
885	0.0112	0.0165
806	0.0092	0.0097
826	0.0094	0.0106
846	0.0097	0.011
866	0.0134	0.017
886	0.0088	0.0121
807	0.0087	0.0093
827	0.01	0.0111
847	0.009	0.0104
867	0.0115	0.014
887	0.0114	0.015

Table 7-31 Axial strain of the elements in area A2

Element ID in A2	Mastic	Fiber-treated mastic
965	0.0109	0.0003
985	0.0120	0.0004
1005	0.0086	0.0001
1025	0.0112	0.0004
1045	0.0070	-0.0004
967	0.0116	-0.0005
987	0.0129	0.0006
1007	0.0089	0.0008
1027	0.0114	0.0009
1047	0.0072	0.0001

Table 7-32 Axial strain of the elements in area A3

Element ID in A3	Mastic	Fiber-treated mastic
1125	0.0089	0.0128
1145	0.0086	0.0110
1165	0.0048	0.0060
1126	0.0123	0.0185
1146	0.0104	0.0153
1166	0.0034	0.0037
1127	0.0082	0.0132
1147	0.0078	0.0100
1167	0.0043	0.0055

Table 7-33 Axial strain of the elements in A4

Element ID in A4	Mastic	Fiber-treated mastic
892	0.0090	0.0074
912	0.0118	0.0092
932	0.0110	0.0067
893	0.0087	0.0061
913	0.0122	0.0093
933	0.0107	0.0111

Table 7-34 Axial strain of the elements in A5

Element ID in A5	Mastic	Fiber-treated mastic
992	0.0096	0.0068
1012	0.0106	0.0087
1032	0.0074	0.0058
993	0.0098	0.0080
1013	0.0104	0.0077
1033	0.0072	0.0057

The axial strain of the elements in area A1 and A3 shows that due to the addition of fiber, the axial strains of the elements in the two areas are slightly increased. This is similar with mastic model. When the high modulus filler is added into binder, the axial stress in front of and behind the filler is increased. The increase axial stress causes the increase of the axial strain. Average

axial strain of the elements in these two areas increases about 18.5 % and 36% respectively. In the area A2, where the fiber elements are added between filler #1 and filler #2, the axial stress concentration between two fillers is released by the addition of the filler. Average axial strain decreases about 97.7% in this area from mastic model to the fiber-treated mastic model. The fiber added makes the interface area between two fillers much stronger. The fillers and the fiber form an interlocking structure providing higher resistance to the external loading. The fiber added between filler #1 and filler #3 changes the axial strain distribution around the filler #3, the axial strain in front of and behind the filler #3 decreases 21.3% and 22.4% respectively.

The axial stress and strain analysis of mastic and fiber-treated mastic models above show that under a tensile loading, the axial stress along the loading direction in front of and behind the filler will be increased. The increased stress causes the increase of the axial strain. Especially for the interface area, the axial stress and strain are much larger. After the fiber is added between two fillers placed along the loading direction, the stress and strain distribution is affected. The stress and strain in front of and behind two fillers are slightly increased. However, the stress and strain of the interface area are significantly decreased due to the addition of the fiber. The stress concentration in the interface area between two fillers is released to a large extent. When two fillers are placed perpendicularly to the loading direction, the fiber added between two fillers forms a bridge between two fillers and decrease the axial stress and axial strain in front of and behind the filler.

7.8.5 Fatigue analysis of the mastic and fiber-treated mastic model

To further analyze the effect of the fiber to the mastic material, fatigue loading is applied on both the mastic and fiber-treated mastic model. Instead of the tensile loading, a cyclic loading is applied on the front surface of mastic model and fiber-treated mastic model respectively. The damage model used in the chapter 6 is applied to both mastic and fiber-treated mastic models. The damage model parameter c1is adjusted so that the fatigue damage is early initiated to reduce the computational time. The other damage parameters are same with previous fatigue modeling of mastic materials described in the chapter 6. The damage model parameter c1=0.01, c2= -1.45, c3=5 and c4=1.15. The peak value of the sinusoidal cyclic loading is increased to 0.8Mpa so that the fatigue damage is easy to initiate. The loading frequency is 0.5Hz. The number of total loading cycles applied is 100. The elastic modulus of the binder elements will be decreased due to the fatigue damage. The loss of the elastic modulus of the elements in five defined areas for both mastic and fiber-treated mastic model are measured by stiffness degradation parameter SDEG respectively.

The SDEG of the elements in area A1 for both models is listed in the Table 7-35. In the mastic model, after the fatigue process, some elements lost their stiffness completely, like element 865, 885, 866, 886, 867, 887. Since these elements are closer to the filler elements, the axial strain generated in the area closer to the filler elements is larger, which agree with the previous axial stress analysis of the model under direct tensile stress. The previous axial stress of fiber-treated mastic model also shows that after the fiber is added between filler #1 and filler #2, the axial stress in the area A1 is increased. So after the fatigue process, the elements in area A1 of fiber-treated mastic model lost more stiffness. Some elements which have not completely lost their

stiffness in mastic model are completely damage in the fiber-treated mastic model, like elements 825, 845, 846, 807, 827, 847.

Table 7-35 Stiffness loss of the elements in area A1

Element ID in A1	Mastic (%)	Fiber-treated mastic (%)
805	64	87
825	64	100
845	70	100
865	100	100
885	100	100
806	65	93
826	66	94
846	74	100
866	100	100
886	100	100
807	64	100
827	64	100
847	70	100
867	100	100
887	100	100

The SDEG of the elements in area A2 for both models is listed in the Table 7-36. In the mastic model, after the fatigue process, most of the elements lost their stiffness completely due the stiffness concentration between two fillers. However, after the fiber is added, the axial strain caused between two fillers is decreased to a large extent. The fatigue test results of fiber-treated mastic model show that after same number of loading cycles, the fatigue damage has not been initiated in the elements of area A2. There is no stiffness loss in this area. The fiber behaves as a bridge between two fillers and release stress concentration between them which improves the fatigue resistance of the structure.

Table 7-36 Stiffness loss of the elements in area A2

Element ID in A2	Mastic	Fiber-treated mastic
965	100	0
985	100	0
1005	90	0
1025	100	0
1045	67	0
967	100	0
987	100	0
1007	92	0
1027	100	0
1047	76	0

The SDEG of the elements in area A3 for both models is listed in the Table 7-37. Similar with area A1, the addition of the fiber between two fillers causes the increase of the axial stress in the area A3. After the fatigue process, the elements in this area of fiber-treated mastic model lost more stiffness compared with the mastic model.

Table 7-37 Stiffness loss of the elements in area A3

Element ID in A3	Mastic	Fiber-treated mastic
1125	100	100
1145	66	100
1165	62	82
1126	100	100
1146	57	100
1166	61	83
1127	100	100
1147	91	100
1167	54	74

The SDEG of the elements in area A4 for both models is listed in the Table 7-38. The fiber between the filler #1 and filler #3 causes the decrease of the axial stress in the area A4, the stiffness loss of the elements in this area of fiber-treated mastic model is less than the mastic model after the fatigue process. Some elements which are damaged in the mastic model, like

element 912 and 913, have not lost their stiffness completely in the fiber-treated mastic model. The fiber added between filler #1 and filler #3 forms a structure together with two fillers which has higher fatigue resistance.

Table 7-38 Stiffness loss of the elements in area A4

Element ID in A4	Mastic (%)	Fiber-treated mastic (%)
892	69	67
912	98	78
932	100	90
893	70	64
913	100	73
933	100	100

The SDEG of the elements in area A5 for both models is listed in the Table 7-39. Similar with the elements in area A4, the axial strain in this area is decreased after the fiber is added between filler #1 and filler #3. After same number of loading cycles, the fatigue damage caused in this area of fiber-treated mastic model is less than the mastic model.

Table 7-39 Stiffness loss of the elements in area A5

Element ID in A5	Mastic (%)	Fiber-treated mastic (%)
992	100	91
1012	98	71
1032	65	51
993	100	100
1013	91	61
1033	66	51

The faituge analysis above shows that similar with stress and strai analysis of the model under tensile stress, when the fibers are added among fillers, the fatigue resistance of the materials is significantly affected. If the fiber is placed along the loading direction between two fillers, the increased strain in front of and behind the fillers causes more loss of the stiffness. However, the

stress concentration between two fillers is released to a large extent, the strain caused by cyclic loading in this interface area is limited a lot by the fiber so the the materials between two fillers has much higher fatigue resistance than the mastic model. When the fiber between two fillers is not along the loading direction, it behaves as a brigde and froms a stronger internal structure together with the fillers. The simulation results provide a good explaination to the observation from the lab fatigue test results.

To analyze the effect of the positon and displacement of the fiber to the performance of the mastic material, the placement position of the fiber is changed in a refined fiber-treated mastic model. The size of the model and the applied loading are still same with the previous model, however, both of the models are refined using smaller mesh shown in the Figure 7-34. The size of the mesh is 0.5mm x 0.5mm x 0.5mm. Filler is added into the binder materials, the size of the which is 3mm x 3mm x 3mm. The contours of axial stress and strain of the mastic model are shown in the cut view in Figure 7-35 and Figure 7-36. In the fiber-treated mastic model, a 5mm long fiber is placed in three differenet postions. In the first model, the fiber is placed in x direction in front of the filler. In the second model, the fiber is placed in x direction but behind the filler. In the third model, the fiber is placed in z direction beside the filler.

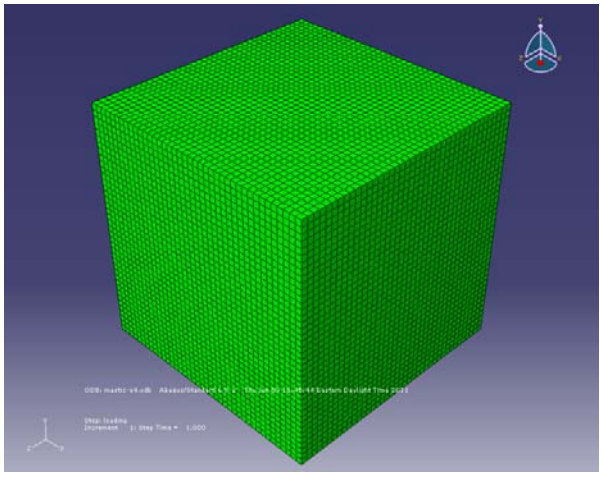

Figure 7-34 Refined mastic model

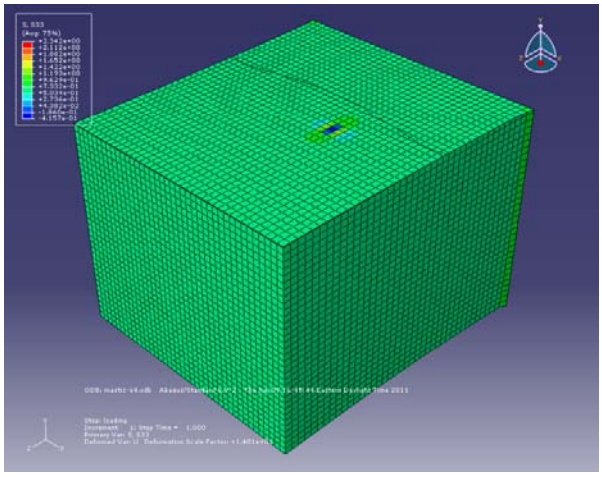

Figure 7-35 Contour of axial stress of the mastic model

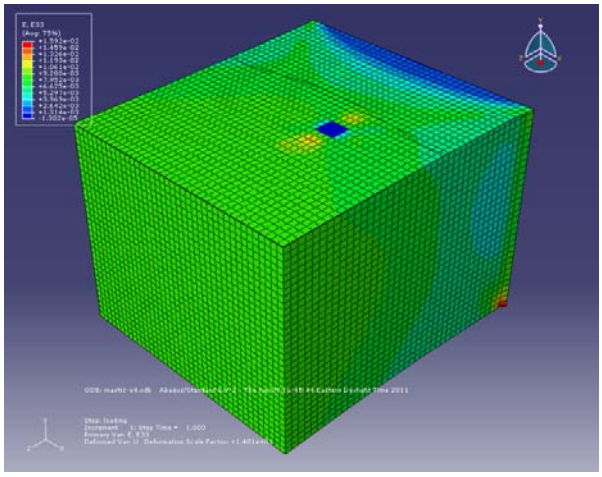

Figure 7-36 Contour of axial strain of the mastic model

In the first fiber-treated mastic model, the fiber is placed in front of the filler along the x direction. The contours of the axial stress and strain are shown in the cut view of model in the Figure 7-37 and Figure 7-38 respectively. The axial stress and strain of the elements in the area A1 and A2 of the model are compared with mastic model. The area A1 is located in front of the filler shown in the Figure 7-39. The area A2 is located behind the filler shown in the Figure 7-40. The axial stress and strain of the elements in the area A1 are shown in the Table 7-40 and Table 7-41. The axial stress and strain of the elements in the area A2 are shown in the Table 7-42 and Table 7-43. It shows that the average axial stress of the elements in A1 area increases 12%. The average axial strain in A1 area decreases 1%. The average axial stress of the elements in A2 increases 2% and the axial strain increases 5%.

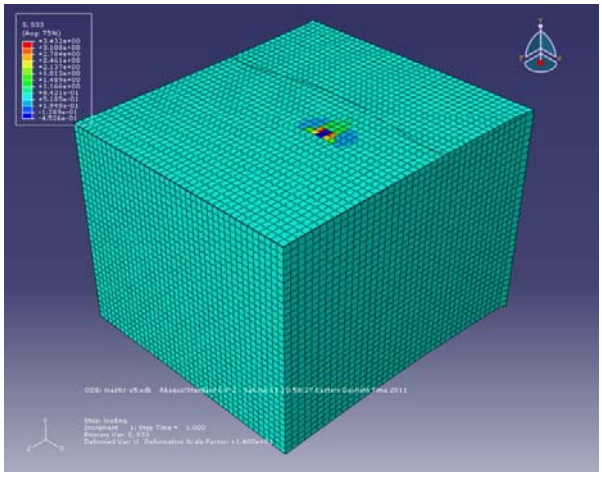

Figure 7-37 Contour of axial stress (fiber in front of the filler)

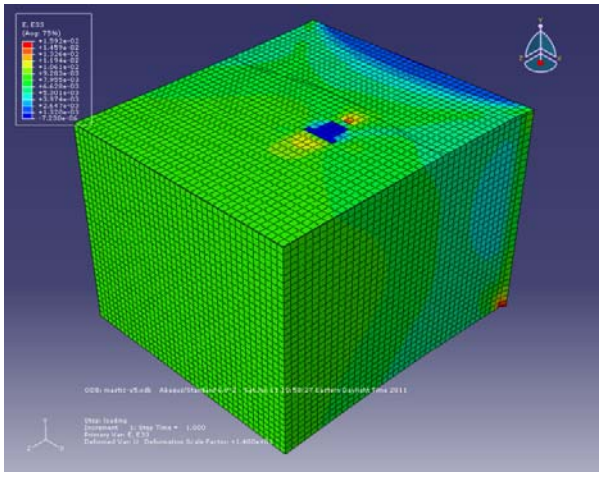

Figure 7-38 Contour of axial strain (fiber in front of the filler)

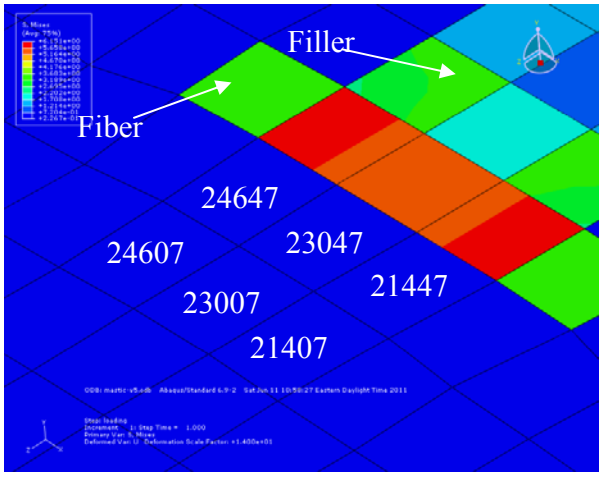

Figure 7-39 Elements in area A1

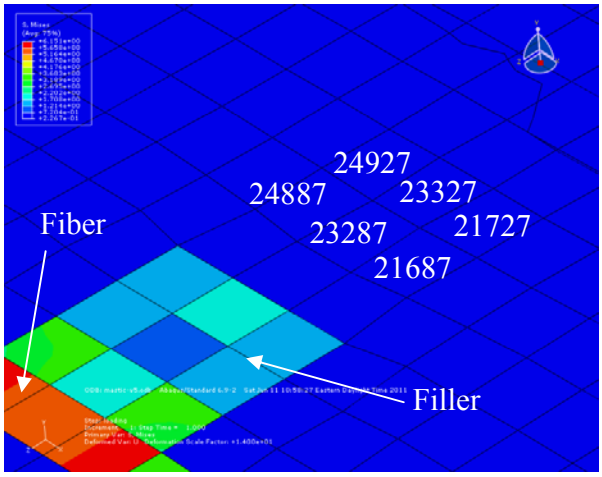

Figure 7-40 Elements in area A2

Table 7-40 Axial stress of the elements in A1 area

Element ID	Mastic model (Mpa)	Fiber-treated mastic model (Mpa)
24607	0.697	0.78
23007	0.679	0.749
21407	0.695	0.779
24647	0.827	0.98
23047	0.970	0.992
21447	0.831	0.981

Table 7-41 Axial strain of the elements in A1 area

Element ID	Mastic model	Fiber-treated mastic model
24607	0.0116	0.0146
23007	0.0137	0.0135
21407	0.0117	0.0144
24647	0.0128	0.0112
23047	0.0147	0.0108
21447	0.0128	0.0112

Table 7-42 Axial stress of the elements in A2 area

Element ID	Mastic model (Mpa)	Fiber-treated mastic model (Mpa)
24887	0.847	0.874
23287	0.985	1.003
21687	0.835	0.862
24927	0.707	0.723
23327	0.688	0.700
21727	0.704	0.721

Table 7-43 Axial strain of the elements in A2 area

Element ID	Mastic model	Fiber-treated mastic model
24887	0.0123	0.0129
23287	0.0139	0.0149
21687	0.0118	0.0125
24927	0.0108	0.0113
23327	0.0126	0.0133
21727	0.0106	0.0111

In the second fiber-treated mastic model, the fiber is placed behind the filler along the x direction. The axial stress and strain of the model are shown in the Figure 7-41 and Figure 7-42 respectively. The axial stress and strain of the elements in the area A1 are shown in the Table 7-44 and Table 7-45. The axial stress and strain of the elements in the area A2 are shown in the Table 7-46 and Table 7-47. Compared with the mastic model, after the fiber is added behind the filler, the axial stress of the elements in area A1 increases 2%; the axial strain of the elements in area A1 increases 5%. The axial stress of the elements in area A2 increases 12%; the axial strain of the elements in area A2 increases 0.5%.

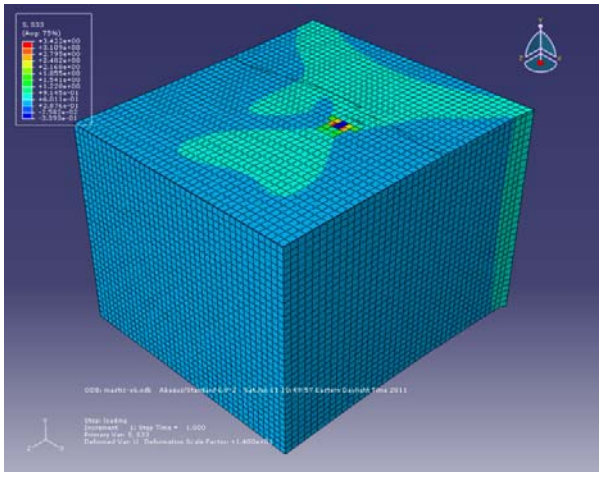

Figure 7-41 Contour of axial stress (fiber behind the filler)

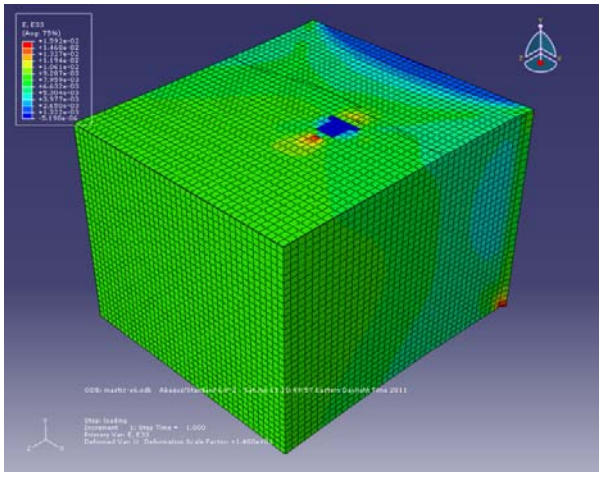

Figure 7-42 Contour of axial strain (fiber behind the filler)

Table 7-44 Axial stress of the elements in A1 area

Element ID	Mastic model (Mpa)	Fiber-treated mastic model (Mpa)
24607	0.697	0.711
23007	0.679	0.689
21407	0.695	0.709
24647	0.827	0.851
23047	0.970	1.004
21447	0.831	0.855

Table 7-45 Axial strain of the elements in A1 area

Element ID	Mastic model	Fiber-treated mastic model
24607	0.0116	0.0122
23007	0.0137	0.0144
21407	0.0117	0.0122
24647	0.0128	0.0135
23047	0.0147	0.0156
21447	0.0128	0.0134

Table 7-46 Axial stress of the elements in A2 area

Element ID	Mastic model (Mpa)	Fiber-treated mastic model (Mpa)
24887	0.847	1.007
23287	0.985	1.010
21687	0.835	0.989
24927	0.707	0.793
23327	0.688	0.762
21727	0.704	0.782

Table 7-47 Axial strain of the elements in A2 area

Element ID	Mastic model	Fiber-treated mastic model
24887	0.0123	0.0109
23287	0.0139	0.0104
21687	0.0118	0.0106
24927	0.0108	0.0135
23327	0.0126	0.0126
21727	0.0106	0.0132

In the third fiber-treated mastic model, the fiber is placed beside the filler along the z direction. The axial stress and strain of the model are shown in the Figure 7-43 and Figure 7-44 respectively. The axial stress and strain of the elements in the area A1 are shown in the Table 7-48 and Table 7-49. The axial stress and strain of the elements in the area A2 are shown in the Table 7-50 and Table 7-51. Compared with the mastic model, after the fiber is added behind the filler, the axial stress of the elements in area A1 increases 3%; the axial strain of the elements in area A1 increases 4%. The axial stress of the elements in area A2 decreases 5%; the axial strain of the elements in area A2 decreases 12%.

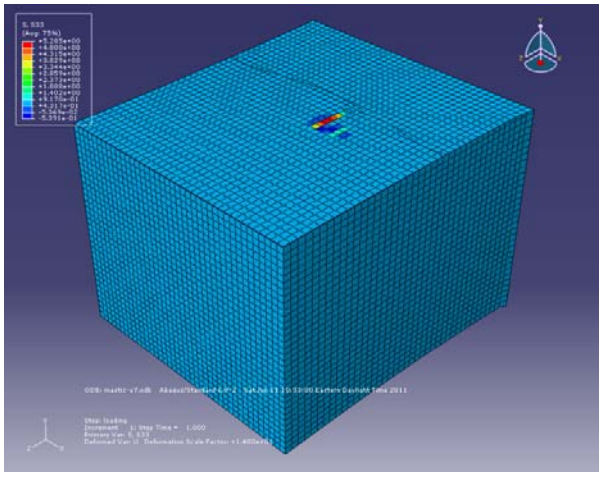

Figure 7-43 Contour of axial stress (Fiber is beside the filler)

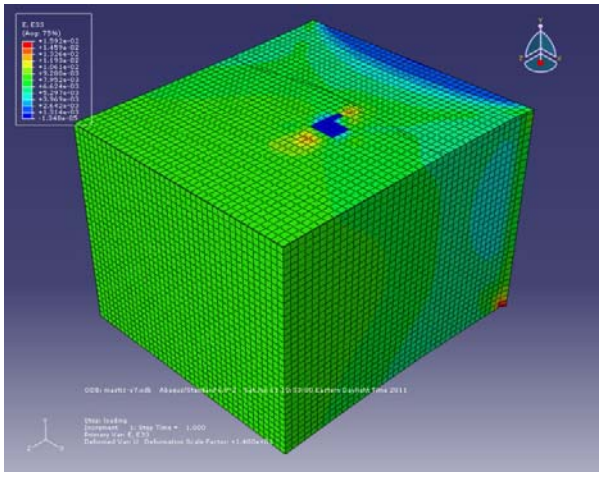

Figure 7-44 Contour of axial strain (fiber is beside the filler)

Table 7-48 Axial stress of the elements in A1 area

Element ID	Mastic model (Mpa)	Fiber-treated mastic model (Mpa)
24607	0.697	0.682
23007	0.679	0.744
21407	0.695	0.676
24647	0.827	0.968
23047	0.970	0.936
21447	0.831	0.854

Table 7-49 Axial strain of the elements in A1 area

Element ID	Mastic model	Fiber-treated mastic model
24607	0.0116	0.0134
23007	0.0137	0.0145
21407	0.0117	0.0112
24647	0.0128	0.0147
23047	0.0147	0.0136
21447	0.0128	0.0126

Table 7-50 Axial stress of the elements in A2 area

Element ID	Mastic model (Mpa)	Fiber-treated mastic model (Mpa)
24887	0.847	0.532
23287	0.985	0.948
21687	0.835	0.770
24927	0.707	0.890
23327	0.688	0.638
21727	0.704	0.681

Table 7-51 Axial strain of the elements in A2 area

Element ID	Mastic model	Fiber-treated mastic model
24887	0.0123	0.0064
23287	0.0139	0.0124
21687	0.0118	0.0113
24927	0.0108	0.0131
23327	0.0126	0.0100
21727	0.0106	0.0093

It can be seen that the placement of the fiber has impacts to the stress and strain distribution around the filler. In three models above, the areas in front of and behind the filler are analyzed when the fiber is placed in three different positions. If the fiber is perpendicular to the loading direction, the addition of the fiber causes increases of the stress and strain around the fiber. If the fiber is placed along the loading direction aside the filler, the stress and strain concentration in front of and behind the filler will be decreased to large extent. So, if the fiber is placed along the loading direction around the filler, it helps the mastic material sustain larger stress and strain level.

Chapter 8. Conclusions

8.1 Overview

The fatigue damage of asphalt concrete is one of the most common distresses that happens on the state highway. The initiation and propagation of the fatigue damage is a complicated phenomenon which is not thoroughly understood. Tremendous research effort is required to completely capture the fatigue process of the asphalt concrete.

Traditional research methods were focused on the fatigue problem of the asphalt mixture. There are a lot of well developed theoretic models and lab test methods to study the fatigue performance of asphalt concrete. However, research of the fatigue of asphalt concrete from micro-scale is not enough. This work provides more understanding about the fatigue of asphalt concrete by investigating the performances of key components of asphalt concrete under cyclic loading. The behavior of asphalt binder, mastic and mixture specimens under cyclic loading is studied.

Currently, the fatigue test methods for asphalt mixture and asphalt binder are different. The repeated flexural bending test is used as the experiment tool to measure the fatigue performance of asphalt mixture, while the fatigue of asphalt binder is estimated by the dynamic shear rheometer (DSR) test. Three major shortcomings are found: 1. The fatigue estimation of asphalt mixture and binding material is not unified; 2. The DSR test used for the fatigue measurement of asphalt binder can provide shear loading only; however, the tensile load is another major source of the fatigue damage; 3. The fatigue of asphalt binder at low temperature cannot be measured by the DSR test. In this study, a self-developed lab test is used to unify the fatigue estimation of

both binding medium and mixture. This test can apply cyclic tensile loading on the specimen and estimate the fatigue performance of asphalt specimen under low temperature. The asphalt binder, mastic and mixture specimens are tested respectively. The effects of loading magnitude, temperature and loading rate to the performance of the asphalt binder under cyclic loading are estimated. The effects of filler content to the performance of mastic specimens are discussed. The differences of performance for mastic and mixture specimen are also analyzed. Finally, the effects of an innovative modifier, basalt fiber, to the performance of asphalt binder and mastic specimens are investigated.

The X-ray tomography imaging technique is utilized to: 1. Obtain the internal structure of the specimen; 2. Provide a tool to analyze the change of internal structure of mastic specimens before and after the fatigue test; 3. Estimate the void content of the mastic and mixture materials. The internal structures of mastic and mixture specimens are reconstructed from a series of 2-D slices of scanned images. The reconstructed internal structures are mapped into the mesh of digital modeling based on FEM. The fatigue test of asphalt binder, mastic and mixture are simulated using the direct cyclic analysis method with damage parameter incorporated to address the damage caused by fatigue loading. The determination of model parameters is described and their effects to the model are discussed. The mesh of the model is refined by using high resolution images; the computational costs are increased and damage parameters need to be adjusted accordingly.

Basalt fibers are dispersed in the binder and mastic specimens to evaluate the effect of the fibers to the performance of the asphalt binder mastic. The fiber-treated asphalt binder and mastic specimens are tested using direct tension test and fatigue test at low temperature. The test results

are compared with test results of asphalt binder and mastic specimens without fiber added. The fiber-treated mastic binder is scanned using x-ray scanner with high resolution. Based on the observation of the scanned image, a FEM model is developed to analyze the influence of the binder and mastic. The fibers are modeled using elastic materials with higher elastic modulus. The effect of the fiber to the axial deformation along the loading direction of the binder is analyzed. An interlocking structure formed by filler and fiber is modeled. The effect of the fiber to the axial stress and strain distribution surrounding the fillers is analyzed. Cyclic loading is applied to the fiber-treated mastic model to analyze the effect of the fiber to the fatigue resistance of the mastic materials. The influence of the position and placement of fiber is discussed in a refined mastic model.

8.2 Major findings

The major findings of the study are shown below:

1. At low temperature, the asphalt binder is easy to break under cyclic loading; even the loading level is lower than the tensile strength. The strain of the specimen keeps increasing as number of loading cycles increases. The magnitude of the cyclic loading is the major factor to determine the final strain and number of loading before a binder specimen fails. The asphalt binder becomes soft as temperature increases; both the strain level and number of loading before a binder specimen fails are increased when temperature is higher. At a low temperature, the impact of loading rate to the performance of asphalt binder is not as significant as loading magnitude and test temperature.

2. The introduction of filler significantly improves the fatigue resistance of asphalt binder. Both the final strain level and number of loading cycles before a mastic specimen fails are much larger than those of the asphalt binder specimen. However, the fatigue resistance of mastic specimen is not linearly increased with the increase of content of filler. A 30% weight ratio between filler and asphalt binder is found to be the optimum content of filler providing longer fatigue resistance.

3. The addition of controlled-size aggregates to the binder can improve the fatigue resistance. However, larger size aggregates added into mastic specimen does not improve the fatigue resistance of the mastic specimen. Based on the image analysis of mastic and mixture specimens, air void content of mixture specimens are much larger than those of mastic specimens. A simple tensile test simulation using FEM shows that strain level of binder and aggregate are very different. Higher air void content and different strain levels between the aggregates and binder are both reasons to initiate the fatigue cracks and accelerate the fatigue propagation.

4. X-ray tomography imaging technique can be used as a tool to analyze the internal structure change of the mastic specimen during the fatigue process. A pixel value variation analysis for the scanning images of mastic specimens before and after fatigue test found that the variation of pixel values of the images after fatigue test is higher than that of the images of specimen before the test.

5. Simulation based on finite element method provides a simple way to describe the fatigue test for asphalt binder, mastic and mixture. With the help of image analysis and processing, the microstructure of the mastic and mixture specimens can be considered in the modeling, in which

the asphalt binder, fillers and aggregates are treated as different materials. The simulation results are improved by considering the micro-structure of the materials. The direct cyclic analysis technique and introduction of damage parameters simplifies the complicated fatigue phenomenon; however, the damage parameters need to be calibrated for different materials.

6. The element number of the model increases when high resolution images are used to reconstruct the internal structure of the model. The high computational cost requires more resources. The damage parameters also need to be adjusted because the number of elements belonging to different components is changed.

7. The basalt fiber increases the break stress of asphalt binder and mastic under direct tensile loading. The direct tension test results of mastic show that the axial strain of the mastic specimen is decreased when fiber is added even the break stress is not much improved. The fatigue test results show that fiber can improve the fatigue resistance significantly for both binder and mastic materials. Simulation of fiber-treated binder and mastic specimens shows that the fibers reduces the axial strain of the binder specimen and reinforce the mastic structure. A fiber placed between two fillers along the loading direction can significantly release the stress and strain concentration between fillers. The fatigue simulation also shows that since the axial strain between fillers is reduced when fiber is added so that fatigue damage in these areas is not easy to initiate. The position and placement analysis of the fiber in the mastic model shows that when the fiber is placed along the loading direction, the effect of the fiber to reduce the stress and strain surrounding the fiber is most significant.

8.3 Recommendations for future research

1. The self-developed fatigue test needs to be further calibrated to find best operation procedure.

2. The parameters of the damage model can be obtained by scanning the specimen during the fatigue test process so that the crack initiation and propagation can be captured. The test data to determine the parameters of the elasto-plastic model is also limited. More tests need to be designed to calibrate the constitutive model of the asphalt binder.

3. The threshold value to determine the air void pixel in a scanned image is not accurate due to the difficulty to determine the real air void content. Tests need to be designed to measure the air void of the small mastic and mixture specimens.

4. The computational costs of fatigue simulation based on FEM are very high if high resolution images are used for mesh generation of the model. A new meshes generation method or mesh refinement techniques need to be studied.

APPENDIX A: TEST BUILDER

The functions of Test Builder used in this work are described below:

Ramp

The ramp function will cause the control channel to ramp to the LEVEL 1 specified, at the RATE specified. (Figure 1). The Absolute and Relative level check boxes determine whether the level specified is relative to the current position, or an absolute level to move to. The Absolute button moves to the specified position from the current position. The Relative button moves the specified Value and Direction from the current position.

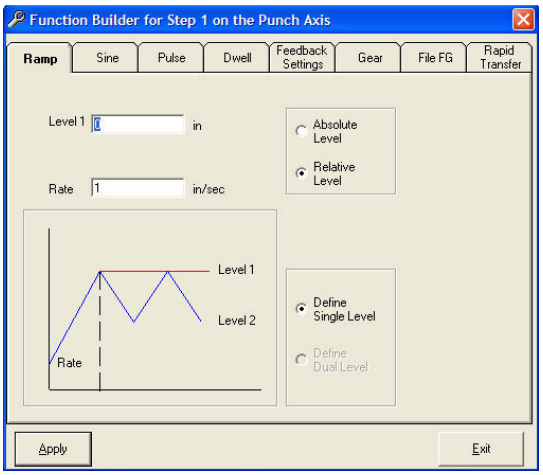

Figure 1 Ramp function of the control channel

Sine function

The sine function –relative will also cause the control channel to move to the LEVEL 1 specified, at the FREQUENCY specified, from the STARTING ANGLE specified. (Figure 2). A starting angle of zero degree will start the sine wave from the position the channel is currently at and

move through an amplitude of the amount specified in LEVEL 1. If a starting angle of 90 degree is input, the current level would be the peak of the sine wave and the valley would be 2 times the amount specified in LEVEL 1, in a negative direction. If a starting angle of -90 degree is input, the current level would be the valley of the sine wave and the peak would be 2 times the amount specified in LEVEL 1, in a positive direction. The number of CYCLES will determine how many times the sequence will be repeated. Cycle always end at 360 degrees, regardless of the starting angle, unless a specific ending angle is specified. If the sine wave continues, zero will be input.

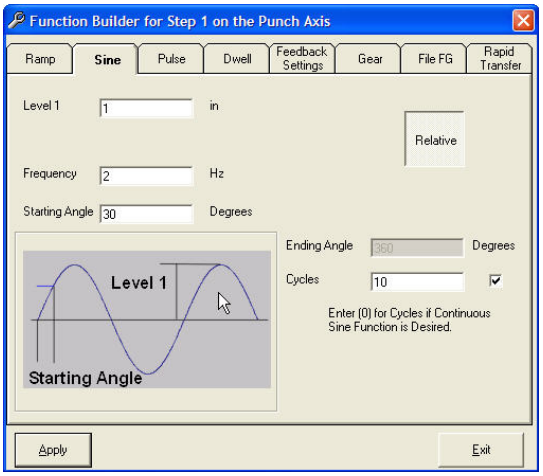

Figure 2 Sine function of the channel control

Dwell Function

The dwell function will cause the control channel to pause at the current level for the amount of time specified in DWELL TIME. (Figure 3) This function is used to make sure the transitions between steps are peacefully built and give users time to input some parameters to continue the test procedure.

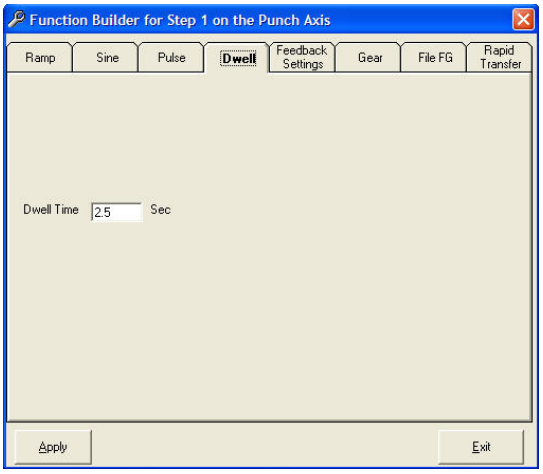

Figure 3 Dwell function of the channel control

Feedback settings

The Feedback settings function changes the control channel feedback to the selected channel. (Figure 4). The channel can either be stroke controlled or loading controlled. The stroke controls the moving distance of the channel which can be considered as displacement or strain controlled. The loading control uses the loading measured at one end of the loading pin as the feedback to control the movement of the channel.

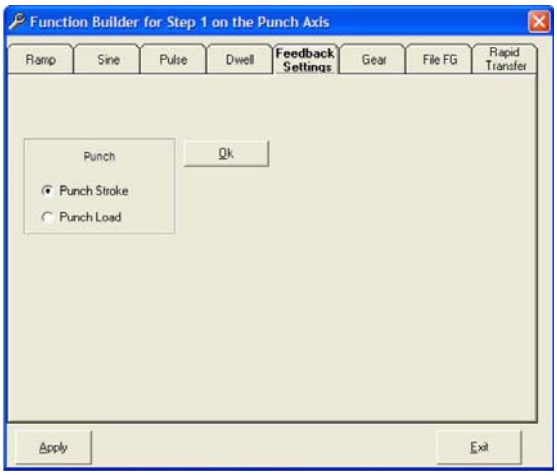

Figure 4 Feedback control of the channel

Define Data Acquisition

Data acquisition of test procedure can be desired at the data acquisition channel column of an existing step. (Figure 5). The Rate (Hz) is the frequency at which the data will be saved which is also known as the number of points per second. The Time (seconds) is the amount of time that the data acquisition will be taken.

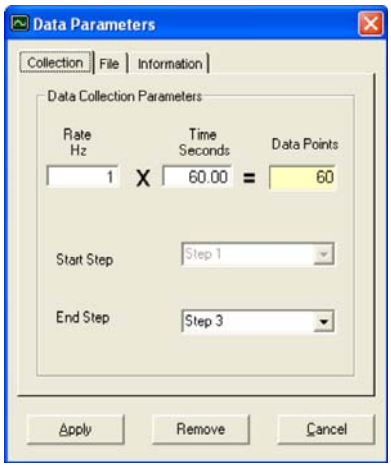

Figure 5 Data acquisition window

Defining Events

The Define Events window (Figure 6) allows several types of events to be defined. Events are used to signify the end of a step. When an event occurs, the channel will move on to the next step in the test sequence.

Level crossing

A channel from the drop down list is selected for the monitor of a level crossing. When the input level is crossed, from either direction, the channel will move on the next step in the test sequence.

Figure 6 Level control of the event

User Input

User input is when the user would like to be prompted during the step that it is specified with. (Figure 7). A small window will appear with the test that was entered and a button that says "PROCEED". The system will not move to the next step until the PROCEED button is pressed. User can also type any message used as a prompt into the message box.

Figure 7 User input control of the event

Axis Done

Axis Done (Figure 8) is used when it is desired to have the channel move on to the next step in the test sequence as soon as the current step function generation is finished. Users can check one channel or any combination if there is more than one.

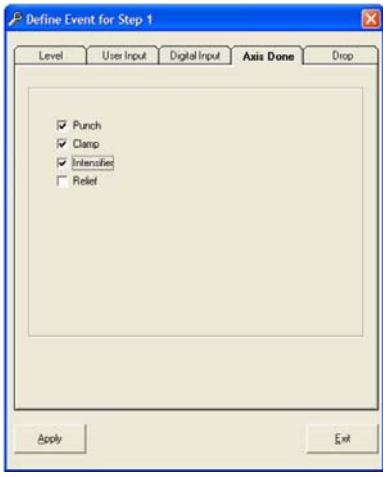

Figure 8 Axis done control of the event

APPENDIX B: MICRO CT 1174 OPERATION PROCEDURE

The steps to operate Micro CT 1174 system are described below:

1. Turn **ON** X-ray scanner from side Green button as shown below. (Figure 9)

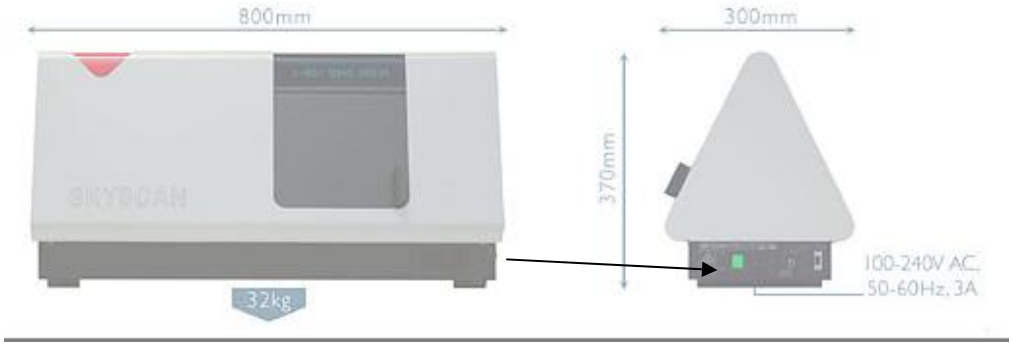

Figure 9 Compact X-ray system

2. Move the switch of the X-ray source to the ON position.

3. Click on SkyScan1174 icon 

on the computer desktop to start the scanning software.

The following window (Figure 10) will appear.

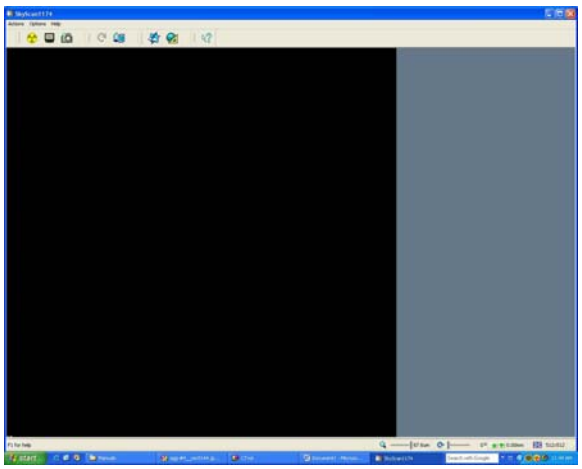

Figure 10 Initialization of the Skyscan system

4. Click on ON/OFF icon  for X-ray aging process. A small window will appear showing the time needed for aging. (Figure 11).

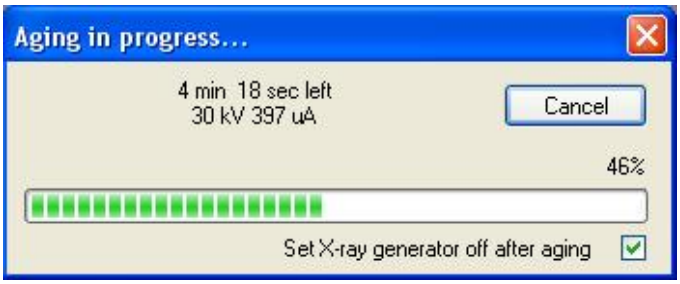

Figure 11 Aging of the system

5. Set the scanning parameters by clicking on the "Options' menu from the menu bar (Figure 12).

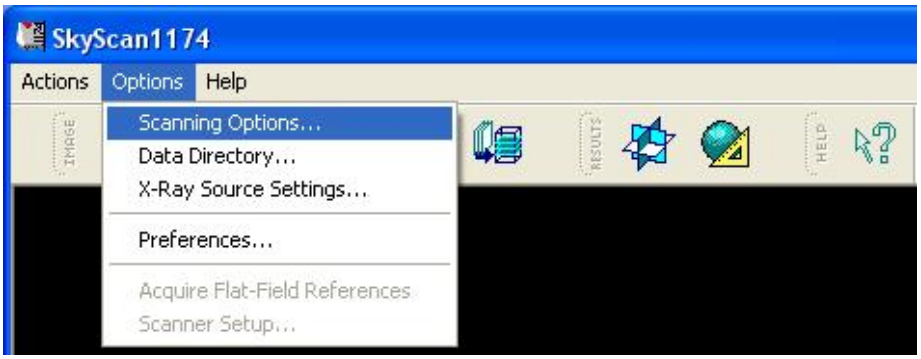

Figure 12 Set up scanning options

By clicking on the "Scanning Option", the following window appears (Figure 13). Users can choose the magnification; data saved path, sample rotation degrees and number of averaging frames to get the results. All scanned images will be saved in a folder created by the user through "Data Directory" under the "Options" menu.

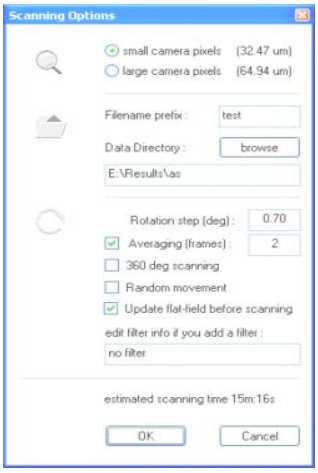

Figure 13 Scanning option parameters

6. After setting up all the parameters, the user can start the Scanning Process by clicking on the Start Scanning  icon in the Toolbar. A small window (Figure 14) will appear showing the scan time left and percent scanned.

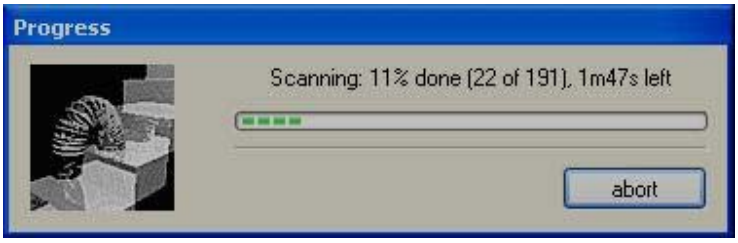

Figure 14 Scanning progress bar

APPENDIX C DIRECT TENSION TEST RESULTS

In the chapter 4, asphalt binder PG70-22 is tested using direct tension test. The stress and strain data of direct tension test for each specimen are listed below.

Table 1 Stress and strain of asphalt binder specimens in direct tension test

	Specimen #1		Specimen #2		Specimen #3	
Time	Tensile Strain	Tensile Stress (Mpa)	Tensile Strain	Tensile Stress (Mpa)	Tensile Strain	Tensile Stress (Mpa)
0	0	0	0	0	0	0
0.1	0.003	0.044	0.003	0.044	0.003	0.039
0.2	0.006	0.064	0.009	0.069	0.009	0.075
0.3	0.012	0.083	0.012	0.097	0.012	0.1
0.4	0.018	0.106	0.018	0.119	0.018	0.119
0.5	0.021	0.131	0.021	0.139	0.024	0.153
0.6	0.027	0.153	0.027	0.164	0.027	0.183
0.7	0.033	0.178	0.033	0.178	0.033	0.197
0.8	0.038	0.197	0.038	0.203	0.038	0.225
0.9	0.041	0.222	0.041	0.222	0.041	0.244
1	0.044	0.239	0.047	0.247	0.044	0.267
1.1	0.05	0.261	0.05	0.261	0.05	0.289
1.2	0.056	0.283	0.056	0.275	0.056	0.311
1.3	0.062	0.306	0.059	0.308	0.059	0.339
1.4	0.062	0.325	0.065	0.319	0.065	0.356
1.5	0.068	0.356	0.068	0.333	0.068	0.381
1.6	0.074	0.372	0.074	0.361	0.074	0.403
1.7	0.077	0.394	0.077	0.375	0.08	0.417
1.8	0.083	0.411	0.083	0.392	0.083	0.444
1.9	0.089	0.436	0.089	0.406	0.089	0.461
2	0.092	0.45	0.092	0.433	0.092	0.475
2.1	0.095	0.472	0.098	0.447	0.098	0.497
2.2	0.101	0.483	0.104	0.464	0.101	0.514
2.3	0.107	0.506	0.107	0.483	0.107	0.533
2.4	0.109	0.522	0.112	0.494	0.109	0.553
2.5	0.115	0.544	0.115	0.514	0.115	0.575
2.6	0.121	0.564	0.121	0.531	0.121	0.597
2.7	0.124	0.581	0.127	0.544	0.124	0.608
2.8	0.13	0.6	0.13	0.558	0.13	0.633

2.9	0.133	0.625	0.133	0.578	0.133	0.65
3	0.139	0.639	0.139	0.592	0.139	0.669
3.1	0.145	0.656	0.142	0.608		
3.2	0.148	0.672	0.148	0.625		
3.3	0.154	0.692	0.154	0.636		
3.4	0.157	0.703	0.157	0.65		
3.5	0.163	0.719	0.166	0.667		
3.6	0.166	0.742	0.169	0.681		
3.7	0.172	0.756				
3.8	0.178	0.772				
3.9	0.18	0.786				
4	0.186	0.811				
4.1	0.189	0.819				
Maximum Tensile loading (N)	29.48		24.52		24.08	
Average (N)	26.03					

In the chapter 7, four kinds of materials are tested using direct tension test. The stress and strain data of direct tension test for each specimen are listed below.

Table 2 Stress and strain of asphalt binder in direct tension test

Binder specimen #1			Binder specimen #2			Binder specimen #3		
Time	Strain	Stress	Time	Strain	Stress	Time	Strain	Stress
0	0	0	0	0	0	0	0	0
0.1	0.007	0.056	0.1	0.007	0.067	0.1	0.005	0.044
0.2	0.012	0.075	0.2	0.012	0.086	0.2	0.01	0.069
0.3	0.017	0.086	0.3	0.017	0.103	0.3	0.012	0.094
0.4	0.022	0.103	0.4	0.022	0.119	0.4	0.02	0.125
0.5	0.027	0.108	0.5	0.025	0.142	0.5	0.022	0.153
0.6	0.032	0.128	0.6	0.03	0.158	0.6	0.03	0.178
0.7	0.037	0.147	0.7	0.035	0.178	0.7	0.032	0.206
0.8	0.042	0.17	0.8	0.04	0.197	0.8	0.037	0.233
0.9	0.047	0.189	0.9	0.045	0.22	0.9	0.042	0.264
1	0.05	0.217	1	0.05	0.242	1	0.047	0.292
1.1	0.055	0.245	1.1	0.055	0.264	1.1	0.05	0.328
1.2	0.06	0.275	1.2	0.062	0.292	1.2	0.055	0.353
1.3	0.065	0.306	1.3	0.062	0.314	1.3	0.06	0.384
1.4	0.07	0.328	1.4	0.067	0.339	1.4	0.065	0.417
1.5	0.072	0.35	1.5	0.072	0.364	1.5	0.07	0.442
1.6	0.077	0.389	1.6	0.077	0.384	1.6	0.075	0.473
1.7	0.085	0.423	1.7	0.08	0.406	1.7	0.08	0.503
1.8	0.087	0.45	1.8	0.087	0.439	1.8	0.082	0.528
1.9	0.092	0.481	1.9	0.092	0.456	1.9	0.087	0.559
2	0.097	0.512	2	0.097	0.487	2	0.092	0.584
2.1	0.102	0.545	2.1	0.102	0.514	2.1	0.097	0.609
2.2	0.107	0.57	2.2	0.107	0.537	2.2	0.102	0.637
2.3	0.11	0.601	2.3	0.11	0.565	2.3	0.107	0.665
2.4	0.115	0.628	2.4	0.115	0.587	2.4	0.112	0.692
2.5	0.12	0.659	2.5	0.12	0.612	2.5	0.117	0.729
2.6	0.125	0.687	2.6	0.125	0.637	2.6	0.12	0.748
2.7	0.13	0.718	2.7	0.13	0.67	2.7	0.125	0.773
2.8	0.132	0.745	2.8	0.135	0.693	2.8	0.13	0.798
2.9	0.14	0.768	2.9	0.137	0.718	2.9	0.135	0.823
3	0.142	0.798	3	0.142	0.746	3	0.14	0.848
3.1	0.147	0.835	3.1	0.147	0.762	3.1	0.145	0.879

3.2	0.152	0.857	3.2	0.152	0.79	3.2	0.147	0.904
3.3	0.157	0.882	3.3	0.157	0.821			
			3.4	0.16	0.84			
			3.5	0.165	0.865			

Table 3 Stress and strain of fiber-treated asphalt binder in direct tension test

Specimen #1			Specimen #2			Specimen #3		
Time	Strain	Stress	Time	Strain	Stress	Time	Strain	Stress
0	0	0	0	0	0	0	0	0
0.1	0.005	0.058	0.1	0.007	0.044	0.1	0.005	0.047
0.2	0.01	0.086	0.2	0.01	0.058	0.2	0.01	0.086
0.3	0.015	0.122	0.3	0.017	0.078	0.3	0.015	0.114
0.4	0.02	0.147	0.4	0.02	0.083	0.4	0.022	0.142
0.5	0.025	0.172	0.5	0.025	0.103	0.5	0.025	0.169
0.6	0.03	0.206	0.6	0.03	0.122	0.6	0.03	0.195
0.7	0.035	0.233	0.7	0.035	0.147	0.7	0.032	0.222
0.8	0.037	0.258	0.8	0.037	0.175	0.8	0.037	0.261
0.9	0.042	0.283	0.9	0.042	0.2	0.9	0.042	0.281
1	0.047	0.306	1	0.047	0.228	1	0.047	0.311
1.1	0.052	0.334	1.1	0.052	0.25	1.1	0.052	0.339
1.2	0.057	0.356	1.2	0.057	0.283	1.2	0.057	0.359
1.3	0.062	0.384	1.3	0.062	0.309	1.3	0.062	0.392
1.4	0.067	0.411	1.4	0.065	0.339	1.4	0.067	0.417
1.5	0.07	0.439	1.5	0.072	0.364	1.5	0.07	0.442
1.6	0.075	0.467	1.6	0.075	0.389	1.6	0.075	0.473
1.7	0.08	0.492	1.7	0.082	0.42	1.7	0.08	0.498
1.8	0.082	0.514	1.8	0.087	0.448	1.8	0.085	0.525
1.9	0.09	0.542	1.9	0.09	0.475	1.9	0.09	0.55
2	0.095	0.573	2	0.095	0.5	2	0.095	0.578
2.1	0.097	0.595	2.1	0.1	0.528	2.1	0.1	0.603
2.2	0.102	0.623	2.2	0.102	0.551	2.2	0.102	0.631
2.3	0.107	0.659	2.3	0.107	0.573	2.3	0.107	0.656
2.4	0.112	0.673	2.4	0.115	0.603	2.4	0.112	0.684
2.5	0.117	0.695	2.5	0.117	0.626	2.5	0.117	0.706
2.6	0.122	0.723	2.6	0.122	0.651	2.6	0.12	0.729
2.7	0.125	0.754	2.7	0.127	0.676	2.7	0.125	0.757
2.8	0.132	0.784	2.8	0.132	0.701	2.8	0.13	0.782
2.9	0.135	0.804	2.9	0.137	0.723	2.9	0.135	0.807
3	0.14	0.826	3	0.14	0.754	3	0.14	0.832
3.1	0.145	0.86	3.1	0.145	0.782	3.1	0.145	0.86
3.2	0.15	0.882	3.2	0.15	0.807	3.2	0.15	0.885
3.3	0.152	0.918	3.3	0.155	0.835	3.3	0.155	0.904
3.4	0.157	0.938	3.4	0.16	0.86	3.4	0.16	0.932
3.5	0.162	0.965	3.5	0.165	0.882			

3.6	0.167	0.988	3.6	0.167	0.907			
3.7	0.172	1.013	3.7	0.175	0.929			
3.8	0.177	1.041	3.8	0.177	0.957			
3.9	0.182	1.066	3.9	0.182	0.985			
4	0.185	1.091	4	0.187	1.007			
			4.1	0.192	1.035			
			4.2	0.197	1.06			
			4.3	0.202	1.083			
			4.4	0.207	1.108			
			4.5	0.21	1.127			

Table 4 Stress and strain of mastic in direct tension test

Specimen #1			Specimen #2			Specimen #3		
Time	Strain	Stress	Time	Strain	Stress	Time	Strain	Stress
0	0	0	0	0	0	0	0	0
0.1	0.005	0.05	0.1	0.005	0.05	0.1	0.002	0.042
0.2	0.01	0.072	0.2	0.01	0.078	0.2	0.01	0.069
0.3	0.012	0.083	0.3	0.015	0.089	0.3	0.012	0.089
0.4	0.02	0.089	0.4	0.017	0.103	0.4	0.017	0.108
0.5	0.022	0.103	0.5	0.025	0.128	0.5	0.022	0.133
0.6	0.03	0.103	0.6	0.03	0.142	0.6	0.027	0.156
0.7	0.035	0.114	0.7	0.035	0.164	0.7	0.032	0.186
0.8	0.04	0.122	0.8	0.037	0.183	0.8	0.037	0.208
0.9	0.042	0.133	0.9	0.042	0.203	0.9	0.042	0.242
1	0.047	0.153	1	0.047	0.225	1	0.047	0.267
1.1	0.052	0.17	1.1	0.052	0.256	1.1	0.05	0.292
1.2	0.057	0.195	1.2	0.057	0.278	1.2	0.055	0.32
1.3	0.062	0.22	1.3	0.062	0.3	1.3	0.062	0.353
1.4	0.067	0.245	1.4	0.067	0.322	1.4	0.065	0.372
1.5	0.072	0.264	1.5	0.07	0.345	1.5	0.07	0.406
1.6	0.075	0.286	1.6	0.075	0.381	1.6	0.075	0.436
1.7	0.082	0.306	1.7	0.08	0.409	1.7	0.08	0.467
1.8	0.085	0.328	1.8	0.085	0.434	1.8	0.082	0.498
1.9	0.09	0.35	1.9	0.09	0.464	1.9	0.087	0.525
2	0.095	0.361	2	0.095	0.495	2	0.095	0.551
2.1	0.1	0.386	2.1	0.1	0.528	2.1	0.097	0.578
2.2	0.105	0.42	2.2	0.102	0.553	2.2	0.102	0.603
2.3	0.107	0.45	2.3	0.107	0.581	2.3	0.107	0.634
2.4	0.112	0.481	2.4	0.112	0.615	2.4	0.112	0.654
2.5	0.12	0.52	2.5	0.117	0.642	2.5	0.115	0.687
2.6	0.122	0.545	2.6	0.12	0.67	2.6	0.12	0.715
2.7	0.127	0.584	2.7	0.125	0.709	2.7	0.125	0.751
2.8	0.132	0.606	2.8	0.132	0.734	2.8	0.13	0.779
2.9	0.137	0.64	2.9	0.135	0.773	2.9	0.135	0.807
3	0.14	0.665	3	0.14	0.804	3	0.14	0.835
3.1	0.145	0.701	3.1	0.145	0.837	3.1	0.142	0.857
3.2	0.15	0.729	3.2	0.15	0.865	3.2	0.147	0.89
3.3	0.155	0.76	3.3	0.152	0.893	3.3	0.152	0.915
3.4	0.16	0.796	3.4	0.157	0.929	3.4	0.157	0.946
3.5	0.165	0.821	3.5	0.162	0.96	3.5	0.162	0.971

3.6	0.17	0.854	3.6	0.167	0.999	3.6	0.165	1.002
3.7	0.172	0.885	3.7	0.172	1.03	3.7	0.17	1.035
3.8	0.177	0.907	3.8	0.175	1.066	3.8	0.175	1.06
3.9	0.182	0.932	3.9	0.18	1.102	3.9	0.18	1.091
4	0.187	0.96	4	0.185	1.13	4	0.185	1.108
4.1	0.19	0.991	4.1	0.19	1.169	4.1	0.19	1.138
4.2	0.197	1.021	4.2	0.195	1.197	4.2	0.195	1.166
4.3	0.2	1.049	4.3	0.2	1.23	4.3	0.2	1.188
4.4	0.205	1.086	4.4	0.202	1.266	4.4	0.202	1.214
4.5	0.21	1.105	4.5	0.207	1.297	4.5	0.21	1.247
4.6	0.215	1.133				4.6	0.212	1.272
4.7	0.22	1.161						
4.8	0.222	1.186						
4.9	0.23	1.211						

Table 5 Stress and strain of fiber-treated mastic in direct tension test

Time	Strain	Stress	Time	Strain	Stress	Time	Strain	Stress
0	0	0	0	0	0	0	0	0
0.1	0.005	0.047	0.1	0.005	0.031	0.1	0.002	0.058
0.2	0.01	0.092	0.2	0.012	0.036	0.2	0.01	0.1
0.3	0.012	0.133	0.3	0.015	0.044	0.3	0.015	0.131
0.4	0.017	0.164	0.4	0.02	0.042	0.4	0.02	0.167
0.5	0.022	0.2	0.5	0.027	0.047	0.5	0.022	0.203
0.6	0.027	0.233	0.6	0.03	0.053	0.6	0.027	0.242
0.7	0.032	0.261	0.7	0.035	0.05	0.7	0.032	0.289
0.8	0.037	0.297	0.8	0.04	0.058	0.8	0.037	0.32
0.9	0.04	0.328	0.9	0.045	0.064	0.9	0.042	0.37
1	0.045	0.37	1	0.05	0.072	1	0.045	0.406
1.1	0.05	0.395	1.1	0.055	0.075	1.1	0.05	0.442
1.2	0.055	0.431	1.2	0.06	0.086	1.2	0.055	0.492
1.3	0.057	0.464	1.3	0.065	0.089	1.3	0.06	0.52
1.4	0.065	0.498	1.4	0.072	0.103	1.4	0.062	0.559
1.5	0.067	0.531	1.5	0.075	0.111	1.5	0.067	0.609
1.6	0.072	0.564	1.6	0.08	0.122	1.6	0.072	0.642
1.7	0.077	0.589	1.7	0.085	0.142	1.7	0.077	0.687
1.8	0.082	0.628	1.8	0.09	0.158	1.8	0.082	0.723
1.9	0.085	0.648	1.9	0.092	0.175	1.9	0.087	0.759
2	0.09	0.681	2	0.097	0.192	2	0.09	0.792
2.1	0.095	0.717	2.1	0.102	0.211	2.1	0.095	0.831
2.2	0.1	0.748	2.2	0.107	0.234	2.2	0.097	0.87
2.3	0.102	0.773	2.3	0.112	0.256	2.3	0.105	0.909
2.4	0.11	0.806	2.4	0.117	0.284	2.4	0.11	0.945
2.5	0.112	0.843	2.5	0.12	0.303	2.5	0.112	0.982
2.6	0.12	0.862	2.6	0.127	0.328	2.6	0.117	1.018
2.7	0.122	0.884	2.7	0.132	0.348	2.7	0.122	1.057
2.8	0.127	0.918	2.8	0.137	0.37	2.8	0.127	1.099
2.9	0.132	0.957	2.9	0.14	0.395	2.9	0.13	1.124
3	0.14	0.99	3	0.145	0.414	3	0.137	1.165
3.1	0.142	1.004	3.1	0.15	0.445	3.1	0.14	1.196
3.2	0.147	1.038	3.2	0.155	0.47	3.2	0.145	1.232
3.3	0.152	1.071	3.3	0.16	0.492	3.3	0.15	1.271
3.4	0.157	1.105	3.4	0.165	0.518	3.4	0.155	1.308
3.5	0.16	1.127	3.5	0.17	0.545	3.5	0.157	1.341
3.6	0.165	1.155	3.6	0.172	0.57	3.6	0.162	1.374

			3.7	0.177	0.595	3.7	0.167	1.413
			3.8	0.182	0.623	3.8	0.172	1.444
			3.9	0.185	0.643	3.9	0.177	1.472
			4	0.19	0.671			
			4.1	0.197	0.699			
			4.2	0.2	0.721			
			4.3	0.205	0.749			
			4.4	0.21	0.771			
			4.5	0.215	0.799			
			4.6	0.22	0.824			
			4.7	0.225	0.849			
			4.8	0.23	0.874			
			4.9	0.232	0.894			
			5	0.237	0.924			
			5.1	0.242	0.944			
			5.2	0.247	0.966			
			5.3	0.252	0.997			
			5.4	0.257	1.019			
			5.5	0.26	1.044			
			5.6	0.265	1.069			
			5.7	0.272	1.092			
			5.8	0.277	1.114			

REFERENCES

[1] "http://training.ce.washington.edu/PGI/."

[2] AASHTO (2008). "Determining the Fatigue Life of Compacted Hot-Mix Asphalt (HMA) Subjected to Repeated Flexural Bending." *Annual Book of ASTM standards*, T321-03.

[3] Abdulshafi, A. A., and Majidzadeh, K. (1985). "J-integral and cyclic Plasticity Approach to Fatigue and Fracture of asphaltic Mixtures." *Transportation Research Record*(1034), 112-123.

[4] Aglan, H. A., and Figueroa, J. L. (1993). "Damage-evolution approach to fatigue cracking in pavements " *Journal of Engineering Mechanics*, 19, 1243-1259.

[5] Bay, B., Smith, T., Fyhrie, D., and Saad, M. (1999). "Digital volume correlation: Three-dimensional strain mapping using X-ray tomography." *Experimental Mechanics*, 39(3), 217-226.

[6] Bodin, D., Pijaudier-Cabot, G., De La Roche, C., Piau, J.-M., and Chabot, A. (2004). "Continuum damage approach to asphalt concrete fatigue modeling." *Journal of Engineering Mechanics*, 130(6), 700-709.

[7] Bonnetti, K. S., Nam, K., and Bahia, H. U. (2002). "Measuring and defining fatigue behavior of asphalt binders." *Transportation Research Record*(1810), 33-43.

[8] Botev, M., Betchev, H., Bikiaris, D., and Panayiotou, C. (1999). "Mechanical properties and viscoelastic behavior of basalt fiber-reinforced polypropylene." *Journal of Applied Polymer Science*, 74(3), 523-531.

[9] Boussad, N., DesCroix, P., and Dony, A. (1996). "Prediction of mix modulus and fatigue Law from binder rheology properties." *Association of Asphalt Paving Technologist*, 65, 4065.

[10] Brik, V. (1999). "Advanced concept concrete using basalt fiber composite reinforcement." *Tech Res Rpeort submitted to NCHRP-IDEA, project 45*.

[11] Button, J. W., Little, D. N., Kim, Y., and Ahmed, J. (1987). "Mechanistic Evaluation of Selected Asphalt additives." *The Association of Asphalt Paving Technologists*, 56, 62-90.

[12] Carpenter, S. H., and Shen, S. (2006). "Dissipated Energy Approach to Study Hot-Mix Asphalt Healing in Fatigue." *Transportation Research Record: Journal of the Transportation Research Board*(1970), 178-185.

[13] Castro, M., and Sanchez, J. A. (2007). "Damage Based Model for Prediction of Asphalt Concrete Fatigue Curves." *Journal of Materials in Civil Engineering*, 19(8), 700-702.

[14] Chehab, G. R., Seo, Y., and Kim, Y. R. (2007). "Viscoelastoplastic Damage Characterization of Asphalt--Aggregate Mixtures Using Digital Image Correlation." *International Journal of Geomechanics*, 7(2), 111-118.

[15] Dai, Q. (2010). "Prediction of Dynamic Modulus and Phase Angle of Stone-Based Composites Using a Micromechanical Finite-Element Approach." *Journal of materials in civil engineering* 22(6), 618-627.

[16] Dai, Q., Sadd, M. H., Parameswaran, V., and Shukla4, A. (2005). "Prediction of Damage Behaviors in Asphalt Materials Using a Micromechanical Finite-Element Model and Image Analysis." *Journal of Engineering Mechanics*, 131(7).

[17] Daniel, J. S., and Bisirri, W. M. "Characterizing fatigue in pavement materials using a dissipated energy parameter."

[18] Daniel, J. S., and Bisirri, W. M. "Characterizing fatigue in pavement materials using a dissipated energy parameter." American Society of Civil Engineers, 199-208.

[19] Darveaux, R. (2000). "Effect of Simulation Methodology on Solder Joint Crack Growth Correlation." *Proceedings of Electronic Components and Technology Conference*, 1048-1058.

[20] Deacon, J. A., Harvey, J. T., Tayebali, A., and Monismith, C. L. (1997). "Influence of Binder Loss Modulus on Pavement Fatigue Performance of Asphalt concrete pavement." *Journal of the Association of Asphalt Paving Technologists*, 66, 633-685.

[21] El-Basyouny, M. M., and Witczak, M. (2005). "Calibration of Alligator Fatigue Cracking Model for 2002 Design Guide." *Transportation Research Record: Journal of the Transportation Research Board*(1919), 77-86.

[22] Epps, J., and Monismith, C. L. (1969). "Influence of mixture variables on the flexural fatigue properties of asphalt concrete." *Asphalt Paving Technology*, 38, 423-464.

[23] Ghuzlan, K. A., and Carpenter, S. H. (2002). "Traditional Fatigue Analysis of Asphalt Concrete Mixtures." *Transportation Research Record: Journal of the Transportation Research Board*.

[24] Ghuzlan, K. A., and Carpenter, S. H. (2006). "Fatigue damage analysis in asphalt concrete mixtures using the dissipated energy approach." *Canadian Journal of Civil Engineering*, 33, 890-901.

[25] Harvey, J., and Tsai, B.-W. (1996). "Effects of Asphalt Content and Air Void Content on Mix Fatigue and Stiffness." *Transportation Research Record: Journal of the Transportation Research Board*, 1543(-1), 38-45.

[26] Huang, C., Najjar, Y. M., and Romanoschi, S. (2006). "Predicting the Asphalt Concrete Fatigue Life Using Artificial Neural Network Approach."

[27] Kandhal, P. S., Lynn, C. Y., and Frazier Parker, J. (2007). "Characterization tests for mineral fillers related to performance of asphalt paving mixtures." *Transportation Research Board*, 1638, 101-110.

[28] Kim, Y.-R., Allen, D., and Little, D. (2006). "Computational Model to Predict Fatigue Damage Behavior of Asphalt Mixtures Under Cyclic Loading." *Transportation Research Record: Journal of the Transportation Research Board*, 1970(-1), 196-206.

[29] Kim, Y.-R., Allen, D. H., and Little, D. N. (2007). "Computational constitutive model for predicting nonlinear viscoelastic damage and fracture failure of asphalt concrete mixtures." *International Journal of Geomechanics*, 7(2), 102-110.

[30] Kim, Y.-R., Little, D., and Song, I. (2003). "Effect of Mineral Fillers on Fatigue Resistance and Fundamental Material Characteristics: Mechanistic Evaluation." *Transportation Research Record*, 1832, 1-8.

[31] Kim, Y.-R., and Lutif, J. S. "Computational Micromechanics Modeling for Damage-Induced Behavior of Asphalt Mixtures Considering Viscoelasticity and Cohesive Zone Fracture." ASCE, 2-2.

[32] Lau, J. H., Pan, S. H., and Chang, C. (2002). "A New Thermal-Fatigue Life Prediction Model for Wafer Level Chip Scale Package (WLCSP) Solder Joints." *ASME*, 124, 212-220.

[33] Lee, H.-J., Daniel, J. S., and Kim, Y. R. (2000). "Continuum damage mechanics-based fatigue model of asphalt concrete." *Journal of Materials in Civil Engineering*, 12(2), 105-112.

[34] Lemaitre, J., and Chaboche, J.-L. (1990). "Mechanics of Solid Materials." *Cambridge University Press*.

[35] Ludovico, M. D., Prota, A., and Manfredi, G. (2010). "Structural upgrade using basalt fibers for concrete confinement." *Journal of composites for construction*, 541-552.

[36] Lundstrom, R. (2004). "On rheological testing and modelling of asphalt mixtures with emphasis on fatigue characterisation." *Doctoral thesis*.

[37] Majidzadeh, K., Kauffman, E. M., and Saraf, C. L. (1972). "Analysis of Fatigue of Paving Mixtures from Fracture Mechanics Viewpoint." *American Society for Testing and Materials (ASTM STP 508)*, 67-83.

[38] Martono, W., Bahia, H. U., and Angelo, J. D. (2007). "Effect of Testing Geometry on Measuring Fatigue of Asphalt Binders and Mastics." *Journal of Materials in Civil Engineering*, 19(19).

[39] Matthys, S., Taerwe, L., and Audenaert, K. (1999). "Tests on axially loaded concrete columns confined by fiber reinforced polymer sheet wrapping." *Proc., FRPRCS-4, Baltimore, American Concrete Institute, 1182*.

[40] Monismith, C. L., Epps, J. A., Kasianchuk, D. A., and Mclean, D. B. (1971). "Asphalt Mixture Behavior in Repeated Flexure." *Report TE 79-5 University of California, Berkeley, 1971*.

[41] Mull, M. A., Stuart, K., and Yehia, A. (2002). "Fracture Resistance Characterization of Chemically Modified Crumb Rubber Asphalt Pavement." *Journal of Material Science*, 37, 557-566.

[42] Papagiannakis, A. T., Abbas, A., and Masad, E. (2002). "Micromechanical analysis of viscoelastic properties of asphalt concretes." *Transportation Research Record.*, 1789, 113-120.

[43] Pronk, A. C. (1997). "Evaluation of the dissipated energy concept for the interpretation of fatigue measurements in the Crack Initiation Phase." *Ministerie van Verkeer en Waterstaat*(W-DWW-97-056).

[44] Ramakrishnan, V., Tolmare, N. S., and Brik, V. B. (1998). "Performance Evaluation of 3-D Basalt Fiber Reinforced Concrete & Basalt Rod Reinforced Concrete." *Final Report for Highway IDEA Project 45*.

[45] Ramsamooj, D. V. (1999). "Prediction of Fatigue Performance of Asphalt Concrete Mixes." *Journal of Testing and Evaluation*, 27(5), 3343-3348.

[46] Ramsamooj, D. V. (2002). "Analytical Model for Prediction of Fatigue Life of Asphalt Concrete, Including Size Effect." *International Journal of Pavement Engineering* 3(3), 161-171.

[47] Rodrigues, R. M. (1999). "A Model for Fatigue Cracking Prediction of Asphalt Pavements Based on Mixture Bonding Energy." *International Journal of Pavement Engineering* 1(2), 133-149.

[48] Scheffy, C. (1999). "Asphalt Concrete Fatigue Crack Monitoring and Analysis Using Digital Image Analysis Techniques." *Accelerated Pavement Testing 1999 International Conference*.

[49] Shatnawi, S. R. (1997). "Fatigue performance of asphalt concrete mixes using a new repetitive direct tension test."

[50] Shen, S., Chiu, H.-M., and Huang, H. (2010). "Characterization of Fatigue and Healing in Asphalt Binders." *Journal of Materials in Civil Engineering*, 22(9), 846-852.

[51] Shenoy, A. (2002). "Fatigue testing and evaluation of asphalt binders using the dynamic shear rheometer." *Journal of Testing and Evaluation*, 30(4), 303-312.

[52] Si, Z., Little, D. N., and Lytton, R. L. (2002). "Characterization of microdamage and healing of asphalt concrete mixtures." *Journal of Materials in Civil Engineering*, 14(6), 461-470.

[53] Sim, J., Park, C., and Moon, D. Y. (2005). "Characteristics of basalt fiber as a strengthening material for concrete structures." *Composites Part B: Engineering*, 36(6-7), 504-512.

[54] SIMULIA "ABAQUS Manual 6.9."

[55] Smith, B., and Hesp, S. (2000). "Crack Pinning in Asphalt Mastic and Concrete: Regular Fatigue Studies." *Transportation Research Record*, 1728(-1), 75-81.

[56] Sousa, J. B., Pais, J. C., Prates, M., Barros, R., Langlois, P., and Leclerc, A.-M. (2007). "Effect of Aggregate Gradation on Fatigue Life of Asphalt Concrete Mixes." *Transportation Research Board*, 1630(1998), 62-68.

[57] Sousa, J. B., Tayebali, A. A., Harvey, J. T., Hendricks, P., and Monismith, C. L. (1993). "Sensitivity of SHRP-A003A Testing Equioement to Mix Design Parameters for Permanent Deformation and Fatigue." *Transportation Research Record*, 1384.

[58] Spoelstra, M. R., and monti, G. (1999). "FRP-confined concrete model." *J.Compos.Constr.*, 3, 143-150.

[59] Sulaiman, S. J., and Stock, A. F. (1995). "The use of Fracture Mechanics for the Evaluation of asphalt mixes." *The Association of Asphalt Paving Technologists*, 64, 500-533.

[60] Suo, Z., and Wong, W. G. (2009). "Analysis of fatigue crack growth behavior in asphalt concrete material in wearing course." *Construction and Building Materials*, 23(1), 462-468.

[61] Tayebali, A. A. (1994). "Fatigue Reponse of Asphalt-Aggregate Mixtures " *Report A404, SHRP Project A003A. Strategic Highway Research Program, National Research Council, Washington, D.C*.

[62] Tepfers, R. (2001). "Compatibility related problems for FRP and FRP reinforced concrete." *Int. Workshop Composites in Construction: A Reality, ASCE, Reston, VA*.

[63] Tigdemir, M., Karasahin, M., and Sen, Z. (2001). "Investigation of fatigue behaviour of asphalt concrete pavements with fuzzy-logic approach." *International Journal of Fatigue*, 24(8), 903-910.

[64] Wang, l., Frost, J. D., G.Z, V., and Harman, T. P. (2003). "Quantification of damage parameters using X ray tomography images." *Journal of mechanics of materials*, 35(8), 777-790.

[65] Wang, L., Frost, J. D., and Shashidhar, N. (2001). "Microstructure Study of Wes Track Mixes from X-ray Tomography Images." *TRR*, 1767, 85-94.

[66] Wang, L. B., Paul, H. S., Harman, T., and Anglo, J. d. (2004). "Characterization of aggregate and asphalt concrete using X ray tompgraphy." *AAPT*, 73, 467-500.

[67] Wen, H., and Bahia, H. (2009). "Characterizing fatigue of asphalt binders with viscoelastic continuum damage mechanics." *Transportation research record*, 2126, 55-62.

[68] Yang, B. (2001). "A cohesive zone model for fatigue crack growth in quasibrittle materials " *International Journal of Solids and Structures*, 38, 3927-3944.

[69] You, Z., Adhikari, S., and Kutay, M. E. (2008). "Dynamic modulus simulation of the asphalt concrete using the X-ray computed tomography images." *Materials and Structures*.

[70] Zhang, L., Sitaraman, R., Patwardhan, V., Nguyen, L., and Kelkar, N. (2003). "Solder Joint Reliability Model with Modified Darveaux's Equations for the micro SMD Wafer Level-Chip Scale Package Family." *2003 Electronic Components and Technology Conference*.